Università Politecnica delle Marche
Scuola di Dottorato di Ricerca in Scienze dell'Ingegneria
Corso di Dottorato in Ingegneria Industriale

---

# An Innovative Pressing Process by Mechanical Interference Fit for Assembly and Calibration of Fuel Injector

Ph.D. Dissertation of:

**Andrea Liuti**

Supervisor:

**Prof. Nicola Paone**

Assistant Supervisor:

**Dott. Ing. Francisco Rodriguez Verdugo**

Ph.D. Course Coordinator

**Prof. Ferruccio Mandorli**

16° Edition – New Series

# Acknowledgements

This thesis has one name on its cover, but its contents is a collective work of many people that have to be acknowledged.

I would like to express my most profound gratitude and sincere appreciation to my Ph.D. supervisor, Professor Nicola Paone, for his guidance, encouragement, and support which he has provided throughout all my Ph.D.

I am truly grateful to Ing. Carmine Ungaro, Dr-Ing Francisco Rodriguez Verdugo and, in general, to Loccioni, partner of the Ph.D project. I am particularly thankful to Carmine and Francisco for their technical supervision, suggestions and encouragement. They gave me the possibility to work in this new topic with confidence, as well as with valuable feedbacks and directions in the research. Our accomplishments in the research are the result of team working and knowledge sharing. I have learned a lot in an environment where ideas and initiative are promoted. I had the opportunity to have contacts with many person, always receiving really helpful comments. Thank you so much.

I am also sincerely grateful to Prof. Paolo Castellini, Dr-Ing Paolo Chiariotti and Dr-Ing Luigi Montalto for their advice and assistance. I am indebted for many enlightening discussions. I wish to extend my special thanks to all my colleagues in the measure group of the Department of Industrial Engineering and Mathematical Sciences (DIISM), for their help and supports.

I am very thankful to FEV Europe GmbH and, in particular, to Ing. Thomas Körfer, Dr-Ing Hermann Josef Laumen and Ing. Holger Beurer. Thanks to their hospitality I had the opportunity to spend 9 fantastic months in Germany for an excellent research experience, which significantly contributed to this thesis. I incremented my knowledge level in a new area that enriches this research of an important part.

Most importantly, I would like to express my gratitude to my girlfriend, Francesca; she has always motivated me to give all my best and use the capacities that I could not see. She encouraged me to catch all the opportunities, placing my growth at the first place.

Last but not least, I would like to thank my family for their love, sacrifice, and encouragement.

Thank you.

*Andrea*

# Abstract

The production processes of fuel injectors can be significantly improved by a more accurate positioning control in the assembly of key components by interference fit.

This thesis presents an innovative press-fitting station in the assembly line, that combines a hydraulic cylinder and a piezoelectric actuator to reach micrometric accuracy in axial positioning. The hydraulic cylinder permits a long operational range, while the piezo actuator provides dynamic action and micrometric accuracy. The experimental characterization of the prototype press is presented together with the physical phenomena influencing the overall system performance. The tests are done using cylindrical plugs and sleeves to replicate the insertion of shafts into holes. The test samples are designed and machined to obtain a predefined interference fit. The classic press-fit assembly process can barely reach micrometric accuracy because the deformation on the contact surface cannot be measured easily. The presented new press-fit station can overcome these limits thanks to the developed advanced control strategy: when the piezo actuator is driven by an amplitude modulated sinusoidal signal, final positioning of ±2 µm is reached insertion forces up to 20 kN.

The remarkable performances obtained using dedicated samples have been then tested for real components in two different use cases: dry calibration process for GDI injector and assembly of a solenoid control valve for state of the art common rail diesel injector.

The first is a cleaner process for calibration of GDI injector in the ballistic region, that uses Nitrogen instead of a liquid working fluid. With this approach a substantially lower error for the injected quantity in the low quantity region can be accomplished, together with a cheaper management of an inert gas with respect to the liquid one.

The second application case is an assembly between the pin and the armature of the solenoid control valve of a common rail diesel injector. The relative position of the armature with respect to the valve body influences the operational behaviour of the injector during the transient opening and closing phases. In order to gain a more predictable behaviour of the fuel injector, needed for upcoming legislative requirements, a high geometric accuracy is mandatory.

These studies have confirmed the possibilities of the press prototype in real application cases; thus, the press can be inserted in real industrial process, achieving the scope of the research.

# Abbreviations

| | |
|---|---|
| ECU | Engine Control Unit |
| CR | Common Rail |
| GDI | Gasoline Direct Injection |
| ICE | Internal Combustion Engine |
| $NO_x$ | Nitrogen Oxides |
| CO | Carbon Oxides |
| $CO_2$ | Carbo Dioxides |
| HC | Hydrocarbons |
| LDV | Light Duty Vehicle |
| NEDC | New European Driving Cycle |
| EUDC | Extra Urban Driving Cycle |
| CADC | Common Artemis Driving Cycle |
| WMTC | Worldwide Motorcycle Test Cycle |
| PEMS | Portable Emissions Measurement Systems |
| WLTC | Worldwide harmonized Light duty Test Cycle |
| WLTP | Worldwide harmonized Light duty Test Procedure |
| UNECE | United Nations Economic Commission for Europe |
| PMR | Power Mass Ratio |
| RDE | Real Driving Emissions |
| GHG | GreenHouse Gas |
| PM | Particulate Matter |
| DPF | Diesel Particulate Filter |
| GPF | Gasoline Particulate Filter |

# *Abbreviations*

| | |
|---|---|
| PSE | Propulsion System Efficiency |
| EGR | Exhaust Gas Recirculation |
| HCCI | Homogeneous Charge Compression Ignition |
| SCR | Selective Catalytic Reduction |
| LNT | Lean $NO_x$ Trap |
| TWC | Three-Way Catalyst |
| SF | Swirl Flaps |
| TBI | Throttle Body Injection |
| MPFI | Multi-Point Fuel Injection |
| SFI | Sequential Fuel Injection |
| SPFI | Sequential Port Fuel Injection |
| HPCR | High Pressure Common Rail |
| SQA | Small Quantity Adjustment |
| ET | Energizing Time |
| FSA | Fuel Set-point Adaptation |
| $\dot{m}_{air}$ | Mass flow of the air at the engine intake |
| $\lambda$ | Air to fuel ratio |
| $\rho$ | Density |
| FSN | Filter Smoke Number |
| $\lambda_{st}$ | Stoichiometric air to fuel ratio |
| $\mu_s$ | Static friction coefficient |
| $\mu_d$ | Dynamic friction coefficient |
| DLDV | Differential Laser Doppler Vibrometer |
| CSD | Constant Slope Driving |
| SWTI | Square Wave Train Impulse |
| AMSD | Amplitude Modulated Sinusoidal Driving |

# *Abbreviations*

| | |
|---|---|
| DOE | Design Of Experiment |
| cRIO | compact Reconfigurable Input Output |
| FPGA | Field Programmable Gate Array |
| AS | Adjustment Sleeve |
| STS | Shot To Shot |
| MAE | Mean Absolute Error |
| $\rho_{xy}$ | Pearson correlation coefficient |
| FAG | Final Air Gap |

# List of Figures

# *List of Figures*

# *List of Figures*

# List of Tables

# Contents

*Contents*

*Contents*

# 1. Introduction

## 1.1. Motivation

The goal of this thesis is to improve the quality of the fabrication processes related to the production of fuel injectors, chosen as products of interest, by mean of a more accurate positioning in the assembly of key components by interference-fit. A micrometric positioning accuracy is currently requested in order to have a more stable and repeatable behaviour of the injector, really important in low fuel delivery regions.

Most of commercial assembly systems are not able to accomplish this requirement in a robust and reliable way, leading to more emissions and the necessity to compensate for this inaccuracies with dedicated learning functions implemented in the Engine Control Unit (ECU).

The adoption of the developed process can lead to remarkable improvements in the injector's production process, fulfilling the tighter requirements needed in order to respect new emission regulations.

### 1.1.1. Interference fit assembly processes

In the automotive industry, exist many assembly processes that require a high geometric accuracy, in the micrometric range; generally, widely used open-loop controllers cannot meet these requirements. Interference fit, also named press fit or friction fit, provides a stable fastening between two parts by friction. Interference fit is generally achieved by shaping the two mating parts so that one part is slightly larger than the other. In general, such an assembly consist in the insertion of a shaft or a plug inside a hole, with interference. When two parts are pressed together, the static insertion force is generally considered as the main control parameter for the pressing process. However, only an approximate value of the insertion force can be computed beforehand because the friction coefficient is not known with appropriate accuracy and the assumed constant pressure is altered by the axial force through the Poisson effect. This difference from the ideal condition causes a non-predictable behaviour of the inserted part and an associated uncertainty of the process. To develop a new press-fitting process, it is desirably important to know, what are the main process variables to be managed and how they evolve during the production process, in order to control the quality of the products and their conformity to the functional specifications.

This work is an intermediate step towards *Industry 4.0* and, in particular, to the concept of *Zero Defect Manufacturing*, that needs an active integrated quality control. Currently, the quality controls of the final assembled products are executed at the end of the process, thus not able to change in relation of modifications of material, geometry or components due to inaccuracies of the previous production phases. With conventional approach, the quality control is only a filter and thousands of products might be produced before the detection of the fault. The solution is to measure continuously the quality of the assembly and monitor the status, adapting the fabrication process in real time.

### 1.1.2. Implications in the automotive industries

Press fit is particularly relevant in automotive industry, where many components of the fuel injection system are realized by interference fit assembly. For these components, interference fit assembly can be subject to different specifications: in some cases, the final axial position of the plug with respect to the sleeve is the main feature to keep under control, often down to micrometric accuracy. In other cases, the functional performance of the assembled component determines the compliance of the process to the specifications. In components like fuel injectors or valves, the functional performances that are need to be achieved might be related to the flow of the fluid across the component: for example, mass or volume flow rate or pressure drop are the real specifications that is aimed to achieve. Functional performances of fuel injection system parts are strictly related to engine performance, fuel consumption, combustion efficiency, pollutant emissions and engine reliability. Since pollutant emission standards are becoming tighter and tighter with view on absolute numbers but as well on durability and lifetime performance, the automotive industry is striving to increase efficiency of the production processes of key sub-systems, including fuel injection components. Therefore, the assembly tolerances both in the final positioning and in the functional performance are becoming more and more demanding.

## 1.2. Research Objectives

The aim of the present research is to improve the mechanical assembly processes for key components in fuel injection equipment with interference fits. The injectors for internal combustion engines were chosen as the products of interest, where different assembly processes are used today to produce these components, depending on the specific application.

In order to accomplish this aim, the characteristic phenomena that take place during the insertion of a shaft in a hole, with interference, will be analysed. The focal points that lead to the inaccuracies will be pointed out and the solutions to overcome these limitations will be expressed with the realization of an advanced press station prototype. The performances of the new process will be analysed in two different application cases: in one the main feature is a fundamental functional performance and more precisely the injected fuel quantity. Indeed, the proposed dry calibration process for Gasoline Direct Injection (GDI) injectors combines the press station and a shot-to-shot device, fed with nitrogen. As a second study case, the assembly of the control valve of a Common Rail (CR) Diesel injector was selected. For this application, the specifications required a high accuracy over the entire process in terms of relative position of the inserted parts.

The proof of concept in two different applications depicts the maternity of the advanced approach for implementation in series production.

# 2. State of the Art

A literature survey of prior research relevant to the current study is given in this chapter starting from the framework of emissions regulations and the current technologies employed in order to have more efficient Internal Combustion Engines (ICE). The second part describes fuel injectors in more details: functional concept, inaccuracies and the adopted strategies for the correction of these issues. The last part addresses existing press-fit processes in current production lines, the theoretical aspects and the characteristic phenomena involved.

## 2.1. Regulatory Framework Regarding Emissions

### 2.1.1. From NEDC to WLTC

For obtaining type approval of engine-powered vehicles in the European Union, light-duty vehicles have to comply with emission limits during standardized laboratory emission testing. Although Euro 1 – 5 tier emission limits have become more stringent over the past two decades, in 2008 light-duty vehicles still contributed to the overall NOx emissions of the EU for 41% [1 – 2]. This share can be substantially higher in urban areas where 16% of the population is currently exposed to $NO_2$ concentrations that exceed given air quality standards. The European legislator has responded to this situation by introducing more stringent Euro 6 emission limits that have been enforced for light-duty vehicles from September 2014 [3 – 4] onwards, consisting in a series of tightening steps.

For emission certification of light-duty vehicles (LDVs) various driving cycles and type-approval test procedures are employed around the world [5] that differ in their ability to statistically represent the real-world conditions and diversity. For example, the New European Driving Cycle (NEDC) is used for the certification of European emission standards up to EU-6.1; it is a modal driving cycle that consists of four repeated urban driving sequences (ECE-15 cycles) and one extra-urban driving portion (EUDC). The entire cycle covers a distance of 11.007 km in 1180 s at an average of 34 km/h. The NEDC (Fig. 2.1) is being used for emission type-approval from Euro 3 and later LDVs in Europe and has been criticized for not being anymore representative of the real-world vehicle operation nowadays.

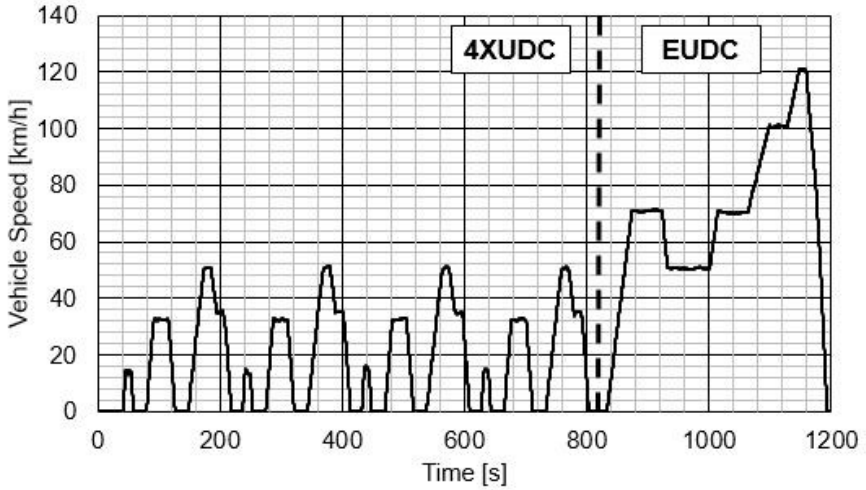


*Figure 2.1 - NEDC emission test*

Several studies [6 – 8] have shown that actual on-road emissions and fuel consumption can be substantially higher than values reported during the type approval testing on a chassis dynamometer in certified testing laboratories. The CADC (Common Artemis Driving Cycle) represents a real-world simulation driving cycle that aims to characterize average driving conditions in today's Europe [9]. Studies have shown that its higher dynamicity resulted also in higher emissions compared to the NEDC [10]. Furthermore, the emissions of passenger cars measured over the newly developed Worldwide Motorcycle Test Cycle (WMTC) are assumed to be closer to real world driving emissions. By recently developed Portable Emissions Measurement Systems (PEMS) has been also possible to realize on-road emission tests, that have shown how the current laboratory emission test fails to reliably capture on-road emissions, especially in the case of NOx for Diesel cars and particulates of gasoline powered vehicles [11 – 12].

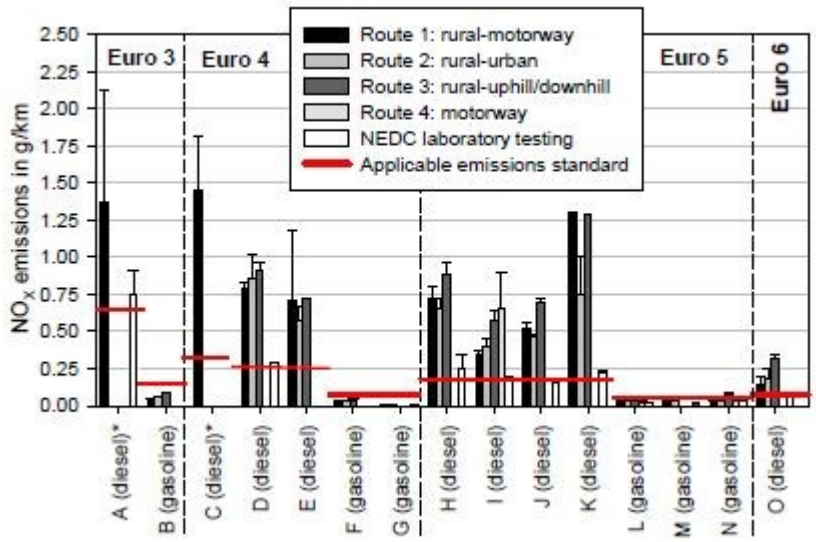


*Figure 2.2 - Gap between on-road vs. laboratory testing (Source: M. Weiss, P. Bonnel, R. Hummer, N. Steinenger, "A complementary emissions test for light duty vehicles: assessing the feasibility of candidate procedures")*

Therefore, despite many objective benefits, the NEDC is increasingly attracting criticism, some of it justified, that it is no longer representative for the average driving style of a vehicle or driver. The member states which signed the 1998 treaty of the United Nations Economic Commission for Europe (UNECE), including all the European countries as well as Japan, USA, China, Russia and India, therefore decided to develop a new test procedure, the WLTP, under the auspices of the UNECE. This should be properly representative of the driving style of a vehicle anywhere in the world. The automotive industry played a major role in supporting and advancing this initiative.

The development of the WLTC was carried out under a program launched by the World Forum for the Harmonization of Vehicle Regulations (WP.29) of the UNECE through the working party on pollution and energy transport program (GRPE). The aim of this project was to develop a World-wide harmonized Light duty driving Test Cycle (WLTC), to represent typical driving characteristics around the world, to have the basis of a legislative worldwide harmonized type certification test from 2014 onwards. Driving cycles are produced by different countries and organizations and used to assess the performance of vehicles, such as pollutant emissions, fuel consumption and traffic impact. There are two main categories of test cycles: legislative cycles employed in type-approval tests for vehicles emissions certification and non-legislative cycles mainly used in research. Several

international harmonized engine dynamometer cycles have been developed for engine emission certification of heavy-duty and non-road engines (WHSC, WHTC, NRTC). A worldwide harmonized test cycle has been developed also for motorcycles emissions (WMTC).

For Light-Duty (LD) vehicles, various vehicle dynamometer test cycles are employed in type-approval tests for emission certification. Such test cycles are: the NEDC used in Europe, JC082 applied in Japan, the UDDS (FTP-75) used in the United States. Each of these driving cycles has advantages and drawbacks, as the ones highlighted for the NEDC in the previous paragraphs.

Therefore, when the WLTC project started, it has been agreed to design a new legislative driving cycle to predict more accurately the exhaust emissions and fuel consumption under real-world driving conditions. WLTC (Fig. 2.3) was derived from "real world" driving data from five different regions: EU + Switzerland, USA, India, Korea and Japan covering a wide range of vehicle categories (M1, N1 and M2 vehicles, various engine capacities, power-to-mass ratios, manufacturers etc), over different road types (urban, rural, motorway) and driving conditions (peak, off-peak, weekend).

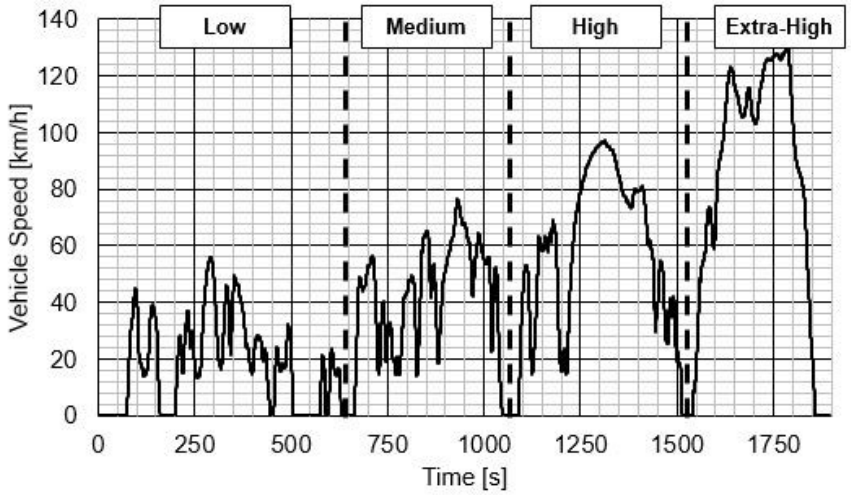


*Figure 2.3 - WLTC emission test*

The WLTC assigned to the highest power mass ratio (PMR) vehicle category (class 3), which represents the vast majority of European vehicles, is composed by four speed phases (low, medium, high and extra-high). The WLTC lasts 1800 s, features a more dynamic speed profile as well as a higher mileage than NEDC. However, the WLTC has the vehicle

accelerating or decelerating 84% of the time over the whole cycle, with only 13% at idle and 4% at constant cruise driving, while 40% of the NEDC is at a steady state cruise condition, 24% at idle and the remaining 36% is spent accelerating or decelerating.

On the other hand, following concerns over the "real-world" performance of vehicles approved using the chassis dynamometer test, the European Commission announced in its CAR 2020 Action Plan that it intends to include an additional test for "Real Driving Emissions of LDV (RDE-LDV) from the start of the Euro 6 stage, an on-road measurement using PEMS for gaseous regulated emissions. During a first transitional period, the test procedures should only be applied for monitoring purposes, while afterwards they should be applied together with binding quantitative RDE requirements to all new type-approvals/new vehicles [13].

The concept idea is that throughout its normal life, the emissions of a vehicle type-approved according to Regulation (EC) No 715/2007 emitted at a RDE test performed, shall not be higher than the following not-to- exceed (NTE) values:

(1) $$NTE_{pollutant} = CF_{pollutant} \times EURO - 6$$

where *EURO - 6* is the applicable Euro 6 emission limit in Table 2 of Annex I in Regulation (EC) No 715/2007 and $CF_{pollutant}$ the conformity factor for the respective pollutant. The trip sequence shall consist of urban driving followed by rural and motorway driving that has to be run continuously.

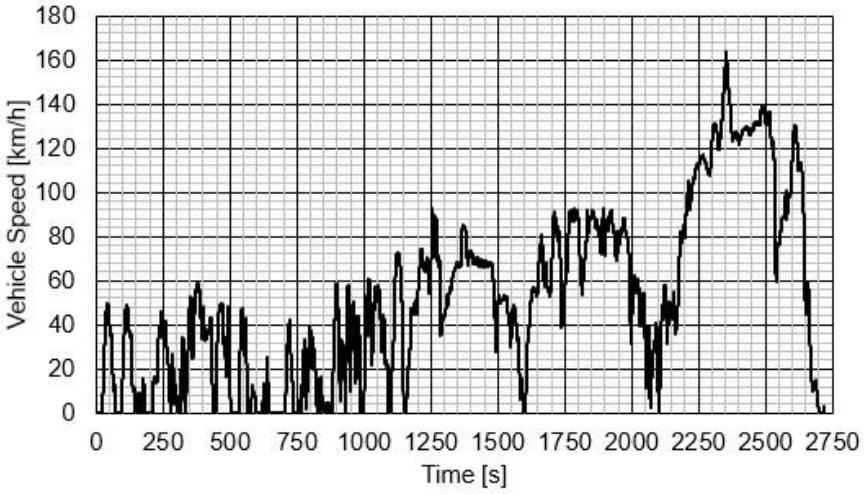


*Figure 2.4 - RDE emission test*

WLTP test procedure should provide in a method to determine the levels of gaseous and particulate emissions, $CO_2$ emissions, fuel consumption, electric energy consumption and electric range from light-duty vehicles in a repeatable and reproducible manner, designed to be representative of real-world vehicle operation. These measurement results shall form the basis for the regulation of these vehicles within regional type approval and certification procedures, as well as an objective and comparable source of information to consumers on the expected fuel/energy consumption.

This theme is particularly important nowadays, since from the end of 2017 the NEDC is going to be phased-out while WLTC and RDE phased-in, as shown in Fig. 2.5. This is driving the technological research on ICE more efficient, less pollutant and on emissions reduction mechanisms, in order to adopt the most effective solutions able to overcome these new limitations.

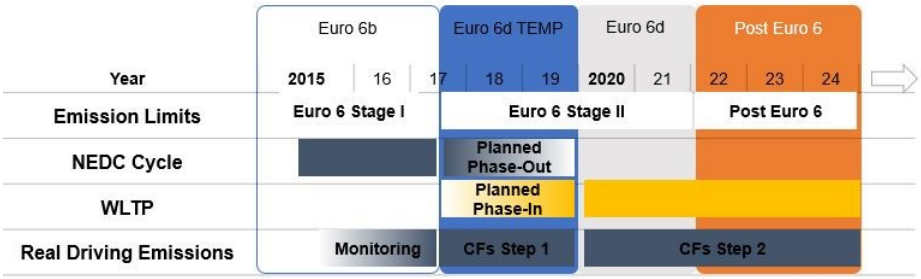


*Figure 2.5 - Time frames of the type approval test cycles*

### 2.1.2. Emissions and fuel efficiency of ICE for mobility

As reported by Johnson [14 – 16] engine technology is evolving very rapidly, primarily to meet the tighter emissions regulations in all the major markets. In light-duty applications, the future choices to meeting market demands and GHG regulations will continue to drive the most economical choices, which so far, are engine-based approaches rather than battery-electric or fuel cell vehicles.

The most important areas of improvement, all under cost constraints, regard:

- Engine technologies for $CO_2$ reduction
- $NO_x$ control
- Particulate control
- Gaseous pollutant control
- Reliability
- Performance

Generally, the technologies used to fulfil these improvements can be divided in three main categories, usually used at the same time in an ICE:

- Downstream of the cylinder
- Inside the cylinder
- Upstream of the cylinder

Downstream interventions do not involve directly the combustion process, but target the exhaust gases by treating them, in order to reduce the pollutant concentration. Upstream interventions are directly related at the combustion process, in order to prevent the formation of pollutants acting principally on the air path and on the injection.

Increasing engine efficiency, hence reducing the fuel consumption in addition to reducing the driving resistance, is the only way to reduce the $CO_2$ emissions of cars and other transportation vehicles driven by internal combustion engines. For this reason, another area of intervention is friction reduction. Although the useful work loss due to engine friction is relatively small for modern engines [17], the reduction of all parasitic energy losses, including friction, remains as a valuable contribution to overall efficiency improvement. Lubrication and friction play essential roles in energy conservation. There are many moving parts in an engine. Proper lubrication keeps them in good working order, extends component longevity, and minimizes energy losses due to friction.

Further solutions for $CO_2$ reduction are the concepts of down-sizing and down-speeding. Downsizing refers to the practice of automotive engineers to reduce the displacement and/or number of cylinders in an engine. Down-speeding is matching the gearing of the transmission and differential to the engine, so the engine turns at lower RPM for a given highway speed. Both these techniques are currently widely used in light-duty gasoline engines to improve fuel efficiency and reduce both regulated and green-house gas emissions with great success.

Downsizing can increase fuel efficiency by 20 to 30% and down-speeding can add an additional 3 to 7%.

#### 2.1.2.1. Downstream intervention

Several devices are installed in the exhaust system, usually mixed for the maximization of the pollutant reduction. The first one is the catalytic converter, an exhaust emission control device that converts toxic gases by catalysing a redox reaction (an oxidation and a reduction reaction). Catalytic converters are used with ICE fuelled by either gasoline or diesel. The "two-way" converters combine oxygen with CO and unburned HC to produce $CO_2$ and $H_2O$. The two-way catalytic converters were rendered obsolete by "three-way" converters that also reduce NOx. However, two-way converters are still used for lean-burn engines. This is because three-way-converters require either rich or stoichiometric combustion to successfully reduce NOx.

The catalytic converter's construction is as follows:

1. The catalyst support or substrate, usually a ceramic monolith with a honeycomb structure. Metallic foil monoliths made of Kanthal (FeCrAl) [18] are used in applications where particularly high heat resistance is required. Either material is designed to provide a large surface area.
2. The washcoat, a carrier for the catalytic materials used to disperse the materials over a large surface area. Aluminum oxide, titanium dioxide, silicon dioxide, or a mixture of silica and alumina can be used. The catalytic materials are suspended in the washcoat prior to applying to the core. Washcoat materials are selected to form a rough, irregular surface, which greatly increases the surface area compared to the smooth surface of the bare substrate. This in turn maximizes the catalytically active surface available to react with the engine exhaust.
3. Ceria or ceria-zirconia. These oxides are mainly added as oxygen storage promoters. [19]
4. The catalyst itself is most often a mix of precious metal. Platinum is the most active catalyst and is widely used, but is not suitable for all applications because of unwanted additional reactions and high cost. Palladium and rhodium are two other precious metals used. Rhodium is used as a reduction catalyst, palladium is used as an oxidation catalyst, and platinum is used both for reduction and oxidation. Cerium, iron, manganese and nickel are also used, although each has limitations.

In order to reduce the particulate matter, a filter is installed in both diesel and gasoline engines, accordingly named Diesel Particulate Filter (DPF) and Gasoline Particulate Filter (GPF), respectively. GPF are mainly developed to control particulate emissions from GDI engines that have been increasing in terms of population, driven by $CO_2$ and fuel economy requirements. The emission regulations have set PN (as well as PM) limits for GDI vehicles that are equivalent to those for diesels; thus, an effective particulate filter is needed. Current filters are designed to burn off the accumulated particulate either passively through the use of a catalyst or by active means such as in-cylinder port injection or a fuel burner which heats the filter to soot combustion temperatures. This is accomplished by engine programming to run (when the filter is full) in a manner that elevates exhaust temperature, in conjunction with late post injection, enriching the fuel that reacts with a catalyst element to burn off accumulated soot in the filter [20] or through other methods. This is known as "filter regeneration".

$NO_x$ control is currently focused on active Selective Catalytic Reduction (SCR), a means of converting NOx with the aid of a dedicated catalyst into $N_2$, and $H_2O$. A gaseous reductant, typically anhydrous ammonia, aqueous ammonia or urea, is added to the stream of exhaust gas and is adsorbed onto a catalyst. $CO_2$ is a reaction product when urea is used as the reductant. Pure anhydrous ammonia is extremely toxic and difficult to store safely, but needs no further conversion to operate within an SCR. Aqueous ammonia must be vaporized, in order to be used, but it is substantially safer to store and transport than anhydrous ammonia. Urea is the safest to store, but requires conversion to ammonia through thermal decomposition, in order to be used as an effective reductant [21]. Using urea as reductant, the reaction is the following:

$$4NO + 2(NH_2)_2CO + O_2 \rightarrow 4N_2 + 4H_2O + 2CO_2$$

The ideal reaction has an optimal temperature range between 630 and 720 K, but can operate from 500 to 720 K with longer residence times. The minimum effective temperature depends on the various fuels, gas constituents, and catalyst geometry. SCR catalysts are made from various ceramic materials used as a carrier, such as titanium oxide, and active catalytic components are usually either oxides of base metals (such as vanadium, molybdenum and tungsten), zeolites, or various precious metals. The two most common designs of SCR catalyst geometry used today are honeycomb and plate. The honeycomb form usually is an extruded ceramic applied homogeneously throughout the ceramic carrier or coated on the substrate. Like the various types of catalysts, their configuration features typically advantages and disadvantages. Plate-type catalysts have lower pressure drops and are less susceptible to

plugging and fouling than the honeycomb types, but plate configurations are much larger and more expensive. Honeycomb configurations are smaller than plate types, but have higher pressure drops and plug much more easily. Catalysts are being characterized further for sulfur degradation and tolerance. Low temperature performance is enhanced with high catalyst loadings, enabled by high-porosity substrates. High temperature performance is improved using higher cell density catalysts.

Lean $NO_x$ Traps (LNT) method uses a catalyst [22] which consists of a storage component and a precious metal supported on Alumina. The reaction takes place in 2 cycles (i.e.) lean and rich cycle. In the lean cycle, NO is adsorbed onto the storage component and oxidized to NO2 over the catalyst and stored in the form of nitrate at the surface. In the rich cycle, this stored NOx is released from the surface and reduced to N2 by HC, CO and H2 generated from incomplete combustion of fuels over the noble metal catalyst. Though the reactions are completed in 2 separate cycles, the overall reaction shows similarity with SCR reactions. Sulfur poisoning remains an issue which leads to deactivation of the catalyst [23]. Ammonia forming capability varies for different SCR catalysts. Pt/Al2O3 shows higher amounts of NH3 at high temperature, whereas Pd/Al2O3 is less affected by temperature variations [24]. LNT are also improving regarding sulfur tolerance and passive release of the $NO_x$ using only temperature increases. LNTs are being combined with SCR in the light duty sector to reduce urea consumption and improve system low-temperature performance.

#### 2.1.2.2. In-cylinder measures

Different strategies can be adopted, in order to change the combustion process to reduce the formation of emissions [25]. However, changes which decrease NOx often increase the engine-out emissions of PM, and vice versa. For example, lowering the maximum temperature reached during combustion reduces NOx emissions, but inhibits the complete oxidation of soot, thereby increasing particulate emissions. This is known as the NOx-PM trade-off and presents a critical challenge to emission reduction strategies. Changing the engine parameters may also affect fuel economy, requiring the optimization of NOx, PM, and fuel economy for the specific application. Hereafter, a list of interventions will be discussed.

Achieving good mixing of the air and fuel injected into the combustion cylinder reduces both NOx and PM emissions yet is difficult in the small, high-speed engines used in cars and light trucks. In-cylinder alterations seek to improve this process by optimizing parameters of the piston bowl - the small area of the piston where fuel is injected. Moving from 2-valves to 4-

valves per cylinder, altering the bowl geometry, and optimizing air motion (swirl) and fuel spray at different engine operating conditions will allow for reductions in NOx and PM.

Delaying the start of fuel injection is known as injection timing retard. This can significantly cut NOx emissions by reducing the peak gas temperature, and is currently used as a method for reducing NOx emissions. However, injection timing retard has a negative impact on particulate emissions and fuel economy.

Homogeneous charge compression ignition (HCCI) is a form of internal combustion in which well-mixed fuel and oxidizer (typically air) are compressed to the point of auto-ignition. HCCI combines characteristics of conventional gasoline engine and diesel engines. Gasoline engines combine homogeneous charge (HC) with spark ignition (SI), abbreviated as HCSI. Diesel engines combine stratified charge (SC) with compression ignition (CI), abbreviated as SCCI. As in HCSI, HCCI injects fuel during the intake stroke. However, rather than using an electric discharge (spark) to ignite a portion of the mixture, HCCI raises density and temperature by compression until the entire mixture reacts spontaneously. Stratified charge compression ignition also relies on temperature and density increase resulting from compression. However, it injects fuel later, during the compression stroke. Combustion occurs at the boundary of the fuel and air allowing a leaner and higher compression burn. HCCI engines achieve extremely low levels of oxides of $NO_x$ without a catalytic converter.

Another promising method to reduce emissions of nitrogen oxides and particulates in direct injection diesel engines is water introduction into the combustion chamber. Various introduction strategies with their particular advantages and disadvantages with respect to emissions and applicability in different engine applications are possible. For obtaining maximum improvements, water has to be added at the right spot at the right time [26]. In conventional combustion processes of both Diesel and GDI powered engines, nitrogen oxides are mainly formed by the highly temperature-dependent Zeldovich mechanism. All water introduction strategies aim at reducing the temperatures in the combustion chamber. The effect of water introduction is two-fold: water reduces the temperature by its large enthalpy of vaporization and the larger heat capacity compared to dry air. Injection of emulsions places the water at the right spot in the spray region. As a result, NOx emissions can be reduced significantly, also offering the potential to reduce particulate emissions [27 – 28].

#### 2.1.2.3. Upstream intervention

Differently from the solutions already descripted, upstream interventions aim to prevent the generation of polluting substances, improving combustion process, mostly due to

shortcomings of mixture formation between air and fuel inside different operational conditions.

One important solution that are being adopted is the introduction of a fraction exhaust gas mass in the combustion chamber. The Exhaust Gas Recirculation (EGR) system works by recirculating a portion of an engine's exhaust gas back to the engine cylinders. This dilutes and replaces the O2 in the incoming air stream and provides inert gases to combustion to act as absorbents of combustion heat to reduce peak in-cylinder temperatures [29]. Because NOx is primarily formed when a mixture of nitrogen and oxygen is subjected to high temperature, the lower combustion chamber temperatures caused by EGR reduces the amount of NOx during combustion. Therefore, the exhaust gas, added to the fuel, oxygen, and combustion products, increases the specific heat capacity of the cylinder contents, which lowers the adiabatic flame temperature. The maximum quantity of mass introduced is limited by the need of the mixture to sustain a continuous flame front during the combustion event; excessive EGR in poorly set up applications can cause misfires and partial burns. The impact of EGR on engine efficiency largely depends on the specific engine design, and, in Diesel engines, leads to a compromise between efficiency and NOx emissions.

A properly operating EGR can theoretically increase the efficiency of gasoline engines via several mechanisms:

- Reduced throttling losses. The addition of inert exhaust gas into the intake system means that for a given power output, the throttle plate must be opened further, resulting in increased inlet manifold pressure and reduced throttling losses
- Reduced heat rejection. Lowered peak combustion temperatures not only reduces NOx formation, it also reduces the loss of thermal energy to combustion chamber surfaces, leaving more available for conversion to mechanical work during the expansion stroke.

EGR is after not employed at high loads as it would reduce peak power output. This is because it reduces the intake charge density. EGR is also typically limited at idle because it would cause unstable combustion, resulting in rough idle.

Another adopted solution is the turbocharging of the engine that coupled with downsizing might increase efficiency, first of all by reducing relative impact of heat and friction losses – increasing the specific power of smaller engine. Further downsizing and increased power densities are key concept for achieving higher break thermal efficiencies and future emission legislations for internal combustion engines. These necessitate advanced turbocharger

technologies such as e-boosting systems in combination with fully variable valve trains and high compression ratios for optimized fuel consumption in part load operation.

In the intake system can also be installed a Swirl Flaps (SF), [30] small butterfly valves fitted just before the cylinder head intake ports. SF position is adjusted by an electrical or vacuum-actuated servo mechanism which is under the control of the ECU. In a typical implementation (4-cylinder engine, 1 port per cylinder) the flaps will be closed at idle speed, creating additional turbulence in the intake. As engine speed increases, the flaps are gradually opened until they are parallel to the airflow and present virtually no resistance. Their purpose is to ensure that the air entering the cylinder is sufficiently turbulent for good fuel-air mixing even at low engine speeds. This aids in providing more mixture formation energy, especially in load areas, where fuel injection pressure is limited.

One of the most effective solutions to improve the combustion process is the development of the fuel injection systems optimized for new fuel injection strategies. Choosing between various injection strategies are highly effective techniques to reduce emission from engines as injection characteristics have great influences on the process of combustion [31].

For example, for common rail diesel engines, the adopted strategy is characterized by several injections [32 – 34]:

- Pilot → this injection occurs in advance respect to the main injection. The purpose is to reduce combustion noise and realize a pre-reaction of the pilot quantity which reduces the combustion delay of the main injection. Splitting the pilot in two injection events, the second is also used for shaping the heat released rate curve, thus the pression inside the chamber.
- Main → this is the so called “torque-forming” injection where the power of propulsion the vehicle is generated and peak of the chamber pressure is reached.
- After Injection → the purpose is the same of a second pilot in terms of shaping the heat release rate and/or introduce additional mixture energy into the combustion chamber at late phase.
- Post Injection → this injection is done to have an enrichment of the exhaust that ensures thermal management, e.g. the regeneration of the particulate filter.

Experiments [35] have shown that with high pressure multiple injections (two or more injection pulses per power cycle), the soot-NOx trade-off curves of a diesel engine can be shifted closer to the origin than those with the conventional single-pulse injections, reducing both soot and NOx emissions significantly.

## 2.2. Fuel Injectors

As mentioned, fuel injectors play a key role for ICE's in reducing emissions to meet future emission standards, as well as achieving other performance parameters like power/torque fuel economy and combustion noise.

The most important innovation of the injection systems has been the introduction (from the 1980s onward) of the electronic control of the injector's opening and closing; using a solenoid or a piezoelectric element the injection event is driven by means of either an electric signal without a mechanical/hydraulic connection to the engine. The injectors need to fulfil the following targets:

- Precise dosing → injection of the correct quantity of fuel
- Accurate phasing → no delay respect to the selected injection window
- Consistent uniformity → uniform distribution of the fuel delivery every cycle and for every cylinder
- Optimal mixing → correct mixture between fuel and air in order to foster the combustion process with the other key parameters like chamber geometry and charge motion

In the next section the state of the art of fuel injection system is discussed and the most important inaccuracies highlighted. Finally, the compensation needed, in order to correct these limits, will be pointed out.

### 2.2.1. State of the art of injectors

The engine combustion process is mainly determined by in-cylinder conditions and fuel injection strategies. Fuel injection is the introduction of fuel in an internal combustion engine by means of an injector. All diesel engines use direct fuel injection by design. Petrol engines can use gasoline direct injection, where the fuel is directly delivered into the combustion chamber, or indirect injection where the fuel is mixed with air before in the intake manifold.

Depending on the design and the layout, it is possible to define different injection system schemes:

- Single point or Throttle Body Injection (TBI) → it is composed of one or two fuel injector nozzles in the throttle body, which for spark-ignited engines is the throat of the engine's air intake manifold.
- Port or Multi-Point Fuel Injection (MPFI) → Multi-point fuel injection devotes a separate injector nozzle to each cylinder, right outside its intake port, which is why the system is sometimes called port injection. Shooting the fuel droplets this close to the intake port almost ensures that it will be drawn completely into the cylinder. The main advantage is that MPFI meters fuel more precisely than do TBI designs, better achieving the desired air/fuel ratio and improving all related aspects. Also, it virtually eliminates better the possibility that fuel will condense or collect in the intake manifold.
- Sequential Fuel Injection (SFI) → Sequential fuel injection, also called sequential port fuel injection (SPFI) or timed injection, is a type of multi-port injection. Though basic MPFI employs multiple injectors, they all spray their fuel at the same time or in groups.
- Direct Injection → More common in diesel engines, direct injection is starting to grow in gasoline engine designs in terms of vehicles number nowadays and are common these days. Again, fuel supply is at higher pressure levels and metering is even more precise than in the other injection schemes, and the direct injection gives engineers yet another variable to influence precisely how combustion occurs in the cylinders.

In MPFI and GDI systems the injectors are supplied with fuel from a common rail and the injector pulse width depends on the input signals seen by the ECU.

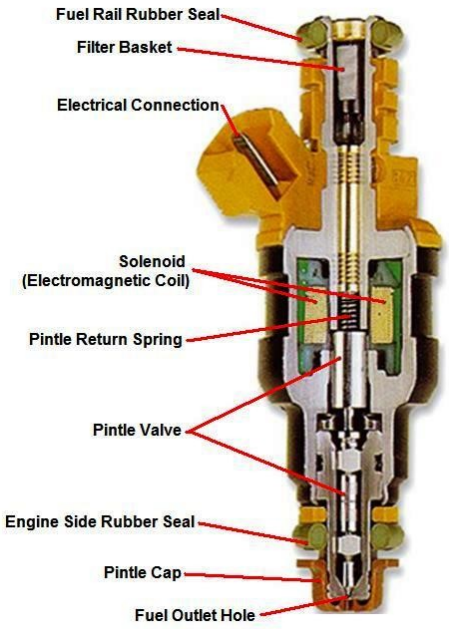


*Figure 2.6 - Schematic of a gasoline port fuel injector*

The shown port fuel injector in Fig. 2.6 is composed of two different main sectors, divided by a valve (pintle valve). In the upper one the fuel is maintained in pressure using a pump that pressurizes the rail up to 5 bars, feeding each injector. In order to avoid contaminations of the fuel, a filter is installed in the upper feeding channel. The valve is connected with the needle and it is kept in position by mean of a spring that acts between the pintle valve and the fuel filter. Electrifying the solenoid, a magnetic field is generated; the pintle valve is lifted and the fuel is free to flow. Thus, the needle opens the holes of the tip and the fuel flow into the intake manifold of port is engaged.

In diesel engines, nowadays common rail injection systems (Fig. 2.7) have affirmed their predominance in the market in the last ten years. High Pressure Common Rail (HPCR) fuel injection systems, typically employed in light and medium-duty Diesel engines, provide an effective way in fuel injection quantity and injection timing control primarily due to their high rail pressure [36 – 37]. Common rail fuel systems are equipped with a closed-loop high pressure control-system that stabilizes the rail pressure within a relatively small margin to the nominal value specified by the ECU for a given engine operating condition. The pump maintains the rail pressure by continuously delivering fuel to the common rail. This pressure is monitored by a pressure sensor and the difference between the nominal rail pressure value and the measured one is the input signal for the controller. There are several different

approaches to control the pressure in the common rail. One typical way is to supply more fuel than is needed to the common rail and use a high pressure regulator in the high-pressure circuit to spill the excess fuel back to the fuel tank.

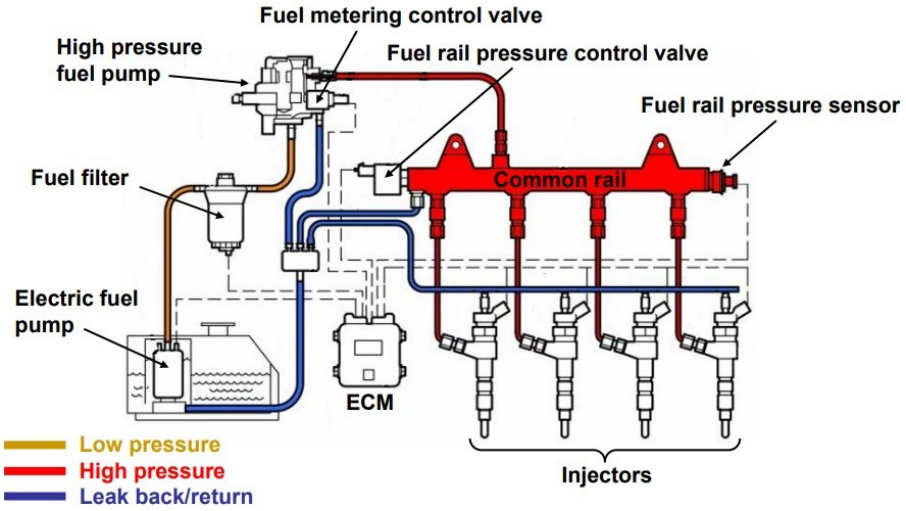


*Figure 2.7 - Example of a Diesel common rail injection system (Source: Technical overview of common rail fuel systems - AK Training)*

The design of a common rail diesel injector is different from a gasoline injector, mostly due to the higher pressure that feed the injector (up to 3000 bar in the last generation of common rail engines). As shown in Fig. 2.8, the fuel pressure is supplied to the injector needle seat area and also to a small chamber above the injector needle, also called control volume, via a calibrated inlet port [38]. Three different forces act on the injector needle:

- Elastic force ($F_e$), in the closing direction, due to the spring installed on the needle. The spring is installed, in order to close the injector when the feeding pressure is zero.
- Force ($F_c$) in the closing position due to the pressurization of the control volume
- Force ($F_o$) in the opening direction due to the pressurization of the injector needle seat

When the solenoid is energized, the valve discharges the pressure in the control volume and the fuel returns to the fuel tank via the injector leak back ports. This creates a forces disequilibrium at the needle:

(2) $$F_c = 0 \Rightarrow F_o > F_e$$

Thus, the needle is lifted and the fuel is delivered through the nozzle, injecting the requested quantity.

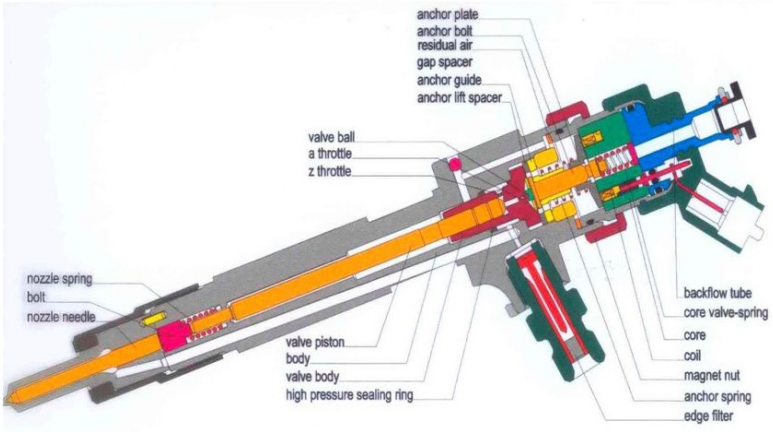


*Figure 2.8 - Schematic of a diesel common rail injector (source: Bosch)*

Piezoelectric common rail injectors are also used instead of solenoid ones. The operation of piezoelectric injectors is quite similar to that of solenoid injectors, with the difference that they have a ceramic core. However, although for this type of actuation is feasible, manufacturers had to circumvent a certain number of problems. In the first place, the dilation of a piezoelectric element is extremely low. To obtain a useable degree of displacement, it requires a stack ceramic disks to form the active element of the injector. To actuate them, an impulse of a hundred volts is applied to them and a tiny lever arm amplifies their movement. Moreover, as with electromechanical injectors, the piezoelectric disks do not directly command the needle movements, but they activate a small valve. The major advantage of piezoelectric injectors is their speed of operation and the repeatability of the movement of the valve. The dilation and retraction movements of the piezoelectric elements are almost instantaneous.

Most injectors have a specific code that must be programmed in the engine controller. The code is related to the nominal flow rate of the injector and it allows the ECU to correct the injection quantity to compensate for manufacturing tolerances. This is the first symptom of inaccuracies during the production process of the fuel injectors that lead to an unexpected non-optimal behaviour of the injector during operation. In the next section, the main inaccuracies will be explored and analysed, in order to detect the weak points of these components.

### 2.2.2. Inaccuracies of the injectors

Accurate fuel injection quantity control [39] is of importance in improving engine attributes like power output, combustion efficiency and reducing engine-out emissions. Conventional internal combustion engines are equipped with fuel injectors, under control of an ECU. The operation of an injector is controlled by means of a nominal characteristic curve correlating Energizing Time (ET) values with corresponding injected fuel quantity values. Thus, engines fuel injection quantity control algorithms are mostly based on pre-calibrated tables, which may not adequately handle the effects of disturbances, either coming from production or from aging effects during operation. Particularly, there are several factors that can lead to fuel injection quantity error; the most important are three:

1. Fuel pressure oscillation/Rail pressure waves

Using multiple events injection with a comparably short interval between injection pulses, the effect of pressure wave in fuel pipe on the subsequent fuel injections must be paid attention [40]. Due to the fast opening and closing of injector needle, the injection pressure waves are generated in the duct of CR injectors, and connecting high-pressure pipe and the injection pressure will no longer remain as constant as optimally required during the whole injection event [41 – 43], to ensure appropriate fuel metering. These pressure waves then push up or down the subsequent injection amount significantly and this makes the calibration of the subsequent injection fuel amount very difficult. Under different operating conditions, these influences become extremely serious [44].

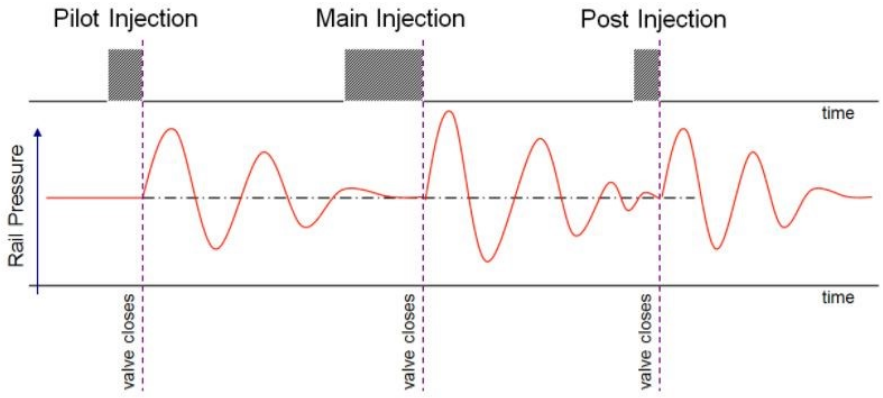


*Figure 2.9 - Rail pressure during different injections (Technology focus - Diesel Common Rail - Pressure Wave compensation, Autoelex)*

Due to the high number of influencing parameters it is an unsolved problem to analytically compute the time response of the pressure at the injector with sufficient accuracy. But as the

exact pressure progression at the injector is of importance for the accuracy of the injected fuel mass and therefore for the combustion process, its knowledge could significantly improve the efficiency and reduce the emissions of the engine. To solve this problem, a sensor based on the magneto-elastic effect was developed [45]. Conventional pressure sensors that work in a high dynamic range are often based on the piezo-resistive effect and are unaffordable for mass use in automobiles. The advantage of the ME-sensor over these conventional sensors is its low cost design and that it is working noninvasively. The disadvantage is a lower signal to noise ratio and its sensitivity to disturbances. The continuous monitoring of the pressure at the injector inlet permits to deliver information to the ECU and thus adjust the injection parameters, for a better control the injected fuel quantity.

2. Non-linearities in low quantity region

The second main factor of larger inaccuracy is the non-linear region in small fuel quantity area; this region is called “ballistic region” bacause the injector needle is in a ballistic flight condition and it is characterized by a partial stroke of the needle. This means that the ET is not long enough to lift completely the needle, operating in highly transient conditions. Therefore, it is not possible to calculate the correct ET for small quantity pulses because each injector behaves differently, depending on the reaction of this transient phenomena (Fig. 2.10).

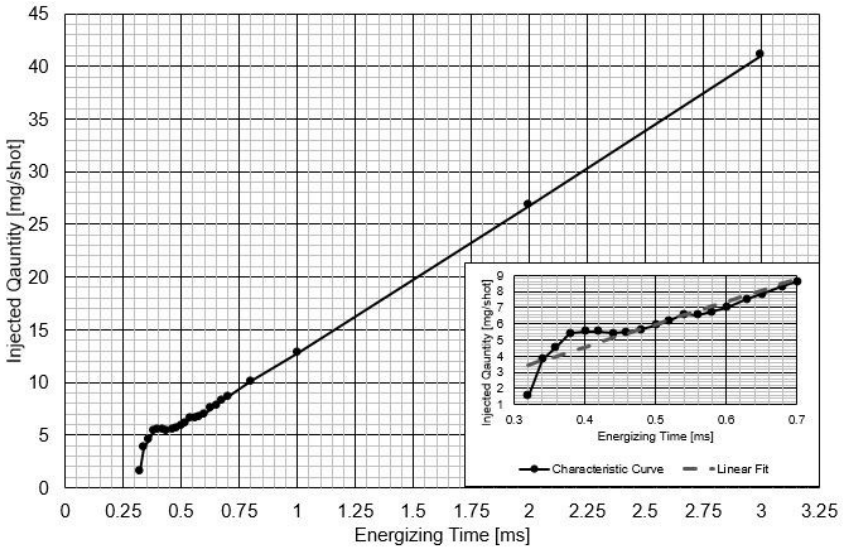


*Figure 2.10 - Characteristic curve of a GDI injector*

This problem can affect both gasoline and diesel injectors, characterized by a solenoid to command the injector.

In gasoline fuel injectors, the calibration point is chosen from the linear region and the delivered quantity measured at the end of process, in order to couple injectors with a similar behaviour in a batch, mounted in each engine. The process error is quite low and nominal characteristic curve can upload in the ECU, cutting the low delivered fuel region during engine operation. Nowadays, the restriction in terms of fuel consumption and CO2 emission require a reduction of the injected quantity and the use of the low quantity region cannot be avoided anymore. Thus, the operational range of the injector has been extended even to the ballistic region and the calibration process has to be modified in order to assure small error even in this portion of curve.

Different solutions are being adopted depending on the manufacturer and on the product. In some cases, the energizing time has been correlated with a so called "hydraulic" time that take into account the hydraulic opening and closing delays of the injector. The relation between injected quantity and hydraulic time is nearly linear, permitting a definition of a gain/offset, valid along the entire operational range.

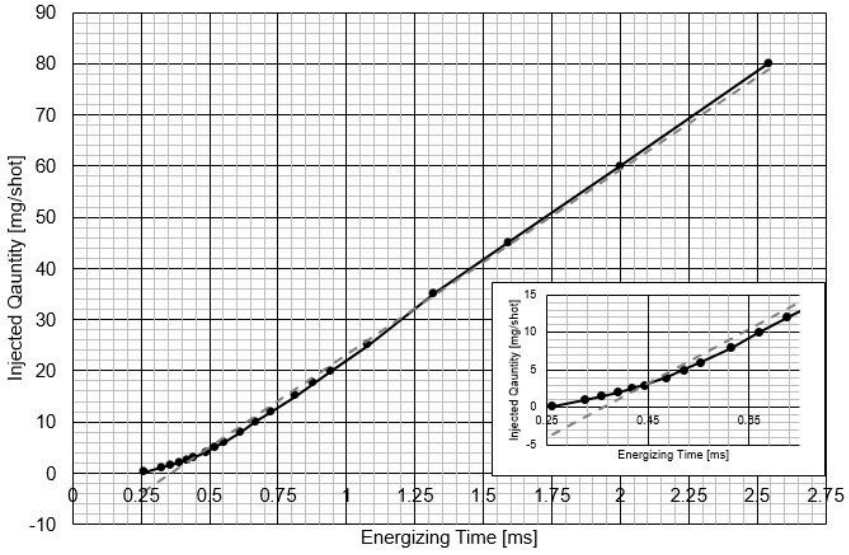


*Figure 2.11 - Characteristic curve of a CR injector without upper needle stop*

In diesel application, at the end of line of the fuel injector production process, each supplier measures the injectors specifically and release an appropriate code for each injector to document the difference to the nominal specification; this code covers the deviation of the

injector characteristic in order to reach the injected quantity target. The correction, that comes from the injector code, is in many cases based on the assumption of a linear behaviour of the injector. The use of the pre-calibrated tables and the correction from the injector code to convert the requested quantity in ET could lead to errors in the real injected quantity in the low quantity region. For instance, an incorrect pilot injected quantity can influence the following aspects:

- Pilot Injection too small → noise increment
- Pilot Injection too big → PM increment
- Misfire → noise and emissions increment, high fuel consumption

3. Injector aging/Nozzle holes coking/Deposit formation

Another term of inaccuracy is the changing of the behaviour of the injector during the lifetime. During vehicle lifetime, a drift in the actual injected fuel quantity compared with the estimation from the ECU can occur. The root causes of the deviation can be related to:

- Injector drift by wear or deposit
- Rail pressure sensor drift
- Oxygen sensor drift
- Fault on the injection system

The last three terms have an indirect impact on the injection quantity, due to a wrong input that causes an incorrect command pulse sent to the inector.

Focusing on the injectors, a modification in the characteristic curve of the injector has been observed. As explained before, the ECU determines the fuel quantity to be injected from the injector nominal characteristic curve. This nominal curve is referred to a sample injector, operating in nominal conditions and generally such curve is supplied by the injector's manufacturer. The quantity of fuel actually injected by a fuel injector may deviate from a target or nominal quantity, due to production tolerances or to ageing drift of the injector.

For all of these aspects, different strategies for control and correction have been developed, depending mostly on the requested quantity; in pilot and post-combustion injection, the main problem is the non-linear region while in the main injection, where the torque forming takes place, the drift of the injector during the lifetime has a big role.

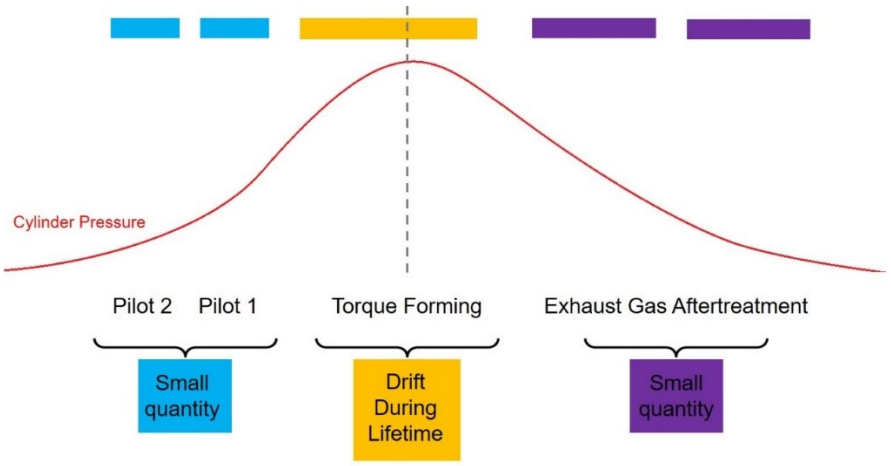


*Figure 2.12 - Different inaccuracies that have an influence in each injection*

In the next section, some fuel delivery compensation strategies will be discussed, in order to highlight the efforts necessary to overcome current limits of injectors.

### 2.2.3. Fuel delivery compensation strategies for ICE vehicle

The aim of these learning functions is to improve accuracy and reliability of the fuel delivery from the injectors and the oxygen estimation on the exhaust, both using the crankshaft sensor, precalibrated models and compensating the oxygen signal from the lambda sensor.

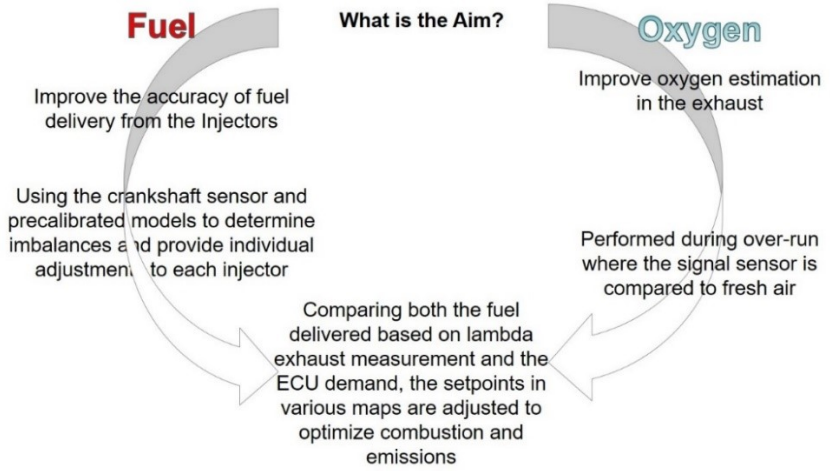


*Figure 2.13 - Schematic overview of the fuel delivery compensation strategies*

In order to improve the operational accuracy in the ballistic region, if the injector has not been tested by the manufacturer at the end of the production line, a supplementary learning phase is needed to adapt the ET, taking into account the different behaviour for the injectors. However, the initial correction learned could change during the lifetime of the vehicle, due to a drift of the injector. Learning control methods are known to obviate to such issue, such as Small Quantity Adjustment learning (SQA) [46], which is a method aimed to determine an actual characteristic curve of the fuel injector, which can be used instead of the nominal curve to operate the injector during small fuel injections. These learning control methods are adjustment functions that demand specific engine conditions regarding engine speed, vehicle velocity, etc. and provided for operating the injector to perform a number of test fuel injections having different predetermined ETs, measuring an actual quantity of fuel injected during each one of the test injections to obtain a corresponding point of the actual characteristic curve. The first test injection is performed with a test ET, an actual fuel quantity that has been injected during the first test injection is measured to obtain an initial point of a characteristic curve representing a relationship between the ET applied to the injector and the fuel quantity which is actually injected by the injector. The ratio between the actual fuel quantity injected and a nominal fuel quantity corresponding to the first test ET is calculated. The calculated ratio is then used to determine a series of corrected ETs for subsequent tests. The new fuel quantities that have been injected during each one of the subsequent test injections are measured to obtain further points of the characteristic curve. The characteristic curve of the fuel injector is modelled on the basis of the obtained further points. The characteristic curve is used to control the operation of the fuel injector. The above described method may be affected by non-linearity errors if the level of injector's drift or fault is high with respect to the test injection.

To correctly estimate the injector drift, a method could be based on the calculation of the actual injected quantity [47]. It is known that modern diesel engines are equipped with an injection system that directly inject the fuel into the cylinders of the engine. The injection system generally includes a common fuel rail and a series of electrically controlled injectors, which are individually located in a respective cylinder of the engine and which are hydraulically connected to the rail through dedicated injection lines. The fuel injection control is an important aspect of the engine management system, in order to ensure the engine performance in terms of available torque and reduced fuel consumption and emissions. Such control includes several strategies, one of which is called Fuel Set-point Adaptation strategy. FSA strategy estimates the injection drift considering the intake air mass and the oxygen concentration in the exhaust gas and stores the fuel quantity drift values in a map, storing

values of the fuel injection quantity drift, with map points being arranged along an x-axis and along a y-axis representing engine operating points. In particular, such engine operating points are defined by different values of engine speed and requested amount of fuel to be injected by the injector. The actual fuel delivered quantity is calculated as in the following equation:

$$\dot{m}_{f\_actual} = \frac{\dot{m}_{air}}{\lambda} \times \frac{1}{\lambda_{ST} \times \rho} \quad (3)$$

where:

$\dot{m}_{air}$ is the intake air measured by the mass air flow sensor

λ is the air to fuel ratio measured by the lambda sensor

$\lambda_{ST}$ is the stoichiometric air to fuel ratio

$\rho$ is the fuel density

The actual injected quantity is then compared to the requested one and the difference calculated, as shown in fig. 2.14.

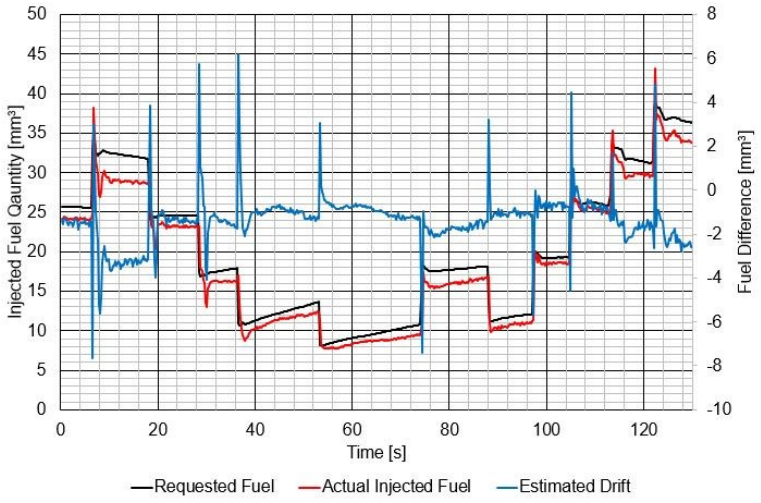


*Figure 2.14 - Estimation of the injector drift, based on estimation of actual injected fuel*

As the figure shows, during the transient between two different fuel demands, the calculation of the injected fuel is not so accurate, mostly due to the delay in the measurement of the oxygen percentage by the lambda sensor. Instead, during steady state conditions the difference is much smaller and more reliable. For this reason, the adaptive map values have to be stored only during nearly stationary conditions (Fig. 2.15).

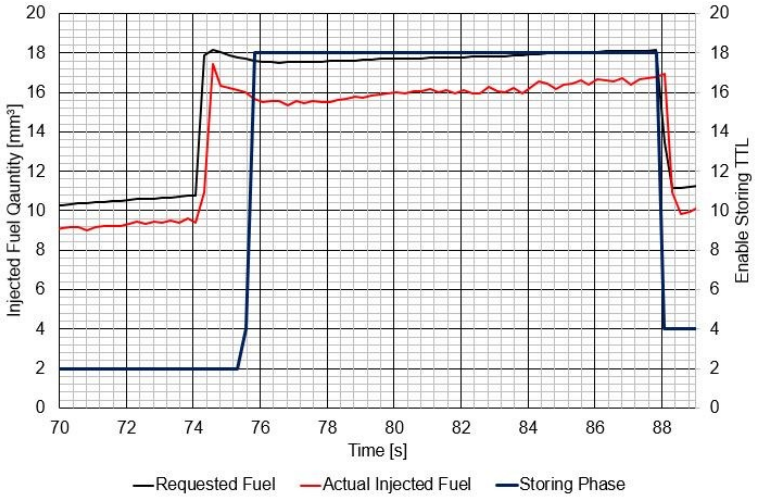


*Figure 2.15 - Enabling of the storing of the fuel difference in the map*

The map points close to a current engine operating point are updated by spreading the estimated fuel injection quantity drift. The stored value is obtained weighing the fuel injection quantity drift with two factors that take into account the relative distances between the learned engine point and the nearby map points.

In order to understand the importance of this factor, a representative test has been made on 1.6, 4-cylinder turbocharged diesel engine. The $NO_x$ and soot concentration (FSN) have been measured and the estimation of the drift in the injected quantity has been changed from -4 to 4 $mm^3$ by steps of 1 $mm^3$. Practically, the zero condition is the one in which the estimation is the correct one and from this an offset has been added or subtracted.

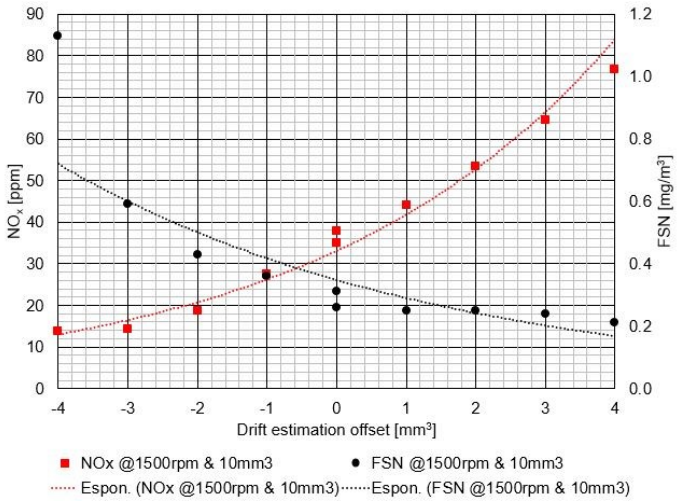


*Figure 2.16 - Emission measurement for different offsets of drift estimation function*

As it is shown in Fig. 2.16, decreasing the offset of the drift estimation means estimate less fuel than the reality and this has an effect on the reduction of $NO_x$ with an increment of soot production (higher FSN). Opposite behaviour is visible with a positive offset that means an estimation of more fuel than reality. The trade-off point is close to the case with zero offset that indicates a good representation of the reality with a best comprise in terms of emissions. This test has best done for an engine speed of 1500 rpm with a fuel request of 10 $mm^3$. Other two conditions have been tested in addition, to underline and verify the adjustment:

- 1750 rpm of engine speed; 15 $mm^3$ of fuel request
- 2000 rpm of engine speed; 20 $mm^3$ of fuel request

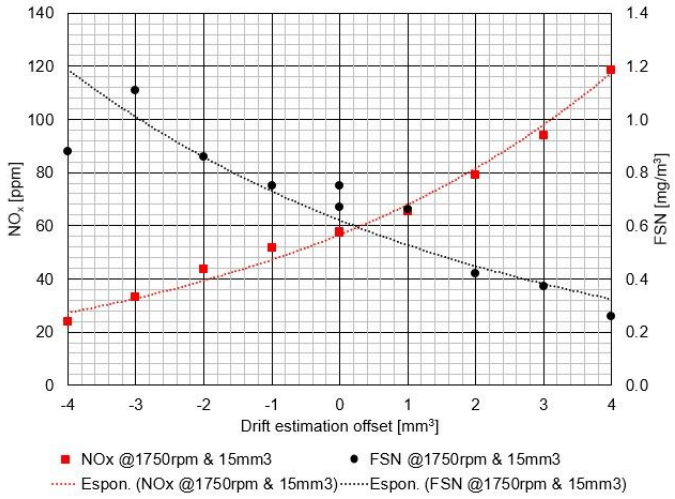


*Figure 2.17 - Emission measurement for different offsets with 1750 rpm and 15 mm³*

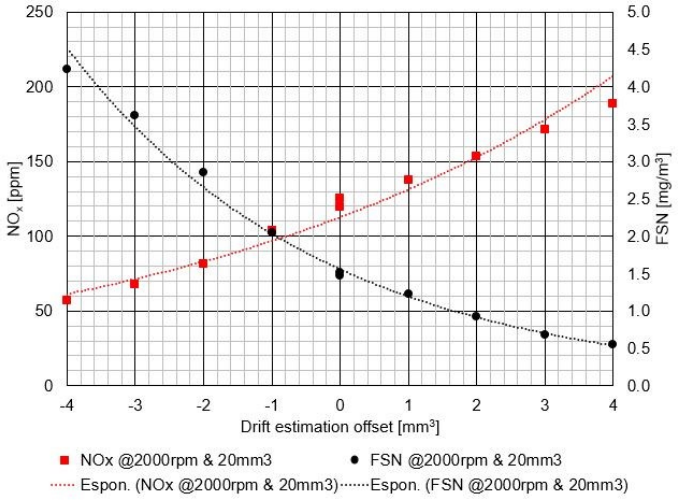


*Figure 2.18 - Emission measurement for different offsets with 2000 rpm and 20 mm³*

Even for these two additional test conditions, the trade-off point is still close to the correct estimation of the drift, without any offset. These tests indicate that a reliable correction of the injection system is really important to maintain the performance and in particular the emissions of the vehicle during the lifetime, avoiding changes in the behaviour due to the ageing of the components.

In last instance, the inaccuracy of the pressure wave propagation in the rail needs to be corrected. The sudden opening and closing of the injector generates a pressure wave that

propagates itself along the fuel line. When a multi injection strategy is adopted, such fluctuation affects the fuel delivery rate of following injection pulses and therefore emission levels, fuel consumption and driveability. A first approach to minimize such problem could be the use of hydraulic systems designed and built specifically to compensate the pressure wave effect. This can be obtained, for example, by modifying physically the fuel line, in order to decrease the wave pressure phenomena by introducing accurate holes or modifying the shape of the fuel accumulator. This approach is limited by the fact that it needs a specific modification of the fuel line for every engine system as well as for each operational condition (for instance injected quantity, rail pressure, distance between injection events, etc.). A second approach is the use of modified injectors that reduce the wave pressure effect using a specific damping volume inside the injector itself. However, this approach requires modifications to the injectors. A further approach is to use a mapping of the effect of the pressure wave in order to apply a control strategy [48] to compensate the injected quantity of the pulses that endure the pressure waves effect. Thus, the objective is to obtain a reliable estimation of the instantaneous pressure value in the fuel line of a fuel injection system, minimizing the impact of the fuel line pressure fluctuations on the injected quantity of each single pulse in a multi-injection pattern without the need to modify mechanically the injector and/or the fuel line itself. The strategy aims to calculate the instantaneous pressure, comparing it with the requested one in order to correct the energizing time taking into account the real feeding pressure of the injector. The instantaneous pressure has been studied by several authors [49 – 51] and pressure measurements can be used to estimate it.

In this section, some of the functions to correct the fuel delivered by the injectors have been discussed. This can give an overview about the efforts needed to overcome the limits of the current fuel injectors. In order to improve these limits, the tolerances of the production process, especially the assembly phase must be reduced. In this way, the behaviour of the injectors will be more easily controllable, reducing the learning functions number used during the lifetime of the vehicle by the ECU.

## 2.3. Press-Fit Processes

In mechanical industry, assembly processes of shafts into hub, based on interference fit, are common. An interference fit, also known as a press fit or friction fit [52] is a fastening between two mating parts that is achieved by friction after the parts are pushed together, rather than by any other means of fastening. There are two basic methods for assembling an oversize shaft into an undersized hole, sometimes used in combination: force assembly and

thermal assembly, by expansion or contraction. The force assembly can be described with at least three different terms: press fit, friction fit, and hydraulic dilation [53]. This kind of method requires an assembly force to axially insert the shaft into the hole and therefore a press system is required. In this section, the theory of the interference pressure and the characteristic aspects will be investigated; then the commercial solutions on the market will be analysed and their limits pointed out.

### 2.3.1. Theoretical aspects of interference fit

When a cylinder and a hole have a certain interference, an interference pressure acting between the two surfaces in contact is determined. This radial stress [54], generally varies along the length of contact and changes in response to the external loading on the assembled parts. The force necessary to produce relative sliding between the parts (also called insertion force), is the product of three terms: the coefficient of friction, the contact surface and the interference pressure.

The simplest case is given by two interfering concentric cylinders of same length (Fig. 2.19).

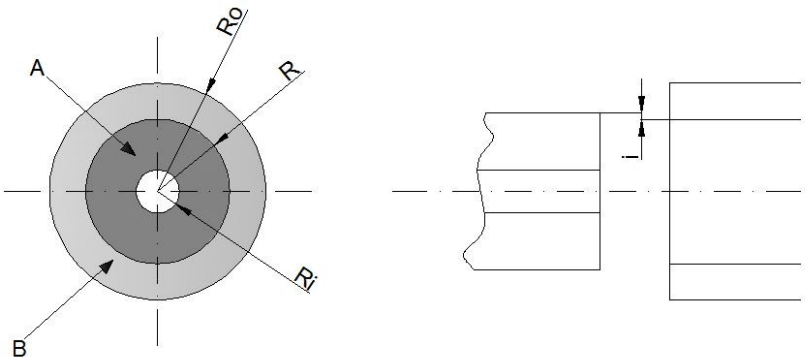


*Figure 2.19 - Interference fit of two cylinders of equal length*

The diametral difference between the shaft (A) and the hub hole (B) is referred to as the interference fit. The geometrical features are defined as follow:

- $R_i$ → internal radius of the inner cylinder
- R → radius of interference
- $R_o$ → external radius of the outer cylinder
- i → radial interference

The radial deformation ($i$) causes an interference pressure, $p$, at the nominal radius, at $r = R$. Consequently, radial and tangential stresses, $\sigma_r$ and $\sigma_t$, are produced. In absence of axial stresses ($\sigma_l=0$) each cylinder is a state of plane stress and the interference pressure is constant along the length of contact. From the cylindrical pressure vessel theory [55], the radial and tangential stresses represent principal stresses can be calculated as follow:

- *Inner Cylinder*

(4) $$(\sigma_t)_i|_{r=R} = -p\left(\frac{R^2+{R_i}^2}{R^2-{R_i}^2}\right) = -pG_{it}$$

(5) $$(\sigma_r)_i|_{r=R} = -p$$

- *Outer Cylinder*

(6) $$(\sigma_t)_o|_{r=R} = p\left(\frac{{R_o}^2-R^2}{{R_o}^2-R^2}\right) = -pG_{ot}$$

(7) $$(\sigma_r)_o|_{r=R} = -p$$

The total deformation is the sum of the deformation due to the tensional state of each cylinder:

(8) $$\delta_{total} = \delta_i + \delta_o$$

Where the decrease in radius of inner cylinder and the increase in radius of outer one are expressed by:

(9) $$\delta_i = R\varepsilon_{ti} = -\frac{R}{E_i}[(\sigma_t)_i|_{r=R} + \upsilon_i p]$$

(10) $$\delta_o = R\varepsilon_{to} = \frac{R}{E_o}[(\sigma_t)_o|_{r=R} + \upsilon_o p]$$

Where:

$E_i$ is the Young's modulus of the inner cylinder

$E_o$ is the Young's modulus of the outer cylinder

$\upsilon_i$ is the Poisson coefficient of the inner cylinder

$\upsilon_o$ is the Poisson coefficient of the outer cylinder

Using the equations (4) and (5) for the above identified tangential stress, the total deformation can be calculated as:

(11) $$\delta_{total} = pRG_t$$

where

(12) $$G_t = \left[\frac{1}{E_i}\left(\frac{R^2+{R_i}^2}{R^2-{R_i}^2} - \upsilon_i\right) + \frac{1}{E_o}\left(\frac{{R_o}^2-R^2}{{R_o}^2-R^2} + \upsilon_o\right)\right]$$

Solving this equation for $\delta_{total}=i$ it is possible to obtain the interference pressure:

(13) $$p = \frac{i}{RG_t}$$

Assuming that the interference pressure remains constant in absence of axial stresses, the insertion force, $F_i$, equals the product of the interference pressure, contact area and coefficient of friction:

(14) $$F_i = (2\pi RL)\mu p$$

When the shaft length is greater than the hub length, which is typical in practice, the assumption of constant interfacial pressure is violated. In this case exists a stress concentration at the contact edges. Far from these discontinuities, if the contact length is long enough, the interference pressure returns to the constant value given by equation (12). Different studies [56 – 58] have reported, by mean of finite element analysis, the pressure distribution for a short collar into a long shaft (Fig. 2.20).

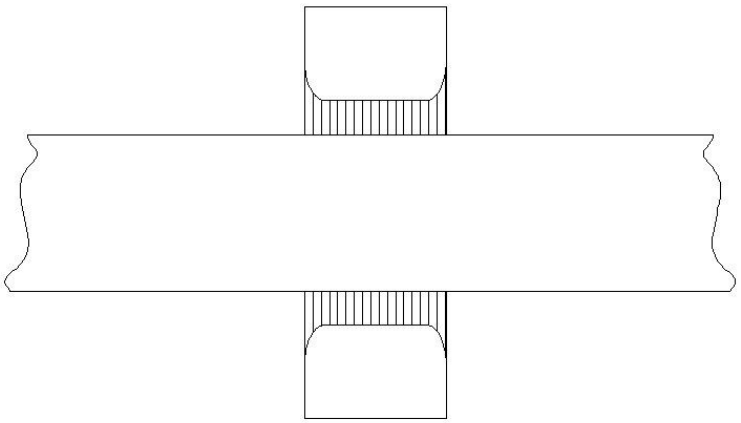

*Figure 2.20 - Behaviour of the contact pressure in case of different length between shaft and collar*

The insertion load is thus calculated by the integration of the interference pressure:

(15) $$F_i = \mu(2\pi R)\int pdz$$

The longer the contact length, the more negligible is the effect of stress concentration on the contact edge.

Nevertheless, even in the case of equal lengths between shaft and hole the axial stresses due to insertion force change the diameter of the components and thus the real interference pressure.

Analysing the forces acting on a section of the inner cylinder (Fig. 2.21a), loaded for a press load insertion, the equilibrium of the forces requires that:

(16) $$p(z) = \frac{R^2 - {R_i}^2}{2R\mu}\frac{d\sigma_i(z)}{dz}$$

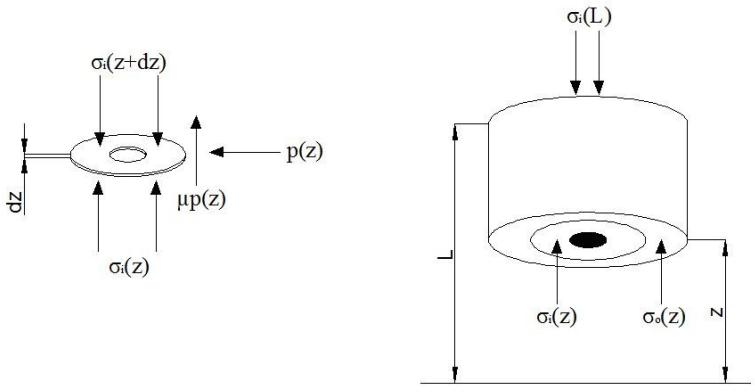


a) b)

*Figure 2.21 - Cross section of the inner cylinder (a) and both shaft and hole (b)*

If a section of both cylinder is taken (Fig. 2.21b), the equilibrium has to be changed as follow:

(17) $$\sigma_o(z) = \frac{A_i}{A_o}[\sigma_i(L) - \sigma_i(z)]$$

where $A_i$ and $A_o$ are the cross-sectional areas.

As the insertion force is given from $A_i\sigma_i(L)$, with the inclusion of axial stresses equation (11) becomes:

(18) $$\delta_{total} = p(z)R\left[\frac{1}{E_i}\left(\frac{R^2 + {R_i}^2}{R^2 - {R_i}^2} - \upsilon_i\right) + \frac{1}{E_o}\left(\frac{{R_o}^2 - R^2}{{R_o}^2 - R^2} + \upsilon_o\right)\right] - \left(\frac{R\upsilon_i}{E_i} + \frac{R\upsilon_o}{E_o}\right)\sigma_o(z)$$

Substituting equations (15) and (16) to (17) the following differential equation for $\sigma_i(z)$ is obtained:

(19) $$\left[\frac{\left(\frac{R^2 - {R_i}^2}{\mu R}\right)G_t}{\mu R}\right]\frac{d\sigma_i(z)}{dz} - \left(\frac{\upsilon_i}{E_i}\frac{\upsilon_o A_i}{E_o A_o}\right)\sigma_i(z) + \left(\frac{\upsilon_o A_i}{E_o A_o}\sigma_i(L) - \frac{\delta_{total}}{R}\right) = 0$$

Solving this differential equation and calculating the solution for $z=L$ and $\delta_{total}=i$, the insertion force is given by:

$$F_i = \frac{i}{R}\frac{A_i E_i}{\upsilon_i}\left(\frac{e^{Kp}-1}{\frac{\upsilon_o A_i E_i}{\upsilon_i A_o E_o}e^{Kp}+1}\right) \quad (20)$$

where:

$$K_p = \frac{\mu L}{R}\left(\frac{\pi R^2}{G_t}\right)\left(\frac{\upsilon_i}{E_i A_i}+\frac{\upsilon_o}{E_o A_o}\right) \quad (21)$$

The insertion loads, calculated without and with, taking into account the Poisson effect due to the axial stresses, are plotted in Fig. 2.22a. The parameters for the calculation are shown in Table 2.1.

*Table 2.1 - Parameters used for the calculation of the insertion loads*

| ***Description*** | ***Symbol*** | ***Value*** | ***M.U.*** |
|---|---|---|---|
| Radius of interference | R | 3 | mm |
| Internal radius of inner cylinder | $R_i$ | 2 | mm |
| External radius of outer cylinder | $R_o$ | 20 | mm |
| Coefficient of friction | μ | 0.2 | |
| Interference | i | 0.025 | mm |
| Young's modulus of inner cylinder | $E_i$ | 200 | GPa |
| Young's modulus of outer cylinder | $E_o$ | 200 | GPa |
| Poisson coefficient of inner cylinder | $\upsilon_i$ | 0.3 | |
| Poisson coefficient of outer cylinder | $\upsilon_o$ | 0.3 | |

The figure depicts how by increasing the contact length the effects of the axial stresses become more important. It is also important to note that without taking into account the axial stresses there is obviously an underestimation of the insertion load, which represents 21% for a contact length of 35mm (Fig. 2.22b). Instead, for contact lengths lower than 10mm, both the insertion load and the error decrease and the axial effects could be neglected.

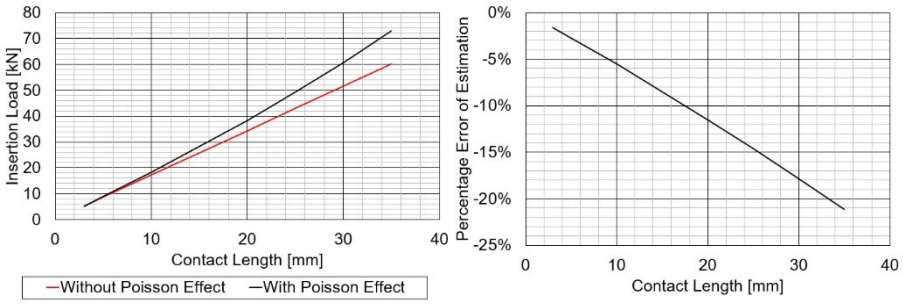


a) b)

*Figure 2.22 - Comparison of the insertion load with or without the consideration of the axial stresses (a). Percentage error between the two calculations (b)*

All the aspects depicted move out from the ideal condition of constant interference pressure, increasing the error in the calculation of the insertion; however, the most critical parameter remains the friction coefficient. The most commonly used friction model [59] is the Coulomb friction model (Fig. 2.23a), which can be formulated as follow:

$$F = \begin{cases} F_c \sin(v), & if\ v > 0 \\ F_{app}, & if\ v = 0\ and\ F_{app} < F_c \end{cases} \tag{22}$$

where $F$ is the friction force, $v$ the sliding speed and $F_{app}$ the applied force. The Coulomb sliding friction $F_c$ is defined as

$$F_c = \mu N \tag{23}$$

where $\mu$ characterizes the coefficient of friction and $N$ the normal load in the contact.

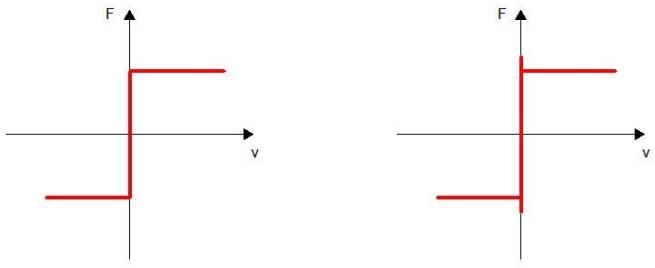


a) b)

*Figure 2.23 - Coulomb friction (a) and Coulomb model with static friction phenomenon (b)*

Using different coefficient for stick and sliding phase, as the reality suggests, the model has been modified as shown in Fig. 2.23b. The Coulomb force is given by [60]:

$$F_c = \begin{cases} \mu_s, & if\ v = 0 \\ \mu_d, & if\ v \neq 0 \end{cases} \tag{24}$$

where $\mu_s$ and $\mu_d$ are the coefficients of static and sliding friction, respectively. The coefficient of sliding friction is smaller than the coefficient of static friction. The influence of different friction coefficient's on the structure response is termed as stiction effect. Friction coefficient is typically a function of the materials, geometries and surface features of the bodies in contact, as well as the operating conditions and environment. Therefore, it easily changes and needs to be considered precisely for different applications. This estimation is often not sufficiently accurate and the insertion load cannot be calculated exactly for obtaining optimal results.

Another problem rises during the insertion when the relative motion of the shaft respect to the sleeve occurs. In the motion with friction between bodies with elastic features a phenomenon called "stick-slip" lead to an intermittent dynamic, characterized from adhesion phase (stick) and sliding. Stick-slip refers to the development of regions of microslip in the surface of interaction between two bodies in contact, when a tangential force is applied to them in order to produce relative motion. As the force increases, the slip region grows and the stick region diminishes [61]. The simplest physical system that can show this phenomenon is a block (Fig. 2.24), sliding on a flat surface, with friction. The block is dragged by mean of a spring with *k* constant with the free ends that moves at velocity *v*.

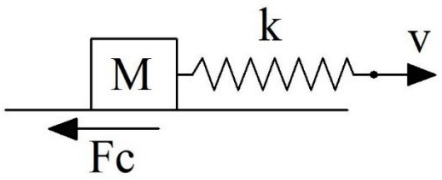


*Figure 2.24 - Mass/spring system with friction*

Solving the motion equation for this system [62], the behaviour of the displacement of the mass ($x$)and the friction force ($F_c$) are shown respectively in Fig. 2.25a and 2.25b.

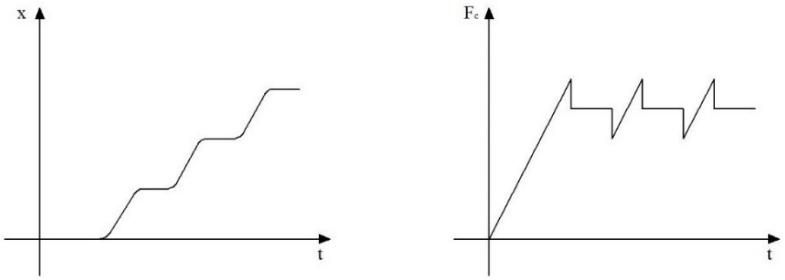


a) b)

*Figure 2.25 – Displacement series (a) and friction load (b) for the mass/spring system*

An accurate press system in production needs to take into account all these aspects in order to control the position precisely during an assembly of components with interference. In the next section, the commercial presses and their limits will be investigated.

### 2.3.2. Limits of the commercial solutions

Commercial presses in manufacturing lines are generally composed by a controller that define the actions to use the actuator, in order to reach the desired output control (Fig. 2.26). In this case the output can be force or position as a parameter of either the assembly or the joint processes.

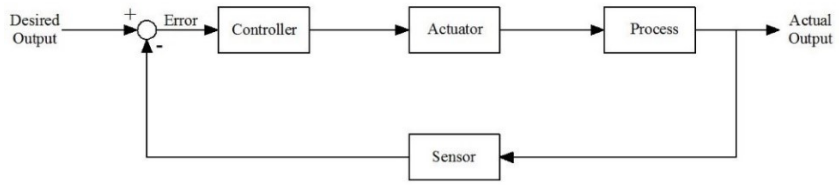


*Figure 2.26 - Block scheme of a press system*

Press actuators can be either pneumatic, hydraulic, electro-mechanic or a mix of these different technologies.

The biggest advantage of pneumatic actuation is its simplicity, meaning its relatively easy to use and install. Their simplicity also results in a low price and small weight. In addition, they have durable components and require only little maintenance. Pneumatic actuators are commonly used in extreme temperatures and other hazardous environments. They are highly safe to use and also operate without using challenging materials, as typically cleaned and compressed air is hard on agent.

One disadvantages of this actuation is that compressed air should be well prepared to meet the requirements. Meet certain criteria, such as dry, clean, and contain the necessary lubricant for pneumatic equipment. Therefore, it requires installation of pneumatic systems are relatively expensive equipment, such as compressors, air filter, lube tube, dryer, regulators, etc. Furthermore, one of the properties of pressurized air is like to always occupy the empty space and the air pressure is maintained in hard work. Therefore, a seal so that air does not leak is needed. Seal leakage can cause energy loss. Pneumatic equipment should be equipped with airtight equipment that compressed air leaks in the system can be minimized. Moreover, pressurized air is easily condensed, so before entering the system must be processed first in

order to meet certain requirements, such as dry, have enough pressure, and contains a small amount of lubricant to reduce friction in the valves and actuators.

In hydraulic actuation, the most important advantage is the force it produces, which can be significantly higher than that of a pneumatic or electric one. They also have high stability and, because of the incompressibility of the used fluids, they can hold a constant force and torque without the need to pump more fluid or pressure to the cylinder. One disadvantage of hydraulic actuators is given by fluid leaks, which leads to a substantial loss in efficiency. Unlike with pneumatic actuators though, the leaks can damage the surrounding system area and components and lead to environmental problems. Also, hydraulic actuation need many other components to operate (a fluid reservoir, motors, pumps, release valves, heat exchangers, noise-reduction equipment), meaning the systems are comparably large and difficult to install.

Both of the before mentioned the technologies have a relatively poor accuracy in the positioning, due to the stick-slip phenomenon that involves both cylinder seals and rod. The seals are installed to avoid the leakage of the operating fluid. They act on the cylinder rod and, due to the different stiffness, the can store more elastic deformation, amplifying the stick phase, as shown in Fig. 2.27.

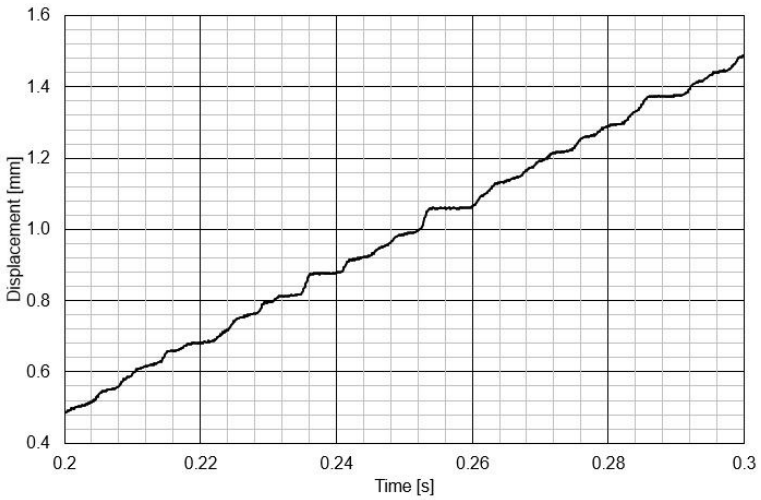


*Figure 2.27 - Stick-Slip effect in a pneumatic press, measured with a differential LDV*

Using electro-mechanic actuators, a good precision-control positioning can be obtained. They can be modified for almost any purpose or force requirement and operate smoothly and with good repeatability. This type of actuation also produces less noise than pneumatic and

hydraulic actuators. They have no fluid leaks, which means they typically pose no danger to the environment. Also, they offer immediate feedback and can be reprogrammed easily in case that problems should occur. In addition, their motion profiles can be fully controlled and encoders can be implemented in order to control position or force. However, the mechanical chain has its inaccuracy and micrometric control of the position is challenging, especially controlling the steps of the electric motor. Electric actuators incorporate other drawbacks; they are usually more expensive than hydraulic and pneumatic actuators and they can also overheat, which can damage the system components.

High accurate positioning devices are piezoelectric actuators using piezoelectric materials as active material and having a specific design to overcome traditional limitations of classical direct piezoelectric actuator, the limited stroke. As classical piezoelectric materials have a strain of 0.1%, it is practically impossible to reach significant stroke without displacement amplification (e.g. 1 mm displacement would require 1 meter of piezoelectric material). The classical solution to reach middle range stroke is to use an amplification system. Two main types of piezo actuators are available: low voltage (multilayer) devices requiring about 100 volts for full motion and high voltage devices requiring about 1000 volts for full extension. The maximum electrical field that can withstand by piezo ceramics is between 1 and 2 kV/mm. In order to keep the operating voltage within practical limits, Piezo actuators consist of thin layers of electroactive ceramic material, electrically connected in parallel, as shown in Fig. 2.28.

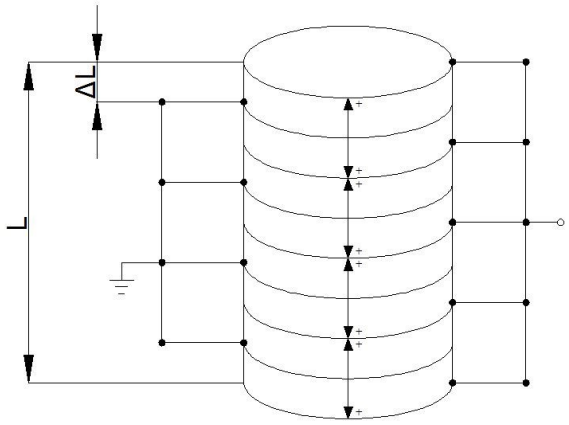


*Figure 2.28 - Electrical connection of the layers of a piezo actuator*

The net positive displacement is the sum of the strain of the individual layers. The thickness of the individual layer determines the maximum operating voltage for the piezo actuator.

High voltage piezo actuators are constructed from 0.5 to 1.0 mm layers while low voltage multilayer piezo actuators are monolithic multilayer designs constructed from 20 to 100 µm layers. Both types of piezo actuators can be used for many applications: in particular, high voltage types can be designed with larger cross-sections for higher load applications, up to several tons, than low voltage ceramics.

Piezo actuators feature no "stick slip" effect and therefore offer theoretically unlimited resolution. In practice, actual resolution can be limited by a number of factors such as piezo amplifier (electric noise results in unwanted displacement), control electronics and mechanical parameters. Nevertheless, piezoelectric actuators are typically used in atomic force microscopes, that require to move distances less than one atomic diameter.

After this general overview of all the main aspects that characterize the assembly process of components with interference, it is quite clear that state of the art solutions cannot manage all the phenomena that take part during the assembly especially in mass production, reaching micrometric accuracy in relative position of the assembled components. For this reason, a new press station for higher quality demands needs to be developed, studying and applying strategies, in order to control these boundaries and phenomena.

In the next chapter, a first detailed numerical study will be highlighted. The gathered information has been used to design an experimental prototype of all-new press station in assembly of sensitive components, able to test different actuations. The results from the experimental study have guided the construction of the full-scale prototype, shown and validated in Chapter 4.

# 3. Characterization of Motion in Interference-Fit

In order to understand the physics of the process and to build up detailed knowledge useful to design an all-new press fit system, numeric simulation can be useful because a good model provides a good representation without the necessity of building multiple prototype stages.

However, the complexity of the given problem makes difficult an accurate mathematical modelling which would be required to describe the geometric dimensions and force relationship, to derive the evolution of the insertion load and the displacement during the press-fitting stroke. For this reason, only a simplified model has been studied by mean of a numeric simulation, then realizing a first prototype to analyse tribological aspects by an experimental approach.

## 3.1. Numeric simulation approach

The simulation of the motion of simplified system has been realized by using Simulink®, a block diagram environment for multidomain simulation and Model-Based Design. It supports simulation, automatic code generation, and continuous test and verification of embedded systems. It provides also a graphical editor, customizable block libraries, and solvers for modelling and simulating dynamic systems

### 3.1.1. Model

The simplified system model, shown in Fig. 3.1, is a mass block $M$ with friction $F_c$, pushed by mean of a spring of constant $k$. The free end of the spring is moved with a displacement $X$.

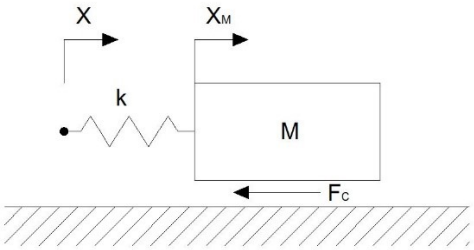


*Figure 3.1 - Schematic of the model used for the simulation*

Two types of conditions have been investigated in detail during this study, changing the velocity of the free end of the spring (Fig. 3.2):

- Constant velocity
- Impulse train of square wave

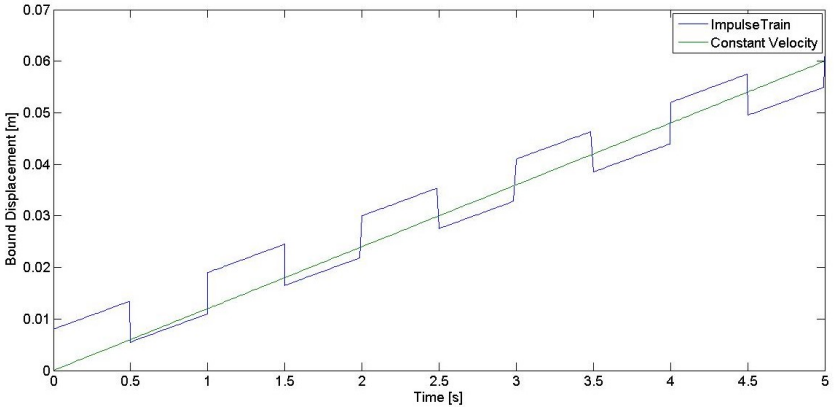


*Figure 3.2 - Bound displacement X at the free end of the spring*

The choice of a comparison between a constant velocity and a dynamic one has been suggested from the literature [63 – 65]. In many positioning devices and manipulators, a way to increase the performances in terms of position accuracy is to drive the device with an impact or, in general, a dynamic force generation. In this dedicated simulation the generation of the load is not possible but a dynamic motion of the free end of the spring can generate a dynamic elastic force by mean of the spring, that can act on the block mass.

The motion equation of the system can be expressed by:

(25) $$M\ddot{X}_M(t) = k[X(t) - X_M(t)] - F_c$$

Where for the friction force $F_c$ the Coulomb model with stiction effect has been used, defining two different friction coefficients for static and dynamic status. The following parameters have been used for the simulation:

*Table 3.1 - Parameters used for the simulation of the mass-spring system*

| ***Description*** | ***Symbol*** | ***Value*** | ***M.U.*** |
|---|---|---|---|
| Block mass | M | 0.1 | kg |
| Spring constant | k | 100 | N/m |
| Coefficient of static friction | $\mu_s$ | 1.1 | |
| Coefficient of dynamic friction | $\mu_d$ | 0.8 | |

Four different cases were studied for a simulation case of 5 seconds, comparing the block displacement in the case of constant velocity with the square wave train with these frequencies:

1. f = 1 Hz
2. f = 10 Hz
3. f = 20 Hz
4. f = 50 Hz

### 3.1.2. Results

In Fig. 3.3 the block displacement for case 1 is shown; with both settings the provided displacements to the free end of the spring, the system shows a typical behaviour characterized from stick-slip phenomenon. No particular differences are visible with the adoption of one displacement law or the other.

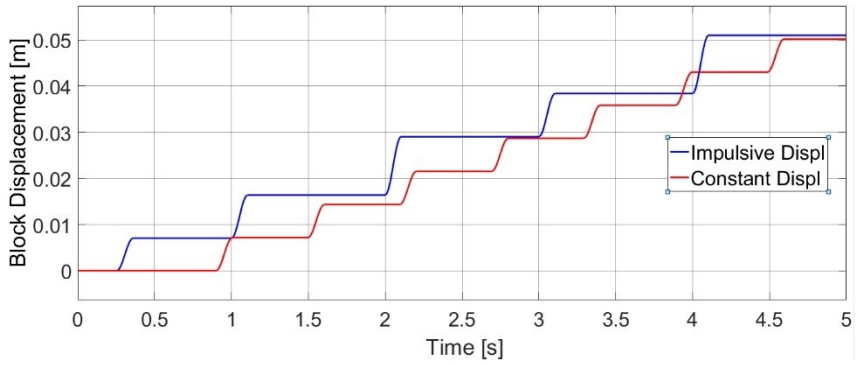


*Figure 3.3 - Comparison of block displacement in constant velocity case and square waves train with a frequency of 1 Hz*

By increasing the frequencies of the square wave to 10 and 20 Hz (cases 2 and 3), a reduction in the amplitude of the stick-slip phenomenon is clearly visible (Fig. 3.4). Calculations [66] demonstrated that oscillations of the normal load could lead to a transition from a state of high-friction stick–slip dynamics to a low-friction smooth sliding state. Manipulation by mechanical excitations, when applied at the right frequency, amplitude and direction, pull the molecules out of their potential energy minima and thereby reduce friction (at other frequencies or amplitudes the friction can be increased).

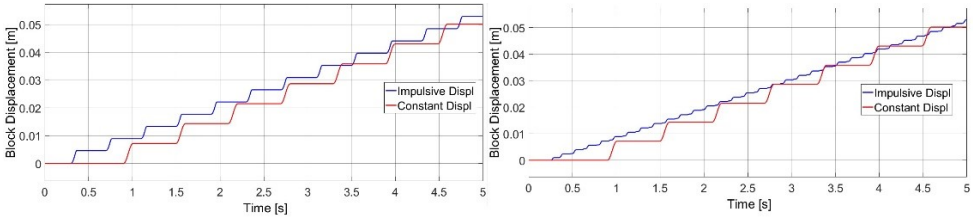


a) b)

*Figure 3.4 - Case 2 and 3, tested with square wave frequency of 10 Hz (a) and 20 Hz (b)*

With this model, using a frequency of 50 Hz the stick-slip is highly reduced (Fig. 3.5) and the block displacement seems to be characterized nearly by a constant velocity (Fig. 3.6).

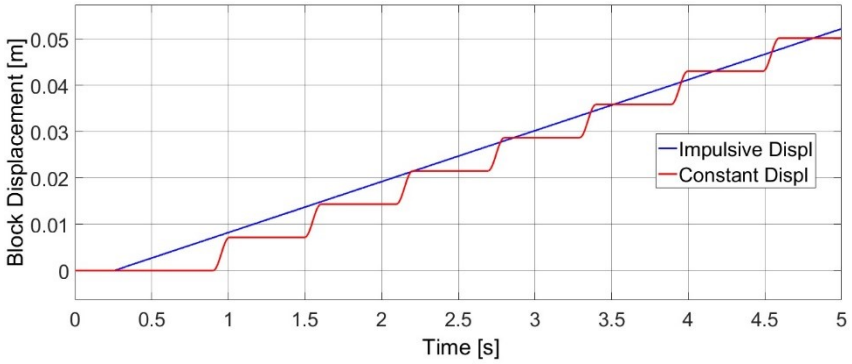


*Figure 3.5 - Comparison of block displacement in constant velocity case and square waves train with a frequency of 50 Hz*

The simulation results indicate the possibility to drive a system dynamically, in order to reduce the effect of the stick-slip phenomenon. Many efforts are needed to solve the equation in the static-dynamic transition region of the friction coefficient; with the addition of the interference pressure and the axial stresses the complexity of the calculation increases and the solution is no longer representative of the real behaviour.

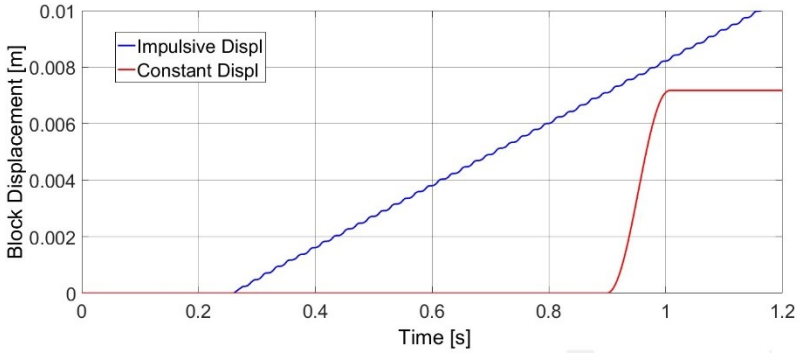


*Figure 3.6 - Particular of block displacement in constant velocity case and square waves train with a frequency of 50 Hz*

For these reasons, an experimental approach has been decided, using an actuator that can be easily driven dynamically till high frequency: a piezoelectric actuator. As explained in the previous chapter, a piezoelectric actuator is a highly accurate positioning device which is not characterized by stick-slip phenomena. In the next section, the main features of the prototype will be discussed and the acquired information highlighted.

## 3.2. Prototype of the Piezo Actuated Press

A piezoelectric press machine was developed for these experiments (Fig. 3.7).

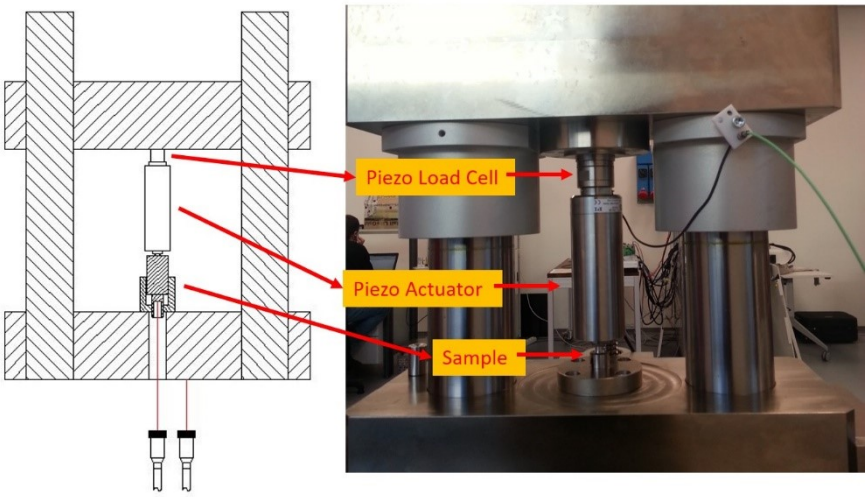


a) b)

*Figure 3.7 - Sketch (a) and picture (b) of the test bench*

The upper supporting plate can be moved, using a screw, connected to a threaded hole, screwed to the supporting beam. The rotation of the screw moves the plate approaching the sample, generating a preload. After that, the two clamps, one for each column, are tightened fixing the supporting plate; now the piezoelectric actuator can be driven. The generated load was measured by means of a piezoelectric load cell located on top of the actuator. The fiber probes of a differential LDV measure the relative displacement and velocity of the plug with respect to the sleeve.

### 3.2.1. Displacement measurement system

A non-contact monitoring system was used to measure simultaneously the relative displacement and velocity between plug and sleeve, more precisely a Differential fiber optic Laser Doppler Vibrometer. DLDV is a non-contact interferometric device particularly fit for differential measurements. It was chosen to avoid measuring the displacement of the press, due to compression and bending of the structure. The use of differential laser Doppler vibrometer is well documented in literature, for example in [67] related to automotive industry.

The first laser beam was pointed at the centre of the plug internal cavity. Ideally, the second beam should be pointed at the sleeve. However, because of optical access constraints, the second beam was pointed at the supporting plate of the test sample. The errors resulting from this installation can be estimated considering the deformation of the support which holds the sleeve under the load applied by the press. Under that load, the support behaves as a beam with two supports loaded at the centre.

In following table, the main parameters used for the calculation are listed:

*Table 3.2 - Parameters used for the calculation of the deflection in the supporting plate*

| ***Description*** | ***Symbol*** | ***Value*** | ***M.U.*** |
|---|---|---|---|
| Height | H | 0.1 | m |
| Width | B | 0.15 | m |
| Length | L | 0.4 | m |
| Young's Modulus | E | 200 | GPa |
| Load | F | 15 | kN |

According to [68], the deflection of the sample support, for a beam with a rectangular section is shown in Fig. 3.8.

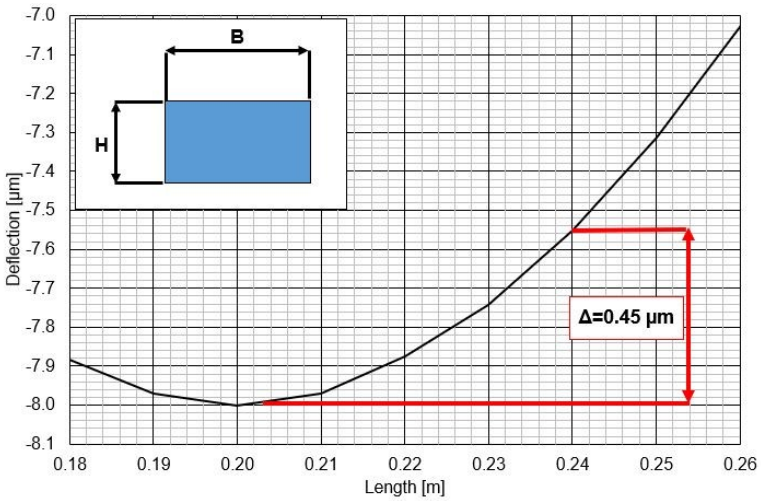


*Figure 3.8 - Deflection of the beam support, loaded at the centre*

The maximum deflection is on the application point of the load, at the centre of the beam, where the first laser beam is pointed. Placing the second laser beam at a distance of 40 mm,

the deflection difference between the two measurement points, thus the error, is around 0.5 μm, within the accuracy of the instrument.

### 3.2.2. Force generation

The piezoelectric actuator was characterized by a multilayer stack of piezo-ceramic elements generating a maximum force of 30 kN and a maximum (free motion) axial displacement of 120 μm. The maximum stroke can be generated without any resistant load against while the maximum load is calculated considering the block condition for which there no motion of the actuator is given (Fig. 3.9).

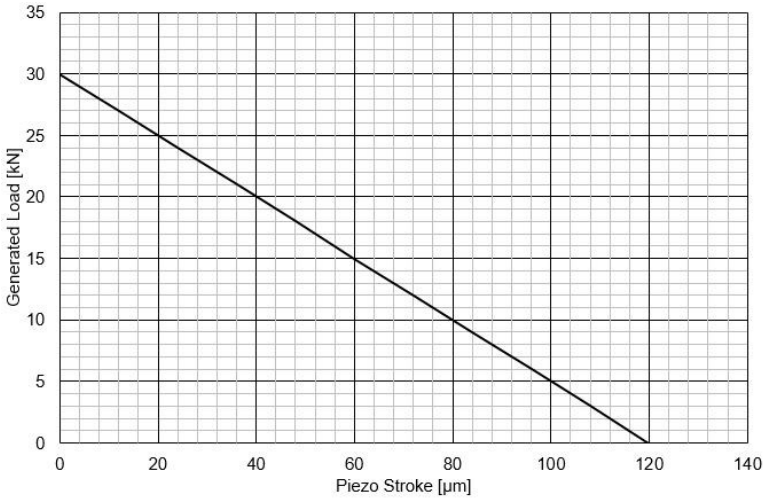


*Figure 3.9 - Characteristic curve of the piezoelectric actuator*

The piezoelectric actuator was in contact with the samples through a spherical tip, generating the mechanical load and consequentially the displacement of the plug into a sleeve.

*Figure 3.10 - Spherical tip of the piezoelectric actuator*

The use of a spherical tip allows to avoid any bending moment acting on the piezoelectric actuator, therefore preventing damages to the actuator.

### 3.2.3. Force measurement system

The selected load cell is a preloaded piezoelectric force transducer link that can measure tension forces up to 20 kN and compression forces up to 75 kN, producing an electrical charge directly proportional to the force applied.


*Figure 3.11 - Load cell*

The force to be measured is transferred to the piezoelectric force transducer elements via the cover plate and base plate of the tightly welded steel housing. The quartz elements produce

an electric charge proportional to the mechanical load. A charge amplifier generates an electric voltage from this charge.

Thanks to the extremely high resolution of the piezoelectric force transducer it is possible to measure a change in force in the order of 1 N under a preload of several tons. This gives high rigidity to the load cell, a sensor with a larger measuring range undergoes less deformation that is a really important, especially considering the limited stroke of the piezoelectric actuator.

### 3.2.4. Acquisition system

The data acquisition system was composed by a National Instrument c-DAQ-9178 chassis, with the following modules (Fig. 3.12):

- Nr. 2, NI 9215, 4 channels, ±10V, 16 bit, Simultaneous Analog Input
- Nr. 1, NI 9234, 4 channels, ±5V, 24 bit, Software-Selectable IEPE
- Nr. 1, NI 9263 4 channels, ±10V, 16 bit, Analog Voltage Output

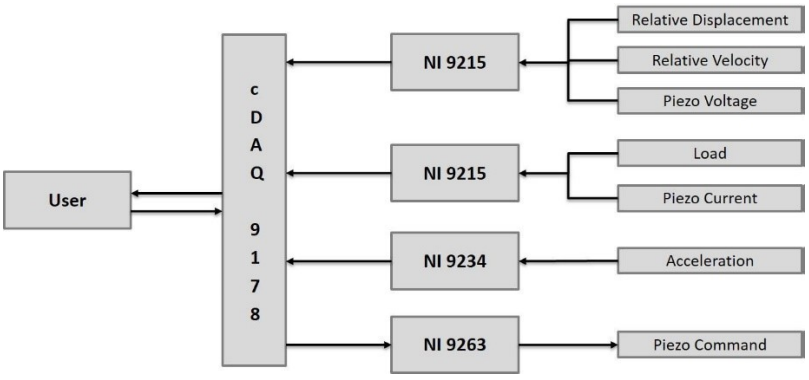


*Figure 3.12 - Block diagram of the acquisition system*

In order to permit the user to select the test parameters and visually monitor the information, an acquisition software interface was developed. Sampling rate was set to 100 kHz. At the end of the test, the acquired data were saved in a file. For every test, the following data were acquired:

*Table 3.3 - Acquired channels specifications*

| ***Device*** | ***Data*** | ***Resolution*** | ***Measuring Range*** |
|---|---|---|---|
| Differential LDV | Relative Displacement | 0.01 µm | ±160 µm |
| Differential LDV | Relative Velocity | 0.001 mm/s | ± 25 mm/s |
| Load Cell | Load | 0.09 kN | 0 – 30 kN |
| Piezoelectric Actuator | Voltage | 0.3 V | ± 1000 V |
| Piezoelectric Actuator | Current | 0.0003 A | ± 10 A |
| Accelerometer | Acceleration | 5.96 $e^{-6}$ g | ± 50 g |

### 3.2.5. Test procedure

All tests were performed operating the piezoelectric actuator in open-loop control [69], increasing the voltage of the piezo actuator till the maximum voltage and measuring all the information in the time domain. From the results of the simulation static and dynamic actuations have been tested. The tests have been performed in a temperature controlled room, with a precision of ± 1 °C. The main purpose of these tests was to characterize the real motion of a test sample, identifying the main features that need to be under control for reaching micrometric accuracy.

## 3.3. Test Samples

The geometry of the test sample is relatively simple: a cylindrical plug of AISI 304 inserted into a sleeve (Fig. 3.13). The aim is to replicate cylindrical elements (shafts) to be assembled by press-fitting into cylindrical seats (holes). The sleeve is a 16 Cr Ni 4 hardened steel cylindrical bushing with an inner collar.

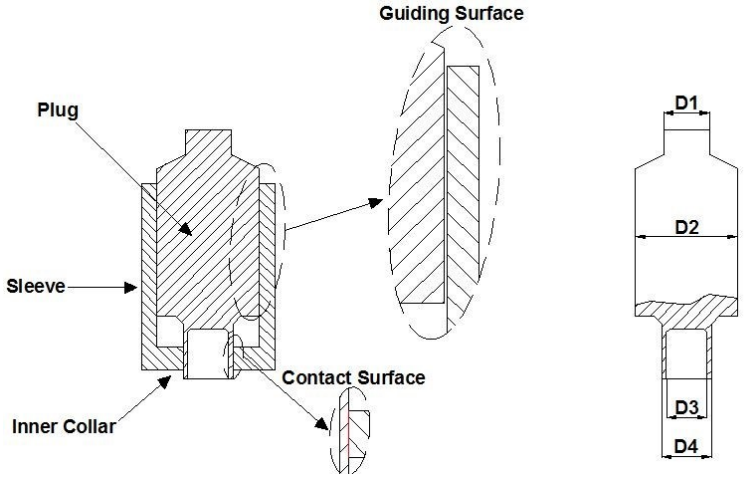


*Figure 3.13 - Schematics of the assembled sample (a) and the plug (b)*

The insertion force is applied on the upper surface ($D_1 = 8^{\pm 0.2}\ mm$). The central part ($D_2 = 11^{-0.12}_{-0.13}\ mm$) of the plug acts as an axial guiding element: no friction occurs along this central part thanks to a clearance of at least 0.02 mm between the sleeve and the plug, higher of the surfaces rugosity ($R_a$=1.6 µm). The hollow part of the plug ($D_3 = 8^{\pm 0.01}\ mm$, $D_4 = 10.1^{-0.03}_{-0.04}\ mm$), is the location where the interference fit process takes place. The parts are manufactured with an interference range between 0.04 and 0.07 mm, which gives an estimated insertion force from 7.2 to 15 kN, using equation (14).

Such a design allows several press tests with a constant interference level to be performed in series without changing samples. Another advantage is to keep always a constant cylindrical surface into contact, i.e. an equal interference length. At each test, the plug advances into the sleeve, but the dimension of the contact area does not vary. With such a design, the contact surface belonging to the sleeve remains the same, while the contact surface belonging to the plug changes when the plug advances in the sleeve.

Before the preassembly of the sample, both plug and sleeves were cleaned by an ultrasonic cleaner, in order to remove dirt particles and grease resulting from the manufacturing process; this allows to improve process repeatability, which may be compromised by varying surface cleanness conditions. Experimentally it is difficult to establish the type of sliding mode [70]. For instance, in thick liquid lubricant films, the friction forces are essentially hydrodynamic or viscous drag forces. However, during the sliding of the plug into the sleeve, it is not

possible to ensure a defined liquid film thickness. Therefore, the intention of cleaning the samples is also to perform tests under controlled conditions, eliminating any variability of the lubrication from part to part.

Before each test sequence, the plug and sleeve are pre-assembled by a manual press, in order to establish the interference between plug and sleeve.

## 3.4. Driving Signal for the Piezo Actuator

Three different driving signals were investigated. The first signal represents the typical continuous stroke of a press; the second signal is the one tested in the simulation of the motion with the simplified model, that has shown good performance in the reduction of the stick-slip effect. The last one consists in a sequence of pulses, but in this case, after each period, the signal returns at zero; in this way, the piezoelectric actuator comes back to its initial position after each period.

### 3.4.1. Constant Slope Driving

The Constant Slope Driving (CSD) signal is shown if Fig. 3.14.

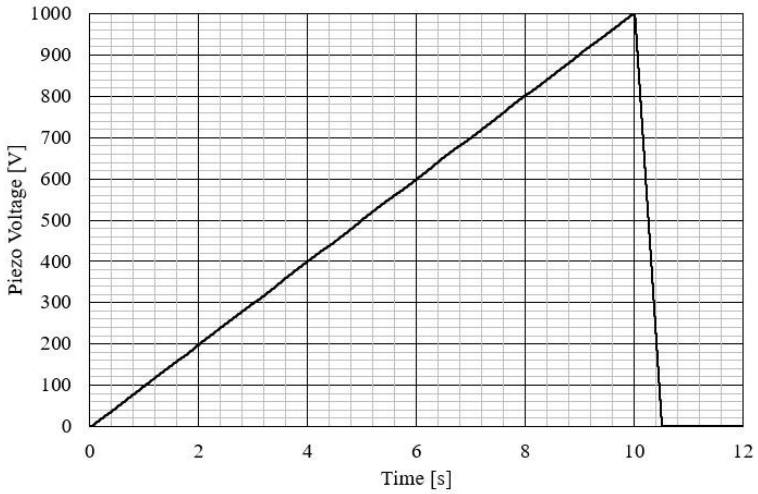


*Figure 3.14 - CSD signal*

The slope can be changed, thus the higher the slope will be, sooner the maximum extension will be reached.

### 3.4.2. Square Wave Train Impulse

The Square Wave Train Impulse (SWTI) signal is explained as follows (Fig. 3.15).

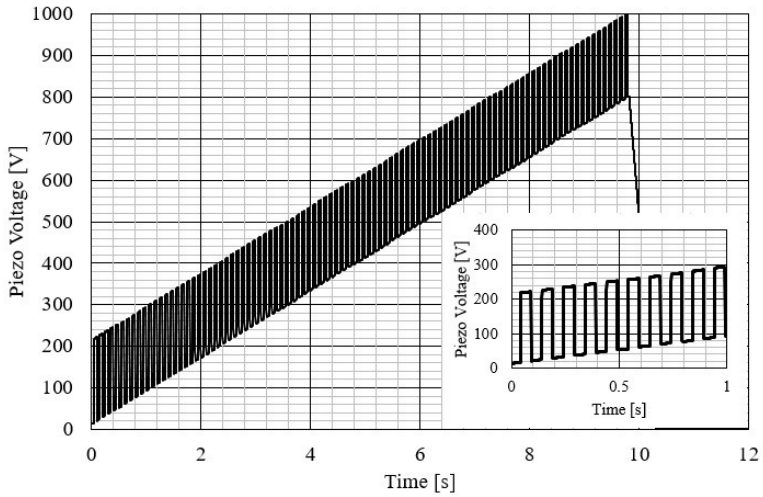


*Figure 3.15 - SWTI driving signal*

This driving voltage is the sum of a constant slope signal and a train of square wave pulses at certain frequency. The base square wave has a constant amplitude (maximum level) and a null minimum level. This signal is then summed to the voltage given from the constant slope signal.

### 3.4.3. Amplitude Modulated Sinusoidal Driving

The Amplitude Modulated Sinusoidal Driving (AMSD) signal is presented in Fig. 3.16.

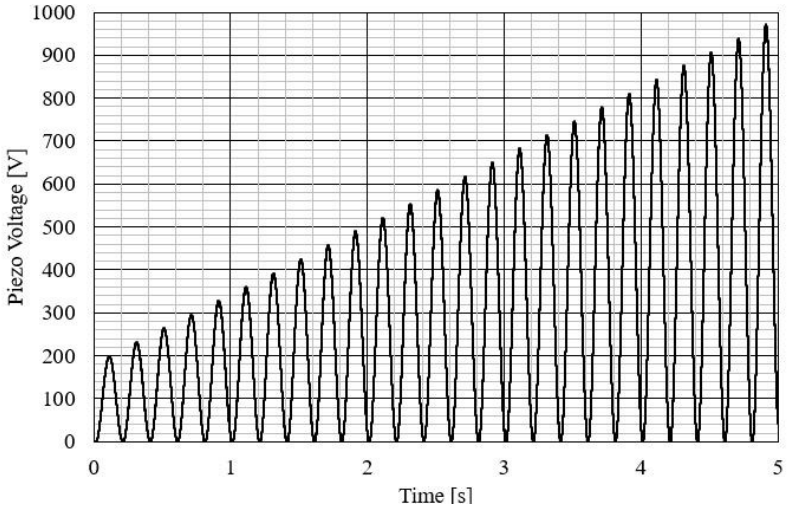


*Figure 3.16 - AMSD signal*

The driving voltage is a sinusoidal wave which amplitude increases linearly with time. The minimum of the voltage for every period is 0 V. Such highly dynamic driving signal permits a different approach because the piezo actuator returns to its initial position at the end of each period, allowing a step-by-step process.

## 3.5. Results

When a CSD signals is applied (Fig. 3.17), several phases of the press-fit process can be observed. During an initial phase (1), an elastic compression of the sample and the structure occurs. When the static friction force is exceeded, the relative movement of the two pre-assembled part starts. This causes a sudden decrease of the load, due to the change from static friction to dynamic friction. After a short transient, the force remains almost constant for all the remaining stroke of the actuator (2), as it is typical of sliding friction. At t=10 s the driving voltage is brought back to 0 V in 0.5 s: the load applied to the sample is released (3). The initial elastic deformation obtained by preloading the system, $F(t=0)$=3.8 kN, is partially recovered at the end of the test, $F(t=12)$=1.8 kN. This initial elastic deformation comes from both the compression and the bending of different parts (sample, structure and actuator). The elastic deformation must be taken into account otherwise a systematic error will arise in the final positioning of the plug after releasing the press load.

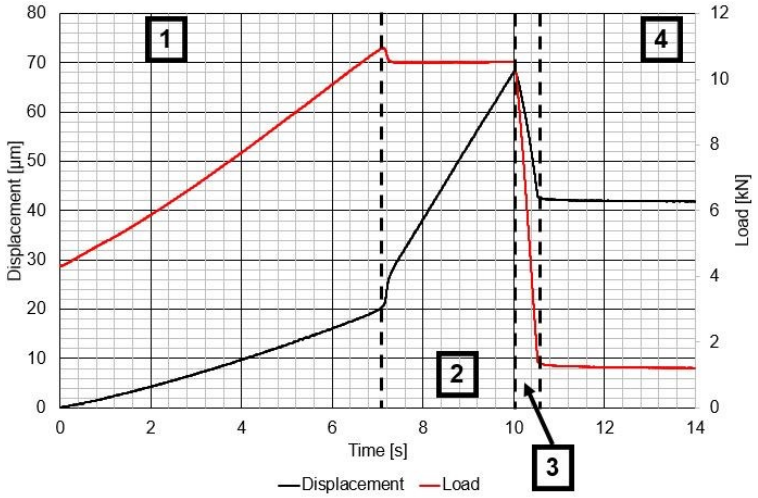


*Figure 3.17 - Load (red) and displacement (blue) during a test with CSD signal*

The slope of the displacement during the phase of irreversible motion, in other words the insertion velocity, was calculated (14.9 µm/s) and then compared to the velocity of free stroke of the piezo actuator, driven with the same voltage (no resistant load) which is 14.3 µm/s (Fig. 3.18).

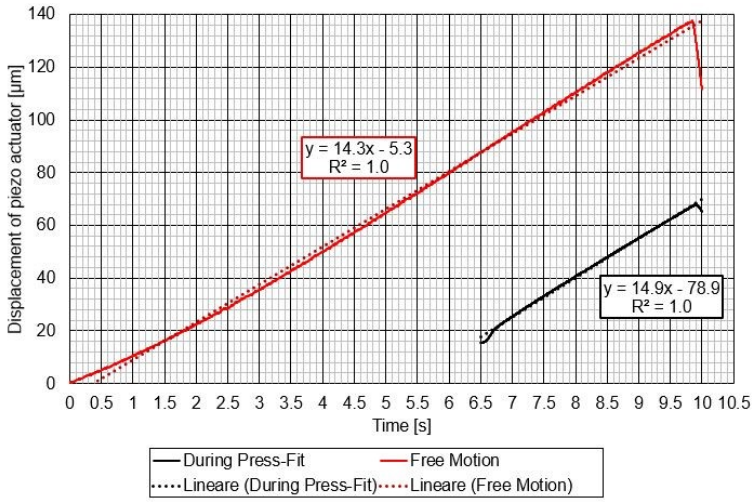


*Figure 3.18 - Comparison of the displacement curves during two different tests: CSD signal test and free motion of the piezo actuator*

The velocity is almost the same and it demonstrates that the irreversible motion occurs. Thus, the relative velocity could be used as an indicator of the effective insertion of the plug.

The accurate detection of the start of the relative motion is a necessary condition to obtain an accurate final positioning. The more precise the detection is, the more accurate the positioning will be.

Driving the piezoelectric actuator with SWTI signal, Fig. 3.19 shows that the main features are the same seen with CSD signal; no particular differences are visible especially considering that, with these samples, the stick-slip effect between plug and sleeve is not evident.

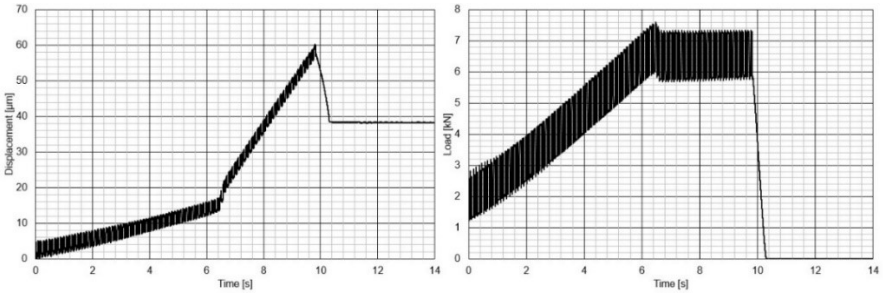


a) b)

*Figure 3.19 - - Displacement (a) and Load (b) measured during an SWTI driving of the piezo actuator*

A measurement (displacement and load) for an AMSD signal test is reported in Fig. 3.20.

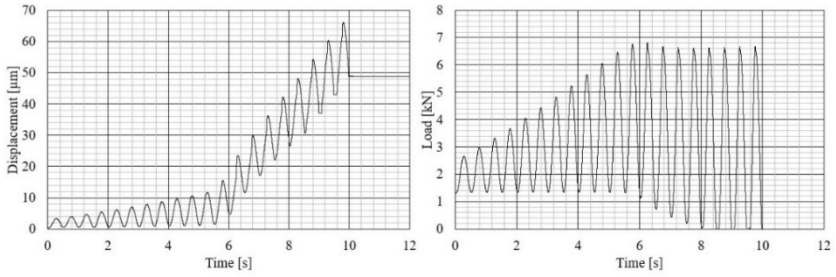


a) b)

*Figure 3.20 - Displacement (a) and Load (b) measured during an AMS driving of the piezo actuator*

For the first cycles ($t < 6s$), the actuator strokes do not generate load levels larger than the static friction force. Therefore, the cycles are exclusively composed of elastic deformation and discharge with no irreversible relative motion of the plug into the sleeve. Indeed, the load and the displacement return at their initial values at the end of each period. When the static friction force is exceeded ($t = 6s$) the load and the displacement signals do not return back to

their initial values at the end of the loading cycle: an irreversible motion has occurred. The ongoing plug insertion during the dynamic press-fitting process can be evaluated through observing the displacement at the end of each loading cycle. Therefore, even in this case, it is crucial to determine the start of the irreversible movement: one indicator could be the reduction of load.

The results of the experiment show that the elastic deformation has a substantial influence on the final positioning uncertainty. For this reason, it is important to exactly identify the start of the relative motion, i.e. the transition from static to dynamic friction. For the constant slope driving of the piezo actuator, a run-in phase during which the friction coefficient changes from the static value to the dynamic was observed.

Also, for the amplitude modulated sinusoidal driving, the beginning of the insertion can be identified through the envelope of the minima of the pulsating force signal. The identification of the start of the irreversible relative displacement between plug and sleeve opens possibilities to develop an interference press fit achieving micrometric accuracy.

In particular, based on the knowledge acquired by these fundamental experiments, in the next chapter, two different closed-loop algorithms controls for the piezoelectric actuator will be implemented in the electronic system management. The evaluation of the error in the final positioning will be investigated more precisely as well as the error in a specific functional performance which may characterize the component being assembled more accurately.

# 4. Full Scale Prototype Press

The first tests made with the piezoelectric actuator have determined that the two key elements for the realization of an accurate press-fitting process are:

a) the accurate detection of the start of the irreversible relative motion of the mating parts

b) the compensation of the spring-back effect

In order to develop a smart automatic press-fit station, a new prototypal version has been developed, based on the findings of the initial studies and the corresponding analysis [71]. Such a design has permitted to generate automatically the preload and to actuate the piezoelectric device, in order to reach the selected setpoint. In this chapter, the new configuration will be highlighted and the incorporated closed-loop controls, based on the previously mentioned driving signals, explained in detail. These two control models will be compared against, to choose the one that assure the best performances in terms of positioning accuracy.

## 4.1. Configuration of the Press-Fit Station

A schematic drawing of the upgraded automatic press-fitting station is provided in Fig. 4.1. The hybrid actuator consists of the piezoelectric device mounted in series to a hydraulic cylinder with a maximum stroke of 200 mm and maximum force of 42 kN. The piezoelectric element and the hydraulic cylinder are mechanically linked by means of a piezoelectric load cell which allows to measure the force generated by the press, both in quasi-static and in dynamic conditions.

The actuator acts on a axially guided punch in order to avoid radial loads, which could damage the actuator. The punch and the axial guide are not represented in the Fig. 4.1 in order to simplify the schematic drawing.

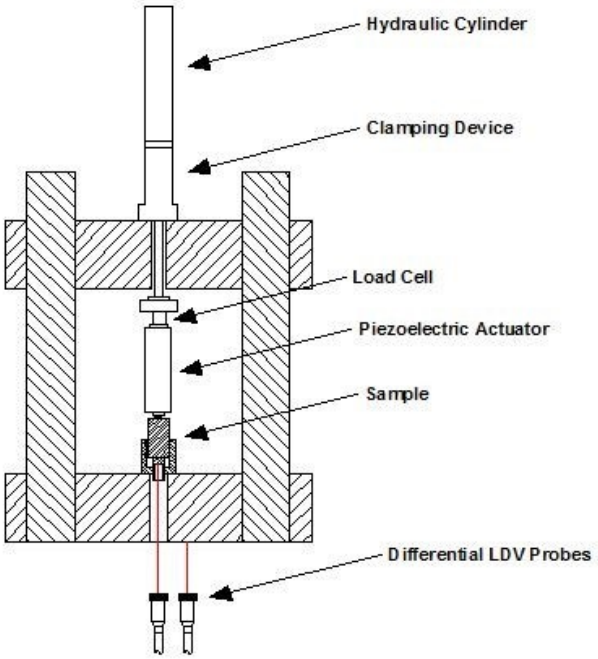


*Figure 4.1 - Schematic of the press-fit station*

### 4.1.1. Mechanical concepts

The core element of the press prototype remains the piezoelectric actuator. In order to overcome the main disadvantage of these devices, i.e. the limited stroke, a hydraulic cylinder has been added. Positioning devices combining a piezoelectric element with a large operation range actuator have been documented by several authors [72 – 74]. For our purposes, a similar approach is used to realize a hybrid press unit.

The hydraulic cylinder is equipped with a clamping device which can lock the rod of the hydraulic actuator at a given position. The clamp works mechanically by frictional contact: a spring acts on a clamping sleeve which holds the rod radially by friction. Instead the hydraulic releasing pressure acts on the clamping sleeve, lifting it against the resistant force of the spring. When the cylinder is clamped, it behaves as a fixed reference frame for the piezo-actuator. In this condition, only the stroke of the piezo-actuator is permitted.

The proposed press-fit station works through several phases, in which either the hydraulic cylinder or the piezoelectric actuator is used. The entire pre-loading of the sample is done by the hydraulic actuator. After this initial phase, by blocking the rod motion with the clamping

device, the piezoelectric actuator is used to perform the plug insertion, down to the required set-point.

Fig. 4.2 depicts the driving process of the press-fitting station where $X$ is the axial position of the plug with respect to the sleeve, at the beginning ($X_{initial}$) and at the end of the test sequence ($X_{final}$).

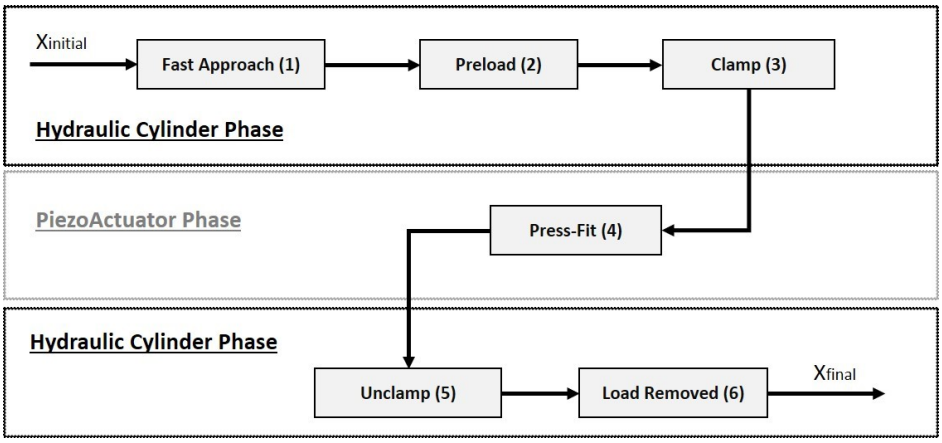


*Figure 4.2 - Test sequence*

The driving process can be described as follows:

- **Approach**: The cylinder is guided near the top of the sample with a position control strategy.
- **Preload**: The preload is generated by the hydraulic cylinder with a load control strategy.
- **Clamp**: The clamping device brakes the cylinder to block the motion of the rod.
- **Press-Fit**: The piezo performs the press-fit until the position set-point is reached.
- **Declamp**: The cylinder clamp is released: the motion of the rod is permitted again.
- **Load Removed**: The preload is removed: the sample returns to a free-load condition.

### 4.1.2. Electric/Electronic hardware

#### 4.1.2.1. Sensors

The position of the press punch is controlled by mean of a potentiometer position transducer. The operating principle is displayed in Fig. 4.3; the output voltage is linearly proportional to the displacement thanks to the sliding contact that changes the resistance of the circuit.

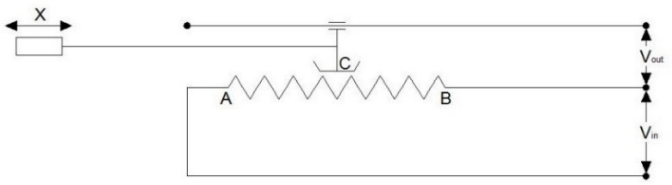


*Figure 4.3 - Operating principle of a potentiometer position transducer*

This kind of transducer is affected by a signal noise related to the ageing of the sliding contacts, thus decreasing its accuracy. Anyway, for the approach phase no extremely high accuracy is needed.

The force is controlled with the same load cell used in the piezo actuated prototype as well as the relative position and velocity during the press-fit phase with the fiber optic differential LDV. In this instrument, the measurements of velocity and displacement are independent: in fact, velocity is obtained by demodulating the Doppler beat signal whereas the displacement comes from a fringe counting [75]. With this technique, the displacement is measured with a remarkable resolution, down to a fraction of the laser wavelength $\Lambda$ (in this case a laser He-Ne having $\lambda$=632 nm).

The working oil was supplied at the press-fit station and the pressurization of the internal circuit commanded by the bench, using the control software.

#### 4.1.2.2. Test bench control system

The control unit used is a National Instruments embedded real-time controller for advanced control and monitoring applications, called cRIO (compact Reconfigurable Input Output). The used cRIO 9024 combines a real-time processor with an 800 MHz CPU and a reconfigurable Field-Programmable Gate Array (FPGA) within the same chassis for embedded machine control and monitoring applications.

The cRIO controller features two processing targets:

1. a real-time processor for communication and signal processing
2. an FPGA for implementing high-speed control and customized timing and triggering directly in hardware

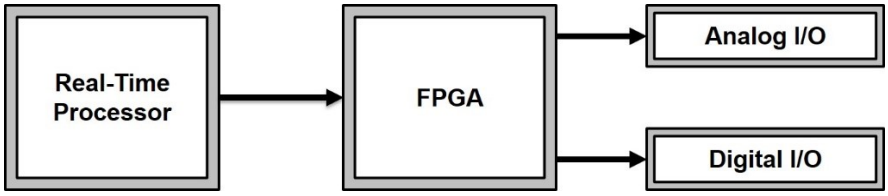


*Figure 4.4 - Architecture of a cRIO*

Another advantage of this architecture is the modularity of the interfaces with the real world. Indeed, cRIO offers a series of modules, for connection with sensors or buses and providing analog and digital I/O. In the presented layout, the following modules, have been installed:

- Nr. 2, NI 9215, 4 channels, ±10V, 16 bit, Simultaneous Analog Input
- Nr. 1, NI 9263 4 channels, ±10V, 16 bit, Analog Voltage Output
- Nr. 1, NI 9421, 8 channels, 24 V, 100 µs, Digital Input
- Nr. 1, NI 9401, 8 Bidirectional Channels, 5 V/TTL, 100 ns, Digital I/O
- Nr. 3, NI 9472, 8 channels, 24 V, 100 µs, Digital Output

The above-mentioned control system is able to control the valves for the pressurization of the hydraulic circuit, the proportional valve of the cylinder, that drives the motion of the rod, acquire all the analog signals necessary for the position control and generate the driving voltage for the piezo.

The accuracies of the acquisition chain of the inputs are shown in Table 4.1:

*Table 4.1 - Measurement devices used for feed-back control in the press-fit station*

| ***Device*** | ***Input quantity*** | ***Accuracy*** | ***Resolution*** | ***Measuring Range*** |
|---|---|---|---|---|
| Differential LDV | Relative Displacement | 2% | 0.01 µm | ± 160 µm |
| Differential LDV | Relative Velocity | 2% | 0.03 mm/s | ± 50 mm/s |
| Load Cell | Load | 1% | 0.09 kN | 0 – 30 kN |

## 4.2. Control Models

Starting from CSD and AMSD driving signals and their specific characteristics shown in the tests with piezo actuated press, two alternative position control strategies have been developed. The first approach tries to improve the performance of state of the art presses, in which the progression of the punch is monotonic. The second algorithm follows a different approach, using a dynamic actuation that permits to control the status of the assembly after each operational period.

### 4.2.1. CSD control loop

In this closed loop control, the feedback control variable is the irreversible relative motion $X(t)_{irr}$; this quantity is indirectly measured by acquiring the total relative motion and subtracting the spring-back effect. Such a procedure needs the precise measurement of the applied force, which allows to detect the onset of sliding between the two parts.

The detection of the start of the irreversible relative motion is based on the analysis of the load time history $F(t)$. In Fig. 4.5 the measured load history is shown, compared with the theoretical one, that follows the Coulomb model of friction with stiction. When considering the ideal Coulomb model, the transition from the static to the dynamic friction coefficient is instantaneous. However, several authors [76 – 77] have published that such a transition in a real process is not abrupt. Indeed, a continuous transition of the friction coefficient from static to dynamic exists. This represents a typical transient situation, called run-in phase, which always occurs before reaching the steady state dynamic friction during the sliding motion of two surfaces above each other.

During the movement, the beginning of the irreversible relative motion between the parts occurs and the current assumption is that the starting point of the irreversible motion is defined by the inflection point of the run-in phase.

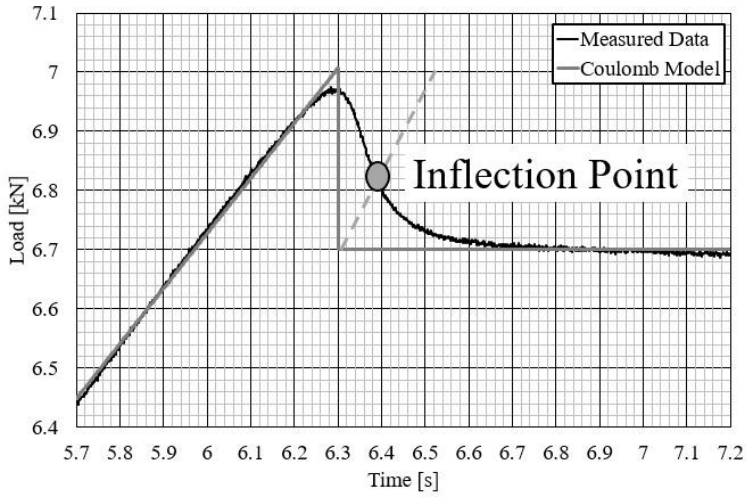


*Figure 4.5 - Measured load time history and Coulomb friction model. Evaluation of the inflection point corresponding to the assumed start of the relative motion*

The implemented controller is based on a discontinuous-action control method. The control loop presented is a two-position (on-off) loop, thus the controlled action can only be activated or deactivated. The active control variable is the supply voltage of the piezo actuator, which varies during the process, following the assigned slope. The voltage increases and the displacement of the piezo actuator follows with it. The controlled variable is supplied till the difference (error *e*) between the setpoint and the measured irreversible displacement is equal to zero.

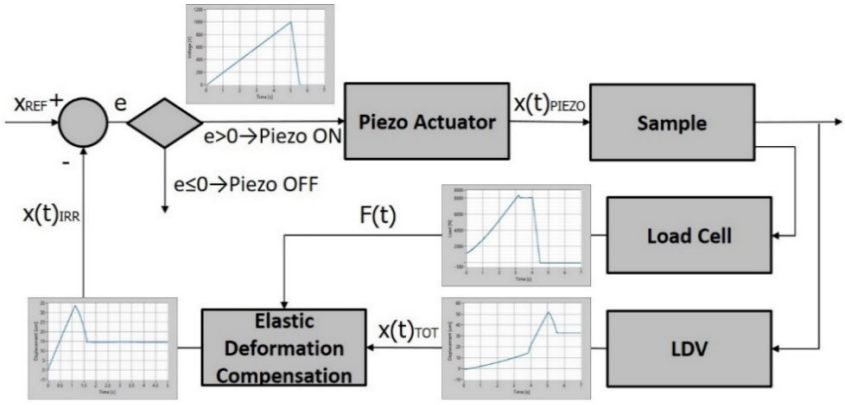


*Figure 4.6 - Workflow of the control loop algorithm for the Constant Slope Drive*

Figure 4.6, *X(t)* represents the axial displacement of the plug with respect to the sleeve, *F(t)* the insertion force and *e* the difference between the set-point $X_{REF}$ and the irreversible displacement $X(t)_{IRR}$.

As shown in Figure 4.7, the control of the observed error with respect to the set-point is done within the FPGA environment, while the inflection point calculation is performed in the Real-Time environment.

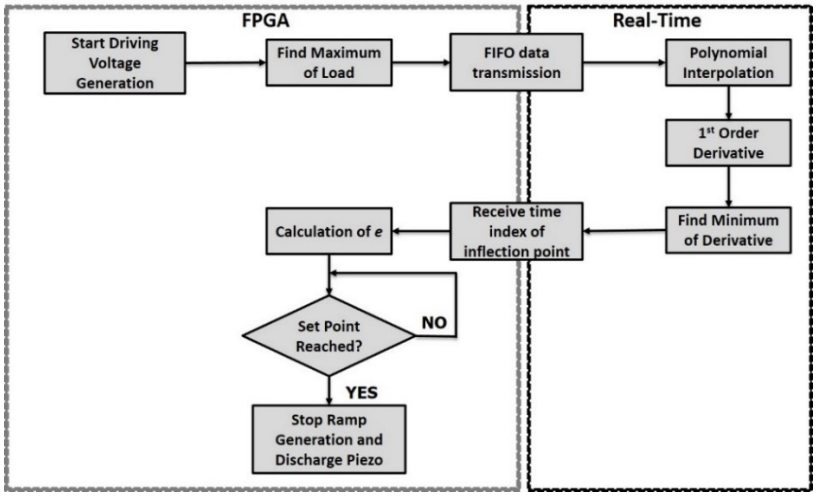


*Figure 4.7 - Schematic of the implementation of the control loop for the Constant Slope Driving*

### 4.2.2. AMSD control loop

Based on the results and the analysis of the previous tests, it is reasonable to divide the load history in three different phases, as shown in Fig. 4.8:

1. **Elastic cycles**: the piezo stroke (and load) is not enough to exceed the static friction resistance. These cycles are composed of an elastic deformation and a return to the initial state. Thus, at the end of every cycle, the load returns to its initial value.
2. **Transition cycle**: during this cycle, the static friction force is exceeded causing an irreversible relative motion.
3. **Press-fitting cycles**: by further increasing the stroke, the plug continues its progression inside the sleeve. The load value decreases at the end of each cycle until it eventually reaches the no load conditions (0 N). Due to the irreversible motion, the plug has changed its position, increasing the recovery of the elastic deformation during the discharge phase.

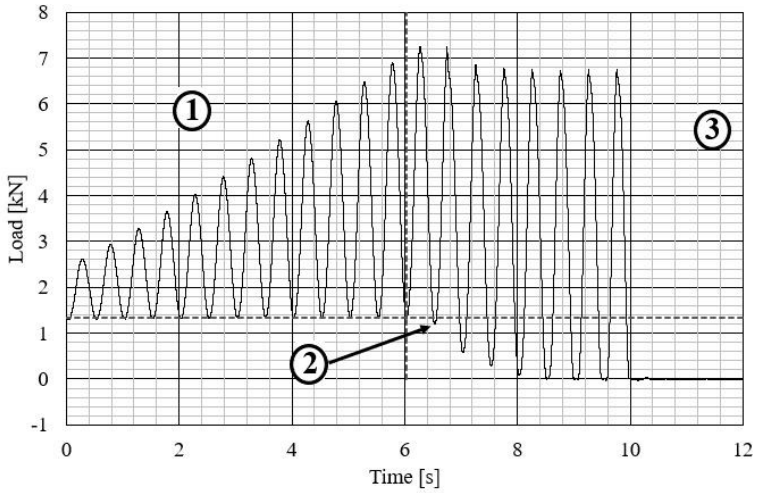


*Figure 4.8 - Different phases of the load history during a typical AMSD test*

The starting point of the irreversible movement is characterized by a load reduction at the end of an AMSD cycle. The algorithm is shown in Fig. 4.9 and it was implemented entirely in the FPGA environment of the controller.

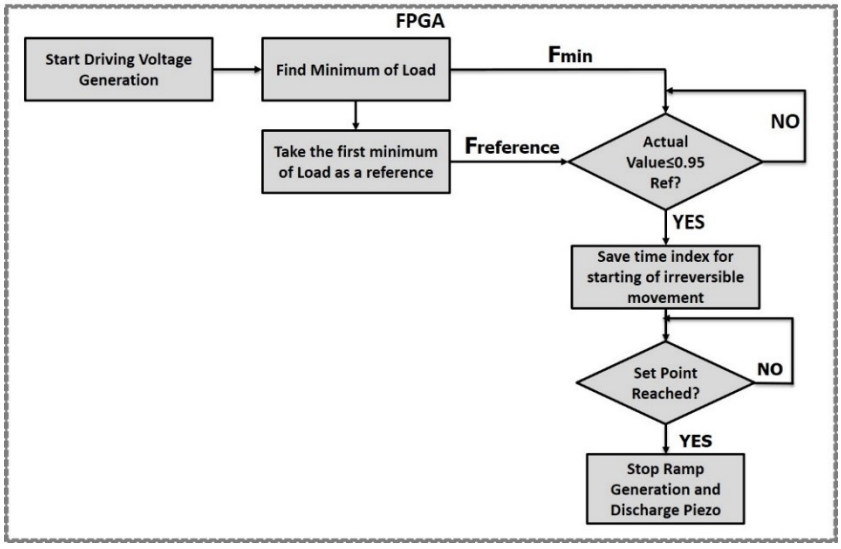


*Figure 4.9 – Initial workflow of the algorithm for AMSD signal*

Dedicated tests have indicated that during the elastic cycles phase, a small increase in the displacement occurs (Fig. 4.10).

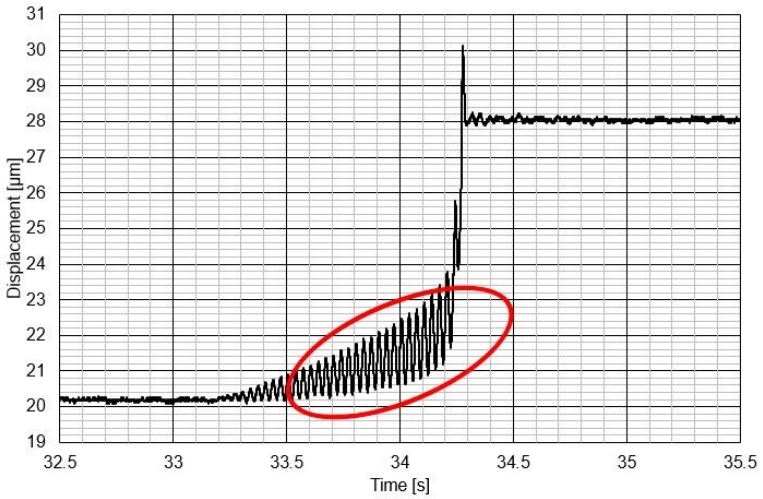


*Figure 4.10 - Increment of the displacement during elastic cycles*

Initially, this rise of the displacement has been associated with an elastic phenomenon. In order to better enquire into this topic, some tests have been realized without reaching the static friction load, thus remaining in the elastic field; in principle, no relative motion should be observed. However, experimental evidence is different: in Fig. 4.11, the piezo actuation phase shows a small drift of the displacement around 1.3-1.4 µm. By measuring the final position at the end of the test sequence, after the removal of the load, an irreversible displacement of 1.4 µm was indeed measured and verified. These results show that even without reaching the static friction force a small displacement occurs.

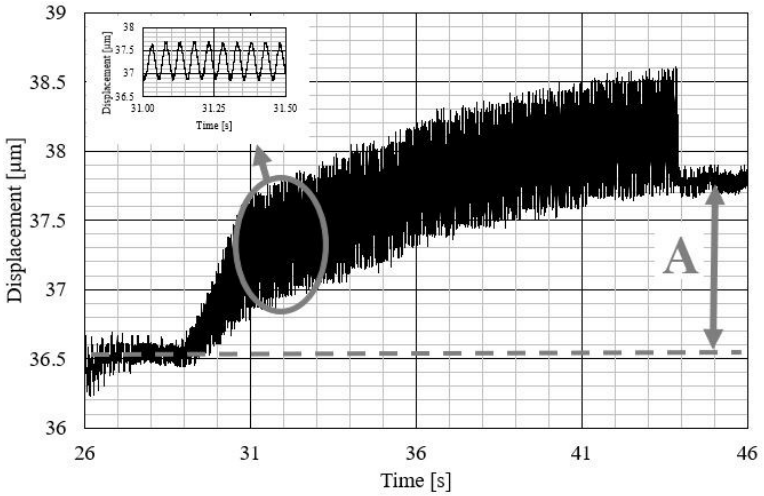


*Figure 4.11 - Pre-sliding phenomenon measurement with $F_{Piezo}$=20 Hz*

This so called “pre-sliding” has already been reported in [78]. The study reveals two sliding friction regimes:

- Pre-sliding regime
- Gross sliding regime

In the pre-sliding regime, the adhesive forces, owing to asperity contacts (surface roughness), are dominant and the friction coefficient, which according to the Coulomb model should be constant, actually changes in function of the displacement. This is due to the fact that the asperity junctions on rough surfaces at micrometric scales deform elasto-plastically, thus behaving as nonlinear hysteretic springs. With the increasing of the displacement and of given force, more and more junctions break and have less time to reform, resulting in gross sliding regime.

The pre-sliding is therefore a hysteretic behaviour [79 - 80] and it arises primarily from micro-slip, that is, the breaking of adhesive contacts. The intensity of this effect with respect to the elastic deformation depends primary on the tangential stiffness of the asperities which overall determine the extent of maximum deformation before slip starts. This behaviour can also be modelled discretely by a parallel connection of Maxwell-Slip elements [81]. During the pre-sliding phase, the shear stress between two contacting surfaces is not large enough to break the contacting linkage. The behaviour during the stiction phase can be modelled by a nonlinear dynamic system.

Thus, after considering this phenomenon which affects the overall relative motion on micrometric scale, the control algorithm was modified accordingly, in order to compensate this effect, as shown in Fig. 4.12.

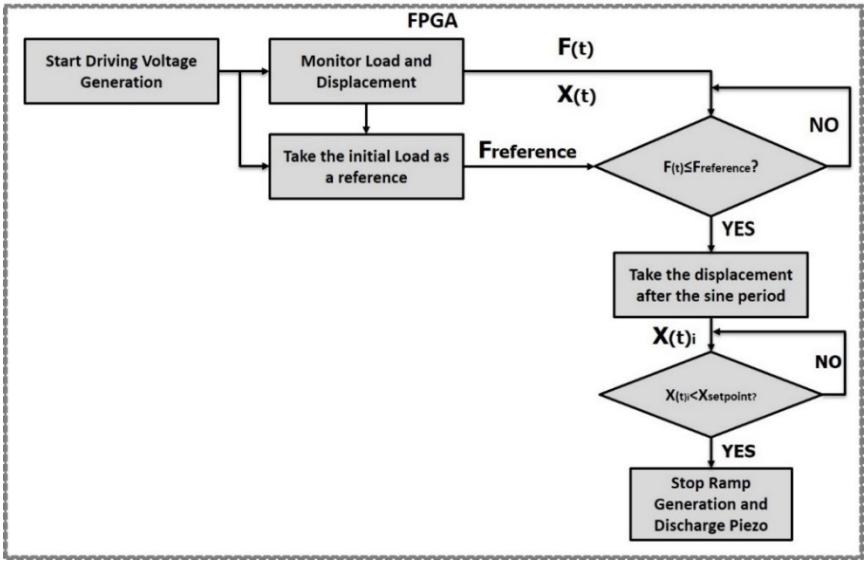


*Figure 4.12 - Final workflow of AMSD control loop*

A reference value of the relative position of the plug with respect to the sleeve is taken at beginning of the driving cycle. At the end of each sinusoidal cycle this reference is subtracted to the new measured position, in order to calculate the actual displacement. The displacement is then compared to the set-point, calculating the error; thus, the driving signal is stopped when the error has reached the value zero ("0").

## 4.3. Experimental Results

### 4.3.1. Test Procedure

The test plan was designed to have almost identical conditions for comparing the performance of both control strategies described above, in order to compare the final positioning error and evaluate the overall performance of the control loops. Both control models were tested using the same procedures for the approach, preload and discharge phases.

For this purpose, a design-of-experiment (DOE) approach was set-up, considering different driving signals parameters (slope, frequency) and different set-points as key paramters.

Eight different set-points were investigated with both driving strategies: 3, 6, 12, 16, 24, 30, 40, 50 µm.

For the Constant Slope driving, 6 different piezo drive slopes were used: 1, 1.25, 2.5, 5, 8, 10 V/s.

For the Amplitude Modulated Sinusoidal driving, two series of tests were executed:

- One driving voltage slope (2.5 V/s) with frequencies: 5, 10, 20, 30, 50 Hz.
- One driving voltage frequency (20 Hz) with different slopes: 1, 1.25, 2, 3, 5, 8 V/s.

For every test, the final positioning error was evaluated as the difference between the measured axial positioning at the end of the press-fit process ($X_{meas}$) and the set-point. The measured axial position was calculated as follow:

(25) $$X_{meas} = X_{final} - X_{initial}$$

### 4.3.2. Results

#### 4.3.2.1. Constant slope (CSD)

Fig. 4.13 shows the positioning error as a function of the set-points for different driving voltage slopes. A general trend that emerges from the results is observed by the fact that the positioning error decreases as the set-point increases. For a given set-point, the positioning error increases together with slope. The main explanation for these two trends is the delay for the calculation of the irreversible movement starting point which causes the controller to stop the driving piezo voltage late.

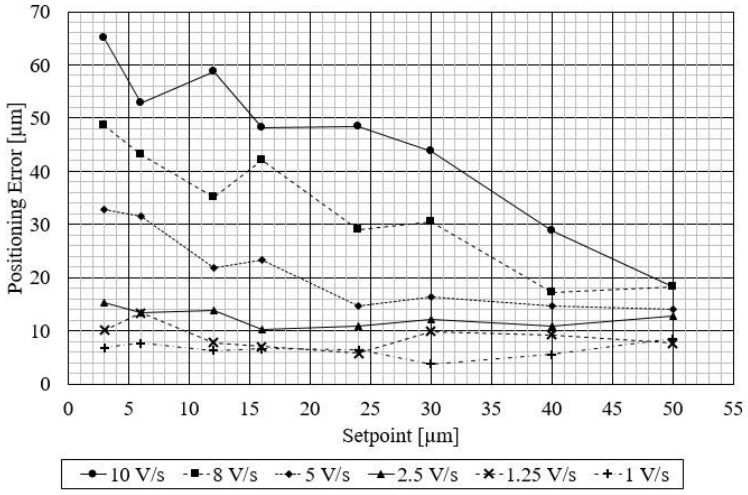


*Figure 4.13 - Positioning error for constant slope driving tests*

This delay can be divided into two contributes:

1. Collect the sampled data in order to fill the window necessary for the calculation of the inflection point
2. Transfer the data window from the FPGA to the Real-Time processor and execute the calculation (polynomial regression, derivative and calculation of its minimum), in order to find the inflection point.

The first contribution cannot be avoided while for the second one, the speed of task execution might have a relevant influence and generates a time delay in the following control action which will manifest itself in a delayed stop of the process, i.e. in a positive positioning error. In order to study this contribution to the delay, two different calculation rates of the processor were tested in addition, 100 ms and 5 ms; the second is the maximum rate performable by the Real-Time controller. For each rate, different slopes of the driving voltage were investigated, all of them for a set-point of 24 µm. Figure 4.14 presents that the real-time processor velocity has an influence only for largest slopes. For the lower slope test (1 V / s), the positioning error is very similar for the two processor speeds. This means that this error (~ 3.3 µm) is not depending on the performance of the controller but it is an intrinsic delay, due to the fact that the data needed for the calculation of the derivative must be collected in a buffer before derivation is executed. Depending on the acquisition rate, this delay can be reduced but not be eliminated, therefore this appears to be an intrinsic limit to the control process.

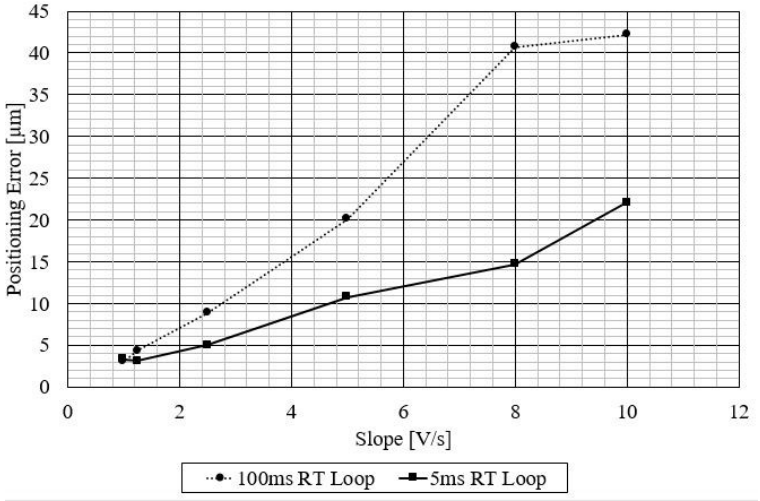


*Figure 4.14 - Comparison of two processor rates for a set-point of 24 µm*

4.3.2.2. Sinusoidal modulated (AMSD)

When testing different driving frequencies (Fig. 4.15), it appears that it is difficult for low frequencies (5 and 10 Hz) it is difficult to keep the relative motion of the plug during its stepwise motion under control. By increasing the driving frequencies (20, 30 and 50 Hz), the positioning error decreases continuously. However, if the setpoint is lower than 10 µm, a relatively poor accuracy on the positioning has been observed, even for large driving frequencies.

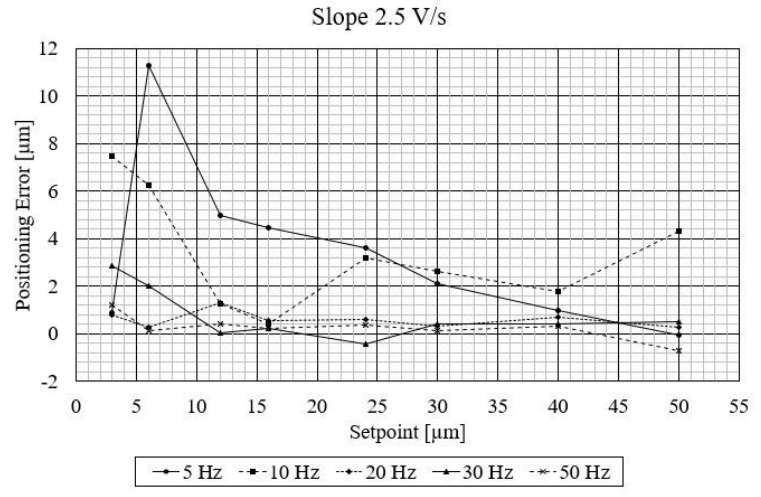


*Figure 4.15 - Positioning error for AMS driving tests for different slopes frequencies*

This is due to the first steps after the static-dynamic transition of the friction coefficient, which are much larger than the following ones, which occur with a constant dynamic friction coefficient (Fig. 4.16). It is worth to note that the minimum error for 50 Hz and 2.5 V/s slope is in range -1/+1.5 µm.

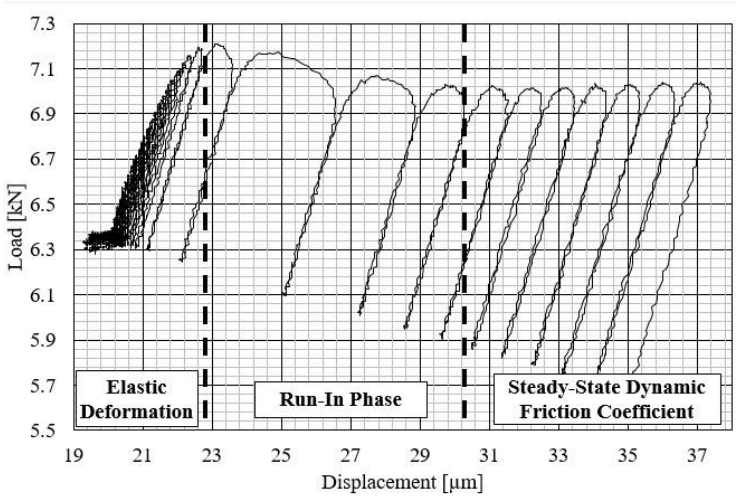


*Figure 4.16 - Load-displacement curve during the first steps of a AMSD test*

When the frequency is set to a higher value (50Hz) and different driving voltage slopes are investigated, see Fig. 4.16, positioning errors in the range +2/-1 µm are found for slopes lower than 5 V/s.

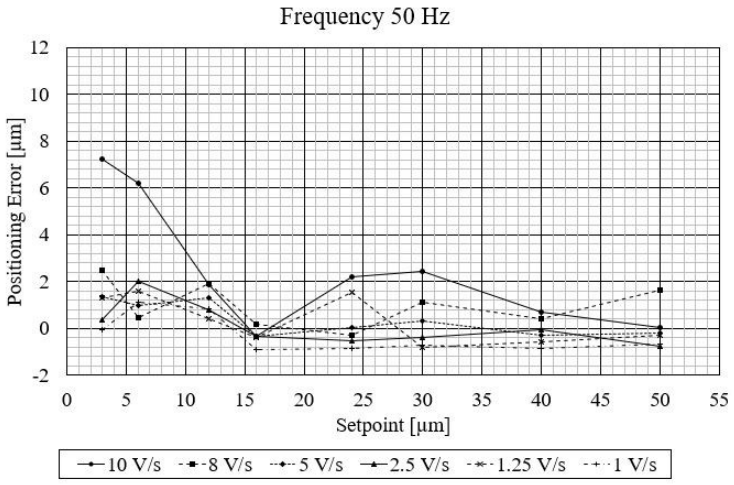


*Figure 4.17 - Positioning error for AMS driving tests for different frequencies*

4.3.2.3. Comparison of results

The CSD and AMSD control strategies are finally compared in Fig. 4.17. For the Constant Slope Driving voltage, the tests have been done with low driving voltage slopes (1 and 2.5 V/s) to avoid the influence of the control loop speed. Several repetitions have been

performed, using different samples. For the AMSD tests, a frequency of 50 Hz was used to better control the initial big steps during static-dynamic transition of the friction coefficient. With the two driving voltage slopes used, the final positioning error is lower for the AMSD algorithm than for the CSD algorithm. For example, in Fig. 4.17b, the minimum error with the Constant Slope Driving is of 3 µm while the maximum absolute error of AMSD is only 1.3 µm for the same setpoint (16 µm).

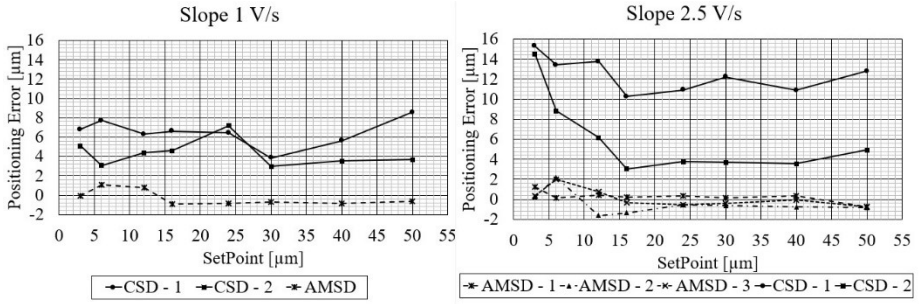


a) b)

*Figure 4.18 - Comparison of the positioning errors for a slope of (a) 1 V/s and (b) 2.5 V/s of the driving voltage*

The higher accuracy of the AMSD algorithm can be explained by analysing the envelope of the displacement maxima during an AMSD test (Fig. 4.18). The signal is similar to the displacement signal during a CSD test. It is not possible to discriminate the elastic deformation from the pre-sliding when using a CSD control strategy. Instead, with an AMSD control, the piezoelectric actuator removes the load to the part being pressed at the end of each period. Thus, AMSD control strategy allows a direct estimation of pre-sliding motions which cannot be evaluated when a CSD control is used.

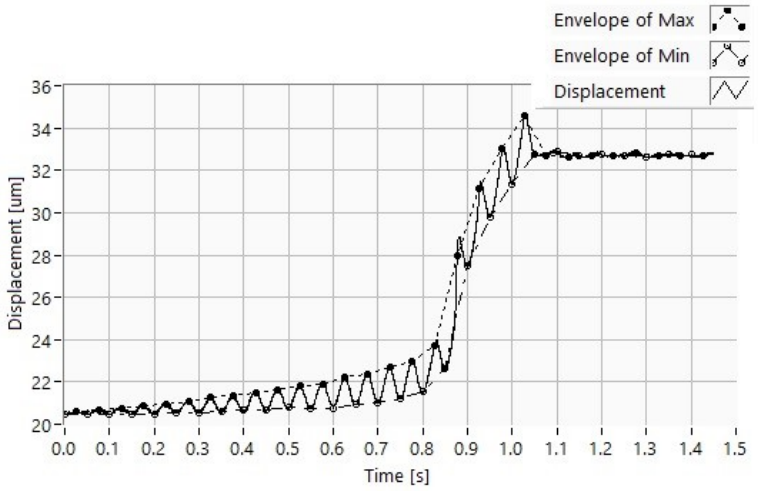


*Figure 4.19 - Envelopes of the maxima and minima of the displacement for a test with the AMSD control*

With the presented press-fit station prototype a large operation range is possible as the result of the combined action of the hydraulic cylinder, which ensures a long stroke, and a fine positioning resolution, provided by the piezoelectric actuator. The layout also allows a complete automation of the process in terms preload and assembly capability.

Major focus has been put on two different driving of signals for the piezoelectric actuator, which allow to apply respectively a continuous load and a discontinuous load. They have been compared using the final deviation between the set-point and the actual position of the plug into the sleeve as a key performance indicator.

The comparison of the results offers a smaller positioning error with the AMSD control strategy. This is mostly due to the fact that with the AMSD control strategy it is possible to detect and to take into account the pre-sliding effect. This phenomenon is indiscernible with the control loop based on the AMSD signal, for set-point values ranging from 3 to 50 µm.

# 5. Application Case 1: Dry Calibration of GDI Injector

A series production GDI injector is depicted in Fig. 5.1 [82]. The filter is assembled to the injector body by interference fit. Even between the adjustment sleeve (AS) and the internal pole the interference fit occurs; thus, changing the AS position the injector behaves differently due to a different spring preload. The spring acts on the armature that lifts the needle once the solenoid coils are excited by current, by means of a stop rig.

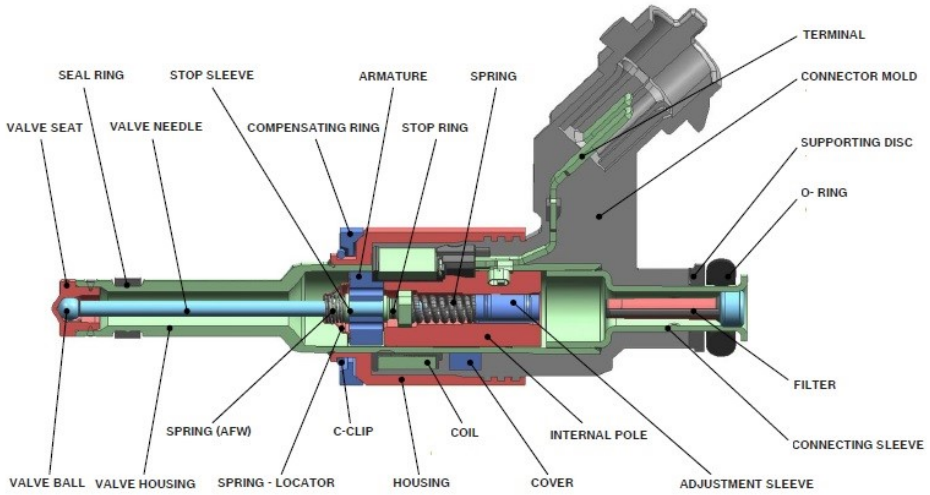


*Figure 5.1 - Main components of a GDI injector*

The process for calibration of such type of GDI injectors is currently based on the assembly of the AS that modifies the preload of the spring; the correct final position permits to assure the target injected quantity.

The operation fluid used is a liquid, for instance Exxol or N-heptane as replacement of gasoline; these of fluids have similar fluid-dynamic characteristic than gasoline with more repeatability of performances and pose less safety issues. However, even these fluids are inflammable, toxic and need safety requirements for the use and the management that increase costs.

Safety issues would be completely removed if a safe fluid could be used for injector calibration. The use of a gas such as nitrogen appears promising, also because it would avoid

the need to clean the injectors after the test, prior to packaging, because the process would become completely dry.

The so-called Dry Calibration process aims to use Nitrogen as a working fluid for the calibration process of GDI injector in the ballistic region. The choice of the ballistic region is due to the fact that the calibrating along the linear region does not assure small errors in the low fuel delivered region. This means that the real behaviour of the injector can be highly different from the nominal one in that portion of characteristic curve. With the new emissions regulations, the small quantities have increased their importance and this error cannot be accepted anymore; the injectors need to be calibrated for having lower errors at small quantities in order to be more predictable in terms of behaviour (Fig. 5.2).

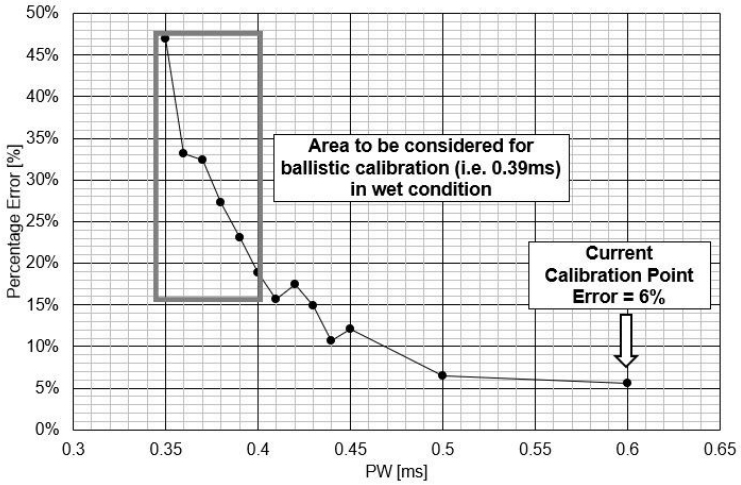


*Figure 5.2 - Error respect to the target quantity of a batch of GDI injectors calibrated in the linear region (ET <0.6 ms)*

The ballistic region is characterized by non-linearities and large sensitivity to the AS position that require high accuracy in the positioning; this is an advantage in the calibration process, because it will provide more sensitivity to positioning errors, therefore enabling for a better repeatability of the calibration process. As shown in Fig. 5.3, even a difference of 13 μm in the filter position produces a measurable difference in the characteristic curve of the injector, i.e. in the injected fuel quantity.

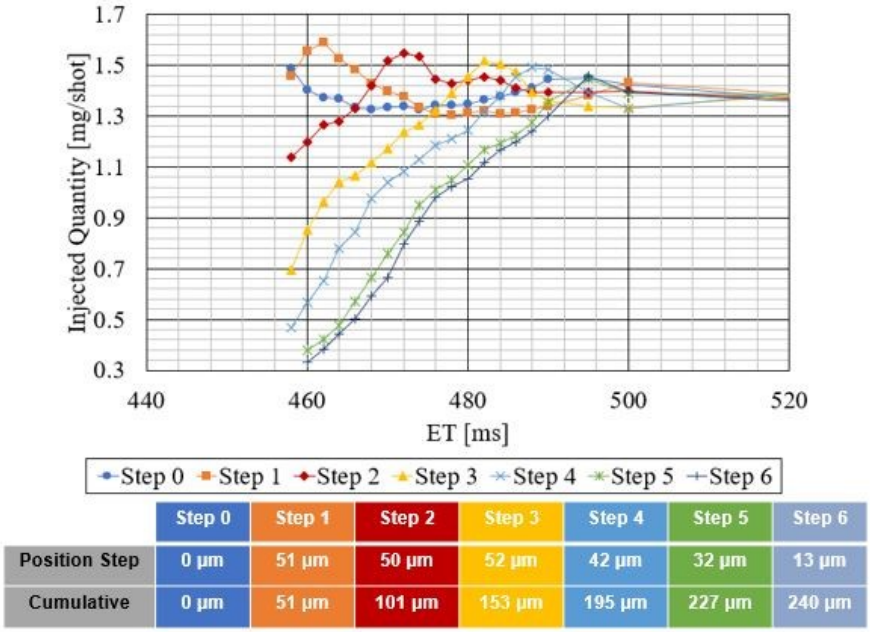


| | Step 0 | Step 1 | Step 2 | Step 3 | Step 4 | Step 5 | Step 6 |
|---|---|---|---|---|---|---|---|
| Position Step | 0 µm | 51 µm | 50 µm | 52 µm | 42 µm | 32 µm | 13 µm |
| Cumulative | 0 µm | 51 µm | 101 µm | 153 µm | 195 µm | 227 µm | 240 µm |

*Figure 5.3 - Characteristic curves of a GDI injector for different filter position*

The use of a different fluid for calibration poses a question of correlation between gas (dry calibration) injected quantity and liquid (wet calibration) injected quantity. The correlation between the performance of the injector operated with different fluids can be based on experiments. Therefore, the goal of the developed process is to calibrate a batch of injectors in dry conditions (Nitrogen), in the ballistic region, and check that the re-test in liquid (N-Heptane) stays within an error range less than ±15%.

The activities were divided as follow:

- **Flow Correlation** → A batch of 10 injectors "wet calibrated" was used to find the Nitrogen vs. N-heptane correlation and the best dry conditions
- **Dry Calibration** → A batch of 9 injectors were dry calibrated with Nitrogen
- **Final Measurement** → N-Heptane measurement were done on dry calibrated injectors, checking batch dispersion in the ballistic region (target <±15%)

In the next section the measurement setup for the injector characterization in Nitrogen will be highlighted; afterwards a correlation between liquid and gas in different functional regions will be presented. After the definition of the target quantity, the process will be detailed and the final results discussed.

## 5.1. Measurement System for Injected Fuel Quantity

The previous chapters have displayed how the tighter emissions regulations have led to the development of more efficient injection systems for an improvement in the combustion of ICE. The ECU needs to determine the correct injection parameters, based on both the functional conditions and the requested performances. However, for this operation, the ECU needs to know how much fuel is injected for a certain ET and, using an open loop configuration, an accurate characteristic curve of the injector has to be implemented. This curve represents the ideal performance of the injector: a real component will behave differently. This requires the measurement of the real performance of every injector, taking into account the measured offset in the ECU. Thus, at the end of line testing of the injector manufacturing process, a measurement of the injected quantity is needed.

This can be done by calculating the average quantity of a fixed number of shots; however, after performing multiple injections and averaging the results, information related to the injection of a single shot will be lost. In order to overtake this problem, the injection rate (Fig. 5.4) needs to be known; this permit to calculate the injected quantity for every opening period of the injector. An instrument with this characteristic is called “Shot-To-Shot” device (STS).

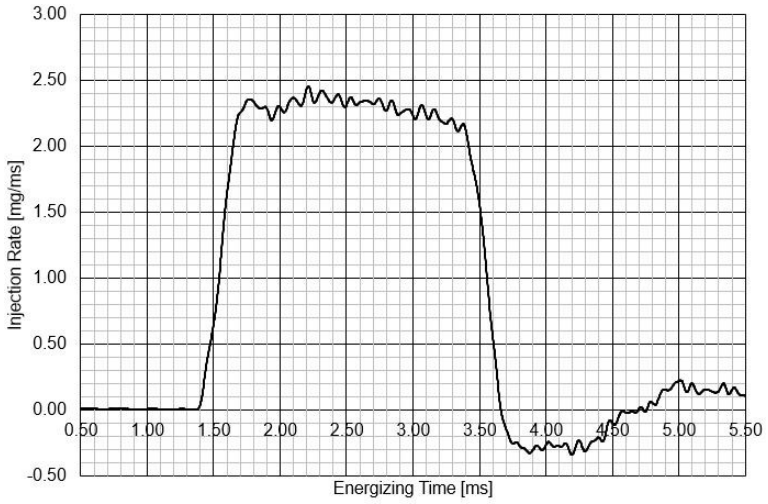


*Figure 5.4 - Injection rate of a GDI injector*

The STS device is not the only component of the measurement chain: the injector needs to be driven in terms of excitation current and needs to be fed with a testing fluid at the correct pressure. Fig. 5.5 shows the schematic of the setup used for the injector characterization.

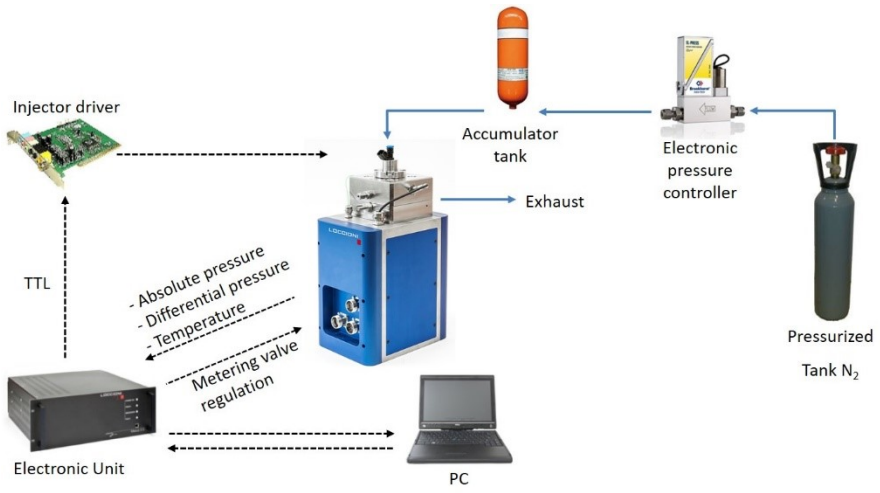


*Figure 5.5 - Schematic of the measurement setup for GDI injector characterization*

In the following section the features of the two core elements used in the application case will be explained in detail:

- the STS device
- the injector driver.

### 5.1.1. Shot-to-Shot device for fuel injector fed with a gas

Loccioni's AirMexus (Fig. 5.6) is an integrated and multifunctional injection measurement instrument [83 – 84] that can measure both the fuel injection quantity and the injection rate for every single shot.


*Figure 5.6 - Loccioni AirMexus*

The injection mass rate is indirectly calculated by means of the measurement of temperature and pressure inside the test chamber.

The test chamber is modelled as a zero-dimensional control volume equipped with an inlet and an outlet (Fig. 5.7). With this approximation all the variables inside the volume are intended constantly distributed within the volume and dependent only on the time.

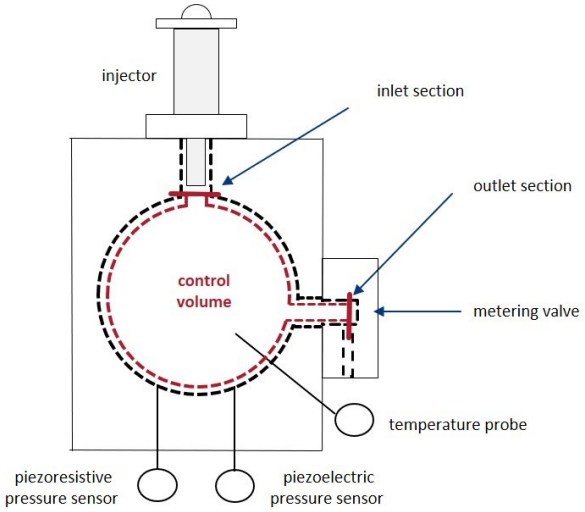


*Figure 5.7 – Schematic of AirMexus measuring chamber*

Thus, it is necessary to determine the analytic expression of the mass rate as a function of the temperature and the pressure inside the chamber. The mass inside a constant volume chamber can be expressed as follows:

(26) $M = \rho V$

Considering the continuity equation of a volume with an inlet and an outlet:

(27) $\dot{m}_{in} = \frac{dM}{dt} + \dot{m}_{out}$

where $\dot{m}_{in}$ is the injected quantity rate, $\dot{m}_{out}$ is the mass that flows outside the control volume and $\frac{dM}{dt}$ is the mass variation inside the volume. Considering the gas behaviour, as approximated by a perfect gas by (28), the variation of mass can be expressed as shown in equation (29):

(28) $\rho = \frac{p}{RT}$

(29) $\frac{dM}{dt} = V \frac{d}{dt}\left(\frac{p}{RT}\right)$

The mass flow of the outlet port can be expressed as follow:

(30) $\dot{m}_{out} = \rho u \sigma_s$

where $\rho$ is the density, $u$ the gas velocity and $\sigma_s$ is the effective orifice area also called vena contracta area. Considering a compressible flow, stationary, mono-dimensional, isentropic and sonic, the equivalent mass rate can be expressed as follow:

(31) $\dot{m}_{out} = \sigma_S \frac{p_0}{\sqrt{RT_0}} \sqrt{k \left(\frac{2}{k+1}\right)^{\frac{k+1}{k-1}}}$

where $R$ is the specific gas constant, $k$ is the isentropic dilatation coefficient $\left(k = \frac{C_p}{C_v}\right)$, $p_0$ and $T_o$ the total pressure and temperature inside the chamber respectively.

Using (29) and (31) in the (27) the injected quantity can be expressed as:

(32) $\dot{m}_{in} = \frac{V}{R} \frac{d}{dt}\left(\frac{p}{T}\right) + \sigma_S \frac{p_0}{\sqrt{RT_0}} \sqrt{k \left(\frac{2}{k+1}\right)^{\frac{k+1}{k-1}}}$

Using the adiabatic condition for the pressure derivative (see Appendix), the (32) is expressed as follow:

$$\dot{m}_{in} = \frac{V}{kTR}\frac{dp}{dt} + \sigma_S \frac{p_0}{\sqrt{RT_0}}\sqrt{k\left(\frac{2}{k+1}\right)^{\frac{k+1}{k-1}}} \quad (33)$$

The hypothesis of a zero-dimensional system means in detail, that the velocity field is always zero; thus, the total pressure and temperature are the same of the static ones. The equation (33) can be expressed in the following manner:

$$\dot{m}_{in} = \frac{V}{kTR}\frac{dp}{dt} + \sigma_S \frac{p}{\sqrt{RT}}\sqrt{k\left(\frac{2}{k+1}\right)^{\frac{k+1}{k-1}}} \quad (34)$$

By introducing two constant, $C_1$ and $C_2$, defined as:

$$C_1 = \frac{V}{kTR} \quad (35)$$

$$C_2 = \frac{\sigma_S}{\sqrt{RT}}\sqrt{k\left(\frac{2}{k+1}\right)^{\frac{k+1}{k-1}}} \quad (36)$$

The equation (34) becomes the following:

$$\dot{m}_{in} = C_1\frac{dp(t)}{dt} + C_2 p(t) \quad (37)$$

The analytical expression (37) is used to calculate the injected mass flow rate. For this purpose, the calculation of $C_1$ and $C_2$ factors is necessary.

The $C_1$ factor is computed through (35) knowing the chamber volume and the gas properties and measuring the temperature in the test chamber.

Factor $C_2$ cannot be obtained directly from (36) because the vena contracta area $\sigma_s$ can be found only empirically. Therefore, equation (36) when $\dot{m}_{in} = 0$; in other words, when the injector is not injecting.

$$0 = C_1\frac{dp(t)}{dt} + C_2 p(t) \quad \Longrightarrow \quad C_2 = -C_1\frac{1}{p(t)}\frac{dp(t)}{dt} \quad (38)$$

The inlet flow is zero when the injector is in the closing configuration (Fig. 5.8); theoretically it is sufficient to determine *p(t)*, its time derivative and the value of $C_1$ at any time in which the injector is in the closing configuration.

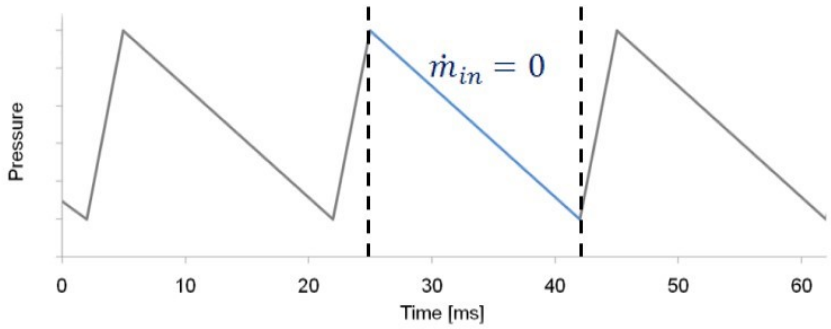


*Figure 5.8 - Closing condition used for calculation of $C_2$*

The pressure values in the measurement chamber *p(t)* and the values obtained by its derivative $\frac{dp(t)}{dt}$ allow, by the procedure described, to calculate the mass flow rate.

### 5.1.2. Injector Driver

The injector drive pulse was generated by the Loccioni universal injector driver: labelled as "Jupiter". This injector driver system is an electric generator of various current profiles, able to cover a wide range of needs for stimulation of injectors and valves in automotive application. The user interface permits to program the profile, editing the main features in terms of time, current and voltage, as shown in Fig. 5.9.

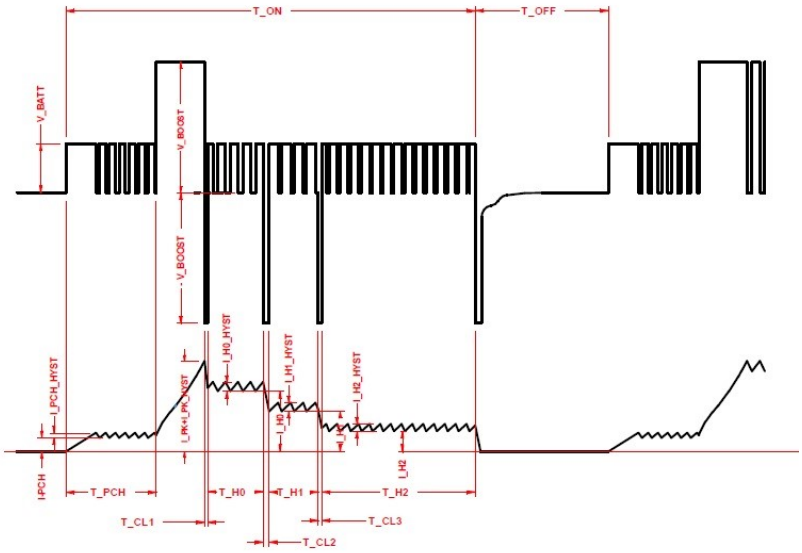


*Figure 5.9 - Current and voltage profile shape*

## 5.2. Correlation between Wet and Dry Measurement

For the development of the dry calibration process, it is necessary to identify the correlation between gas injected quantities and liquid injected quantities. The two selected working fluids are N-heptane (liquid) and Nitrogen (gas). Different aspects have been investigated to understand the sensitivity of the dry measurements to changes in characteristic variables. First, the characteristic curves have been correlated to demonstrate the feasibility of using gas instead of liquid for the injector characterization. Then the influence of the spring load has been studied. This is done by means of the adjustment sleeve press-fit, reaching a final position that impresses a preload to the spring connected to the AS. Finally, the correct parameters for improving the correlation in the ballistic region have been analysed, finding the appropriate current profile and injector feeding pressure.

This study is fundamental, in order to safeguard the correlation between dry and wet measurements; in this way the N-heptane target quantity for the calibration can be transferred in the corresponding the Nitrogen target, ensuring only a marginal error. In Fig. 5.10 characteristic flow curves of a GDI injector fed with both N-heptane and Nitrogen are presented. Along each of these curves three different regions can be detected:

- Linear region [0.7 – 3 ms]
- Rebounds region [0.35 – 0.7 ms]
- Ballistic region [0.28 – 0.35 ms]

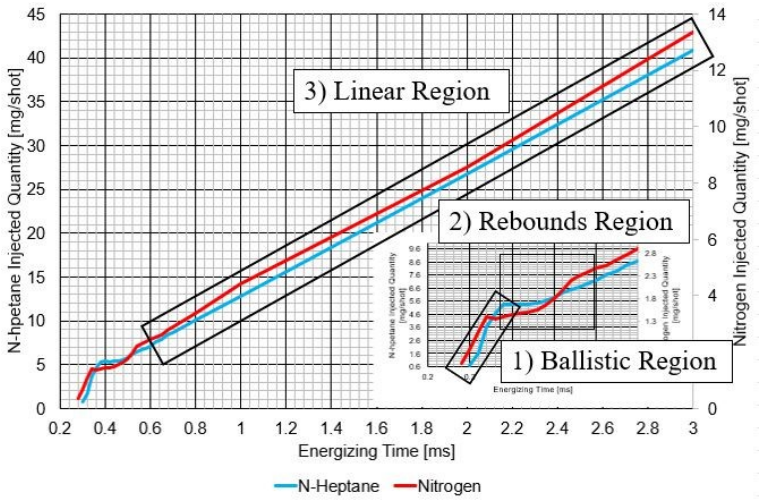


*Figure 5.10 - Characteristic flow curve of GDI injector measured with N-heptane and Nitrogen*

At low ETs, the so-called ballistic region is dominated by non-linearities. This region is also characterized by the fact that during the opening of the injector the anchor and consequently the needle of the injector do not travel for the entire stroke till the pole piece.

Then the maximum stroke of the needle is reached, that touches the pole piece and several bounces occurs. This determines a different opening positions of the injector and an associated fluctuation of the injected quantity. Thus, even in this region are non-linearities given, but the static condition, when the needle is in the maximum strike position is increasing its predominance within the driving pulse period (i.e. the ET).

For larger ET the injector is in the maximum opening position for the most part of the pulse width; the non-linearities can be neglected and the injected fuel quantity can be approximated as a linear function of the energizing time.

The regression of the injected quantities in N-heptane and Nitrogen shows a strong correlation for both linear and rebounds region (Fig. 5.12).

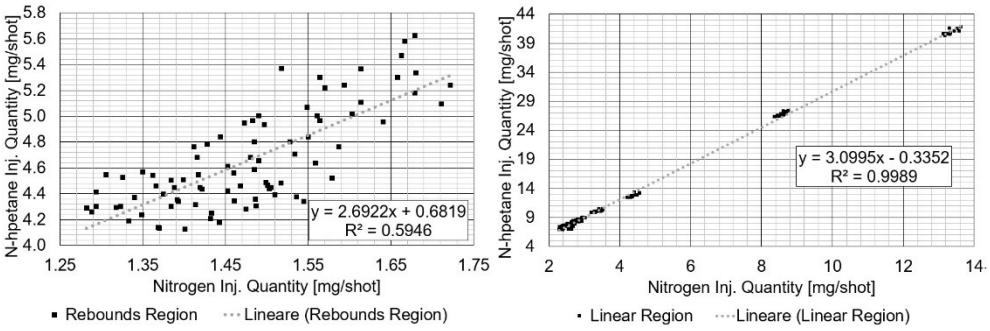


a) b)

*Figure 5.11 - Linear correlation between N-heptane and Nitrogen in a) rebound and b) linear region*

These results open the possibility to find a good correlation even in the ballistic region, which represent the region of interest for the dry calibration process.

Thus, a dedicated test campaign was performed in ballistic conditions. A batch of 10 injectors was analysed; these injectors have been calibrated with the standard wet process.

For this batch the following procedure has been followed:

- Measure the N-heptane injected quantity using a STS device
- Measure the Nitrogen injected quantity using a Loccioni AirMexus
- Identifying a common ballistic region for all the injectors
- Selection of the ET to have the same number of test points both for n-heptane and nitrogen

The injected quantities are plotted for all the pulse widths and all the injectors within the common ballistic region, in Fig. 5.12. A linear regression was then performed in order to estimate the coefficients to predict the N-heptane injected quantity from a Nitrogen injected quantity. The prediction error was calculated for all the injectors, reporting the Mean Absolute Error (MAE). The correlation analysis was made for all the test conditions. The Pearson correlation coefficient $\rho_{xy}$ (sometimes referred as Pearson's r) was used, defined as follow:

$$\rho_{xy} = \frac{\sum_{i=1}^{n}(x_i-\bar{x})(y_i-\bar{y})}{\sqrt{\sum_{i=1}^{n}(x_i-\bar{x})^2(y_i-\bar{y})^2}} \quad (39)$$

where:

- $n$ is the sample size
- $x_i$, $y_i$ are the single samples indexed with i
- $\bar{x} = \frac{1}{n}\sum_{i=1}^{n} x_i$ (the sample mean); and analogously for $y_i$

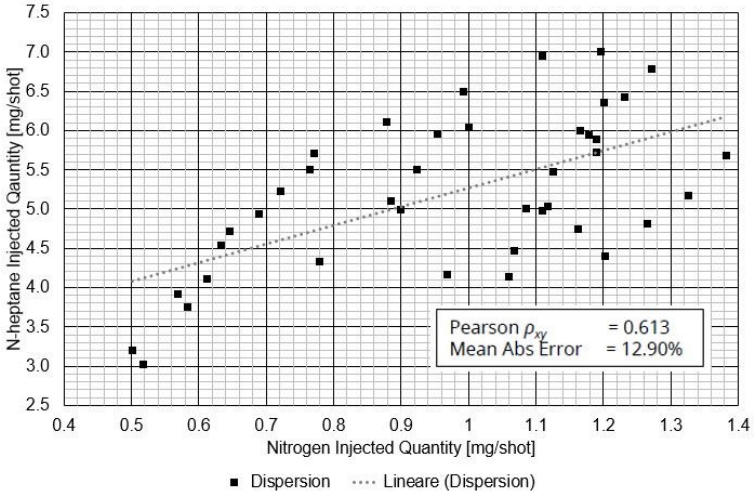


*Figure 5.12 - Dispersion of the injected quantities in Nitrogen and N-heptane*

For each pulse width, the Pearson correlation coefficient was calculated, in order to identify the ET that maximizes the correlation.

*Table 5.1 - Comparison of pulse widths for maximization of Pearson coefficient*

| ET $N_2$ | ET N-heptane | Pearson $\rho_{xy}$ | Mean Absolute Error |
|---|---|---|---|
| [ms] | [ms] | | % |
| 0.472 | 0.38 | 0.76 | 8% |
| 0.474 | 0.39 | 0.7 | 8% |
| 0.476 | 0.4 | 0.56 | 8% |
| 0.478 | 0.41 | 0.46 | 7% |

By averaging the injected quantities of the reference batch, the target quantity for the calibration process was derived (Fig 5.13).

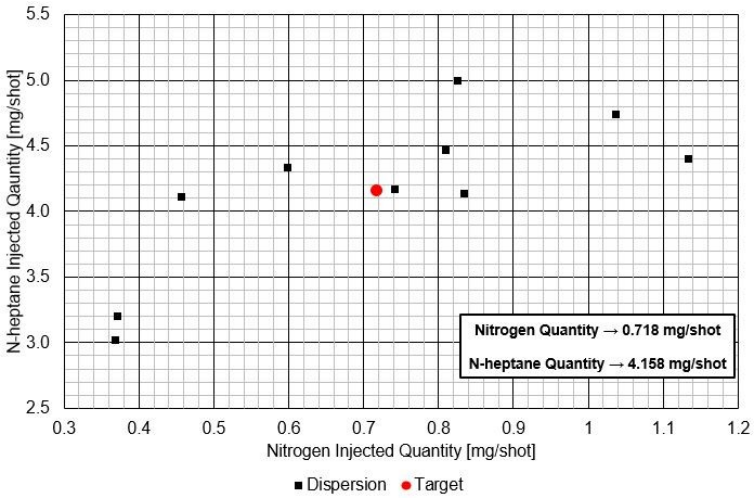


*Figure 5.13 - Target calculation for dry calibration*

In this phase the feasibility of the correlation between dry and wet measurements of the injected quantity for GDI injector has been investigated. The result is in the target quantity in Nitrogen that is the setpoint of the dry calibration process. Using the correlation, a small error using a gas instead of liquid was introduced, in this case 8% of MAE.

## 5.3. Dry Calibration Process

In this section the new proposed process will be highlighted and the results will be discussed, in order to demonstrate the reduction of the error that can be achieved by calibrating a batch of injectors in the ballistic region using Nitrogen as operating fluid.

The high sensitivity of the injected quantity to the position of the AS in the ballistic region requires to use a really accurate press system to fulfil this specific requirement. Furthermore, the injected quantities are comparably small and a high-resolution device for flow rate measurement is ultimately needed. The process goes round these two core elements (Fig. 5.14), performing the assembly of the part and then measuring the functional performances.

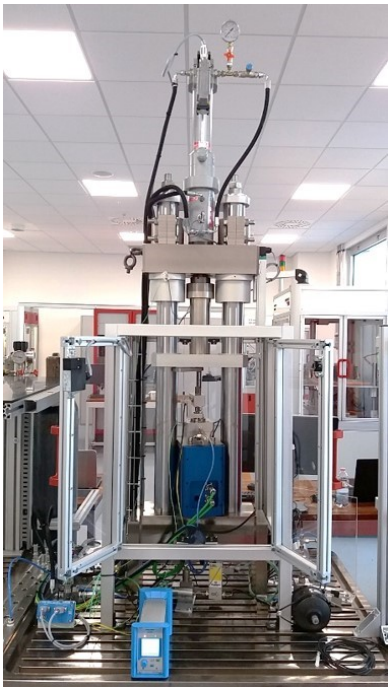

*Figure 5.14 - Configuration of the dry calibration test bench*

### 5.3.1. Developed process

The process is characterized by an iterative process, based on two control loops (Fig. 5.15), one for the positioning of the fuel filter and one for the injected quantity. In practice the press-fit of the fuel filter is done in one iteration, reaching the position setpoint; after this step, the current injected quantity is measured, in order to compare the measured value with the target quantity. The iteration continues till the injected quantity matches the target value.

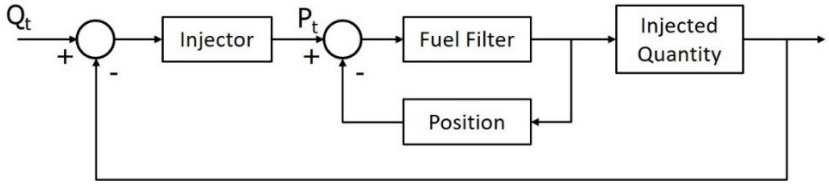


*Figure 5.15 - Schematic of the double control loop*

With the target value found in the correlation phase, nine uncalibrated GDI injectors underwent the proposed process. Then, the injectors have been tested in N-heptane for the wet characterization, in order to check the fulfilment of the target in liquid.

The estimation of the needed position delta to reach the quantity target has been implemented as a linear regression of the injected quantity with respect to the AS position, calculated as the cumulative of the setpoints given to the press. Thus, the idea is to start with large setpoints and reduce the step size after each iteration. Fig. 5.16 reports the error in the assembly of the real final position with respect to the setpoint.

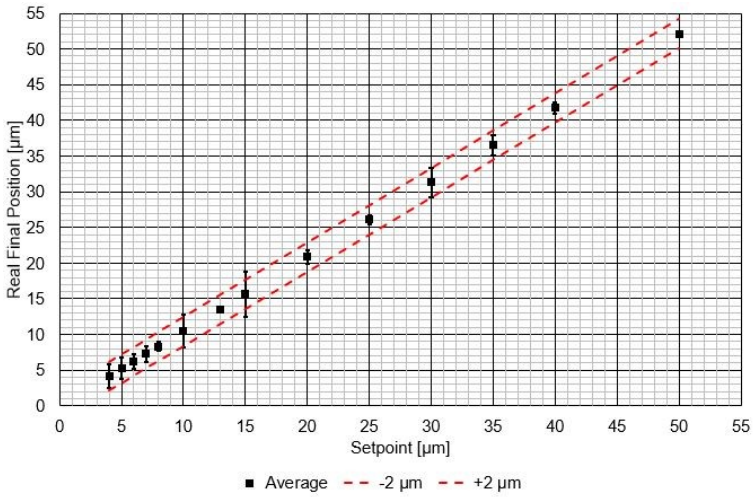


*Figure 5.16 - Accuracy of the press-fit*

The AMSD control is able to achieve the shown performances using samples, even for real components. In the next section the obtained results regarding the injected quantity will be exposed in more detail.

### 5.3.2. Results

Fig. 5.17 provides the comparison of the dispersion and the MAE for two different injector batches:

- 10 injectors, calibrated at 0.6 ms (linear region) with the standard wet process
- 9 injectors calibrated at 0.472 ms (ballistic region) with the new dry process

These injected quantities have been measured in N-heptane to have a retest of the injectors in liquid conditions that represent the real operational conditions.

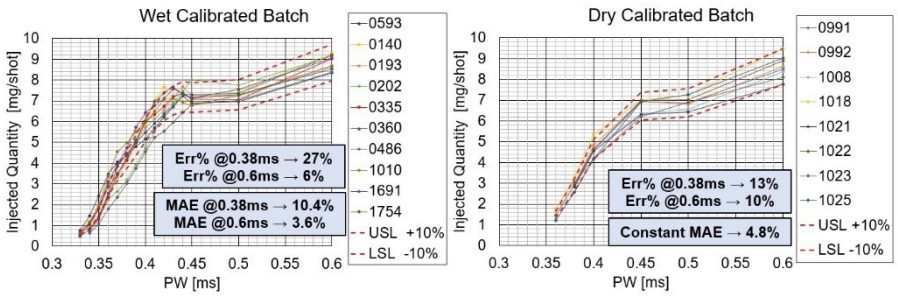


*Figure 5.17 - Comparison of error dispersion and MAE of wet calibrated and dry calibrated batch*

The dry calibration has reduced the error in the ballistic region by a half, with a little increment of the error at 0.6 ms, but within a target range of ±10%. The calculation of MAE shows that the curves have been aligned, with respect to the average along the characteristic curve.

Even the evaluation of the error with respect to the quantity target presents a small deviation (Fig. 5.18).

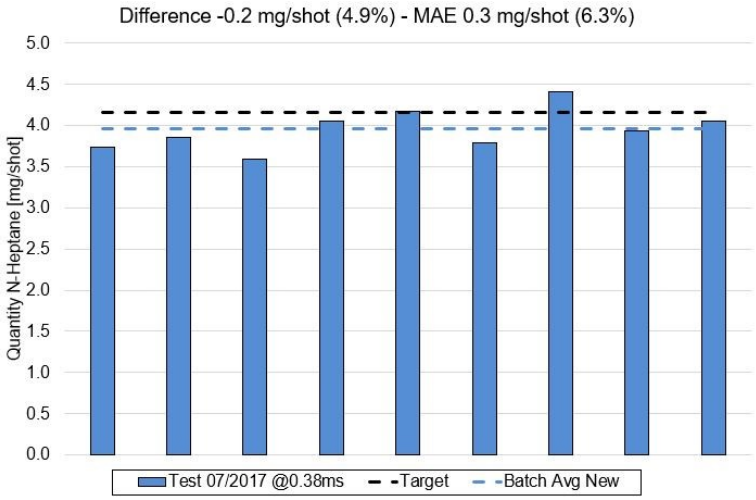


*Figure 5.18 - Error of the dry calibrated batch with respect of the quantity target in liquid*

These results demonstrate that a complete dry calibration module is feasible for industrial purposes and with the adoption of the press-fit prototype station a high accuracy in the fuel filter assembly is reachable. Furthermore, the performances observed during the validation of the press prototype have been respected even for real hardware components.

The usage of a dry calibration process represents a step towards a more efficient technique, leading also advantages in terms of:

- Cost reduction mostly due to the unnecessity of the purge module and the pressure generation system
- Cost saving for liquid storage & management
- Energy cost reduction
- Safety & health for operators cost reduction

# 6. Application Case 2: Assembly of Needle Control Valve of CR Diesel Injector

The injector in a common rail system normally consists of the nozzle module, a piezoelectric crystal for piezo injectors or a solenoid valve for electro-mechanical injectors, as well as hydraulic and electrical connections for actuation of the nozzle needle.

In a common rail injection system, the high-pressure pump pressurizes the fuel in the rail. The fuel flows to the injector in two different areas, one on the top and one on the bottom of the nozzle needle. The two resulting forces are equal, cancelling each other; forcing the needle to remain in a neutral position by means of a dedicated spring and by hydraulic forces.

The upper area has an outlet duct driven by a command valve, actuated either by a solenoid or by a piezoelectric. For a solenoid control valve, when the excitation current is engaged, the electromagnetic effect opens the valve that releases the pressure to the return passage. The pressure on the bottom area of the injector lifts the needle and the injection starts.

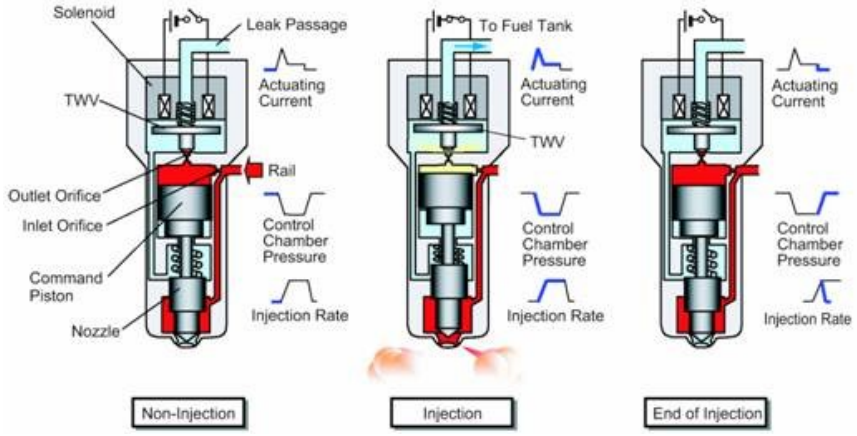


*Figure 6.1 - Operating principle of a solenoid common rail injector*

Closing the control valve, the upper area of the injector is pressurized again, the needle goes down and the injection stops injecting fuel.

Therefore, the control valve is one the main components of common rail injectors; a correct design is mandatory for a precise control of the injected quantity and a reduction of the opening and closing delays.

## 6.1. Focus on the industrial problem

There are several types of control valves, depending on the injector layout and concept: for this application case the component is schematically structured as shown in Fig. 6.2, with the following parts:

1. Valve body
2. Armature
3. Pin

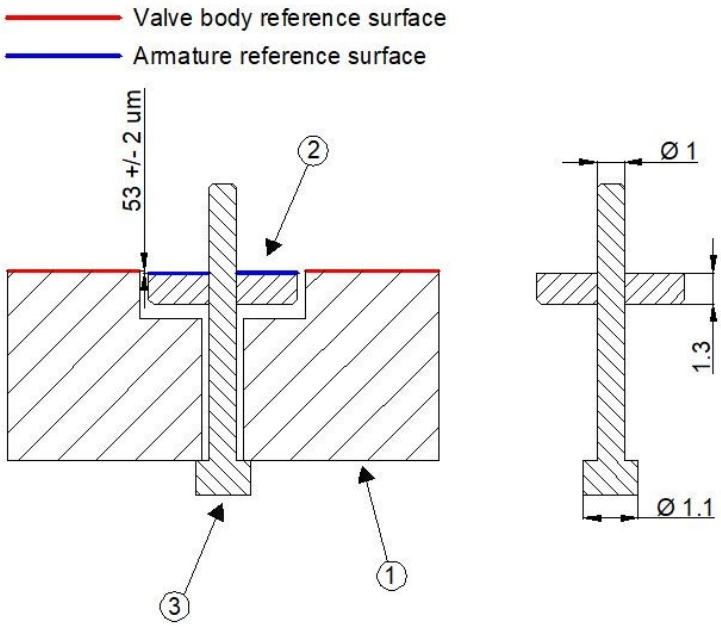


*Figure 6.2 - Schematic of the control valve*

The pin is guided through the valve body and press-fitted to the armature, where the interference takes place. Then, the pin head touches the body reaching the final assembly position. The valve body diameter is bigger than the pin; thus, a clearance occurs.

The target position is taken as a differential height between two reference surfaces, one on the valve body (red line in Fig. 6.2) and one on the armature (blue line). The final position, also called Final Air Gap (FAG) has to be 53 µm, with a tolerance of ± 2 µm.

In order to fulfil this requirement, both an accurate press process and precise measurements system are mandatory. In the next section the proposed solution will be highlighted.

## 6.2. Proposed workflow of the process

Due to the complexity of the problem, the layout of the process has been divided in two different stations, which work in a sequential and iterative way (Fig. 6.3):

- Measurement station
- Press station

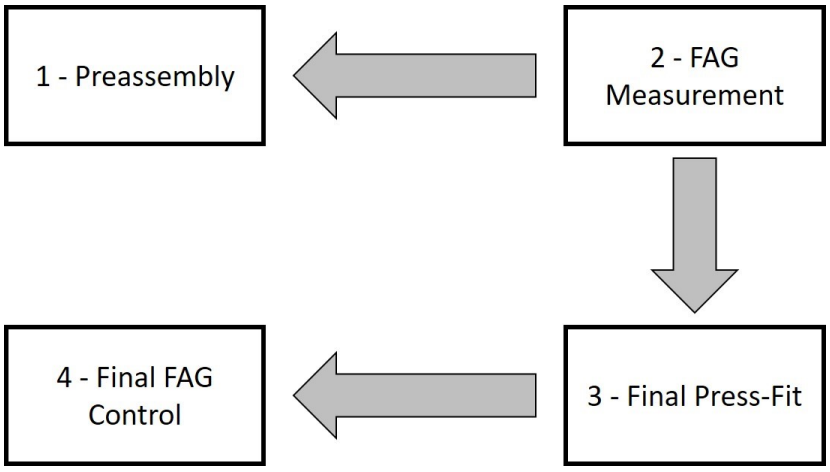


*Figure 6.3 - Workflow of the proposed assembly process*

The cycle starts with the preassembly phase, necessary to have the first insertion of the pin with respect to the armature; in this step it is not necessary a micrometric accuracy. After that the differential position of the armature with respect to the valve body is measured, in order to get the final setpoint for the accurate press-fit, where the full scale prototype's performances are used. The part is tested again in the measurement station to verify if the FAG is within expected tolerance or not.

## 6.3. Development of the stations

The layout of the full scale prototype press combining a hydraulic cylinder and a piezoelectric actuator is the same as described in Chap. 4. A dedicated tooling system for the control valve assembly has been designed. The measurement station able of scanning the entire surface of the control valve was also designed. Fig. 6.4 depicts the measurement station, composed by two piezoelectric linear stages and a single point triangulation sensor: sample can be moved over a horizontal plane by means of the linear stages, scanning the surface of the part.

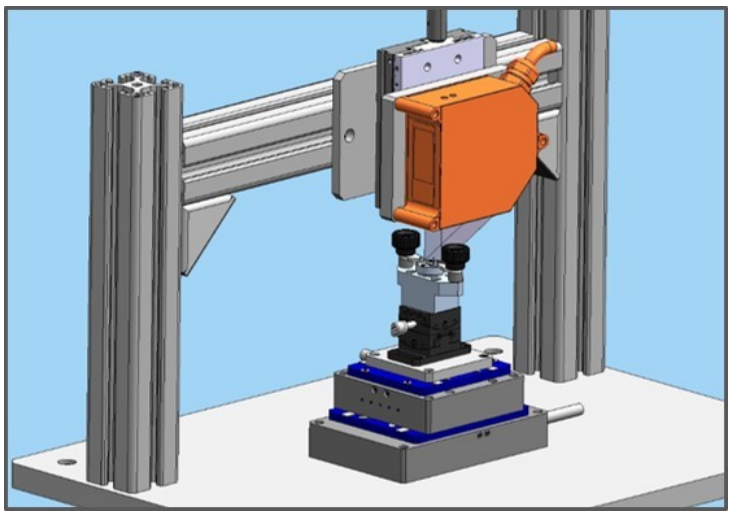

*Figure 6.4 - Layout of the measurement station*

The single point triangulation sensor has both a linearity and a resolution lower than 1 µm while the linear stages are highly performing in terms of flatness (< 1 µm) as shown in the following table.

*Table 6.1 - Characteristics of the equipment of the measurements station*

| **Equipment** | **Range** | **Linearity** | **Resolution** | **Flatness** |
|---|---|---|---|---|
| Single Point Triangulation | 2 mm | 0.6 µm | 0.03 µm | - |
| Linear Stage 1 | 10 mm | - | - | 0.5 µm |
| Linear Stage 2 | 20 mm | - | - | 0.5 µm |

### 6.3.1. Measurement of the armature position

The scanning path of the valve is shown in Fig. 6.5. The red rectangle is the available scanning area with the linear stages; in this area two straight lines has been chosen as scanning path, 45° degrees tilted with respect to the reference system.

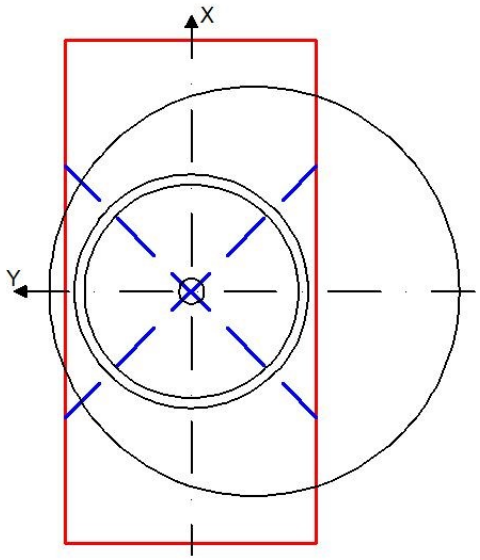


*Figure 6.5 - Scanning path of the valve*

Along these two traces the position has been acquired continuously, triggering the start and the end of each scanning stroke by using a TTL signal. This signal, sent by the linear stage, identifies when the stage is in motion. The TTL was acquired by the electronic module of the triangulation sensor and it was used to synchronize the measurements.

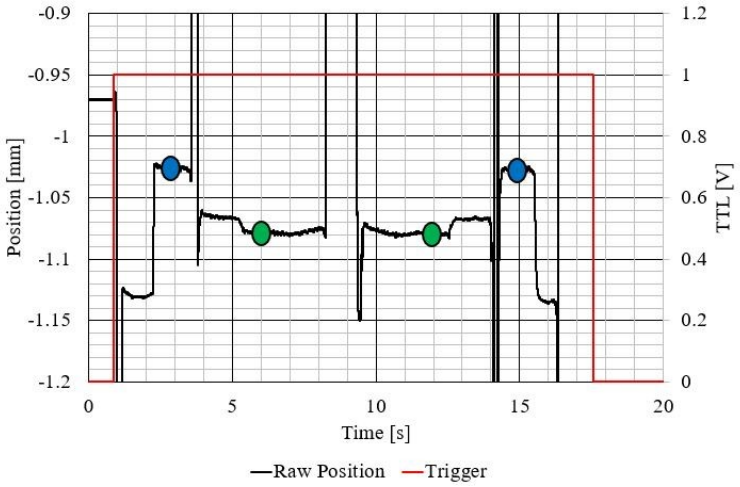


*Figure 6.6 - Synchronization of the position measurement with the scanning stroke*

For each trace 4 windows have been defined (Fig. 6.6), in order to extract the data:

- 2 for the body reference surface (blue circles)
- 2 for the armature (green circles)

The extracted data have been used for a linear fit of the reference surface and the armature respectively. With these linear regressions the FAG was calculated as the difference between the two straight lines in the centre point of the valve. For the centre point the half of the pin was chosen.

### 6.3.2. Repeatability and reproducibility of the measurement station

A repeatability and reproducibility test has been done, in order to evaluate the performances of the measurement station. Two different conditions have been tested:

a) 10 consecutive measurements of a single valve without removing the part from the measurement station

b) 10 consecutive measurements of a single valve, removing and putting again the valve into the measurement station

c) 10 consecutive measurements rotating the pin respect the valve body 90° every test

For each test, the repeatability was calculated as follow:

$$R_x = \frac{3\sigma}{T_{max} - T_{min}} \quad (40)$$

Where $\sigma$ is the standard deviation of the measurements, $T_{max}$ and $T_{min}$ are the maximum and the minimum tolerance respectively. For the tilt the tolerance is ± 2 µm; thus, the range of tolerance is 4 µm.

In Fig. 6.7, the repeatability results are displayed. For the same installation case (case a), the standard deviation is 0.01 µm, while mounting the same valve ten times (case b) gives a standard deviation of 0.19 µm; the part standard deviation (case c) is 0.38 µm.

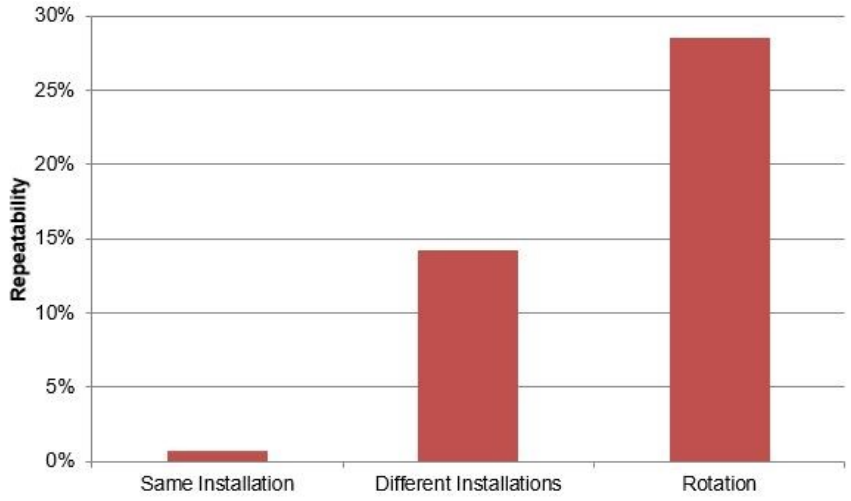


*Figure 6.7 - Repeatability of the measurements for three different test conditions*

All the tests have shown that the standard deviation is within the tolerance thresholds; in particular the deviation introduced by the measurement station is low, half of the part repeatability even considering the worst case scenario, 14.3% compared to 28.5% of repeatability of rotating the pin respect to the valve body.

In conclusion, the measurement station can be considered robust and reliable for the FAG measurement.

## 6.4. Results

In order to evaluate the capability of the proposed assembly process, 10 parts have been tested. The punch that acts on the pin was guided, to avoid any bending moment (Fig. 6.8). The armature was centred by means of a pin, in contact with a linear encoder length gauge, in order to measure the displacement of the valve pin.

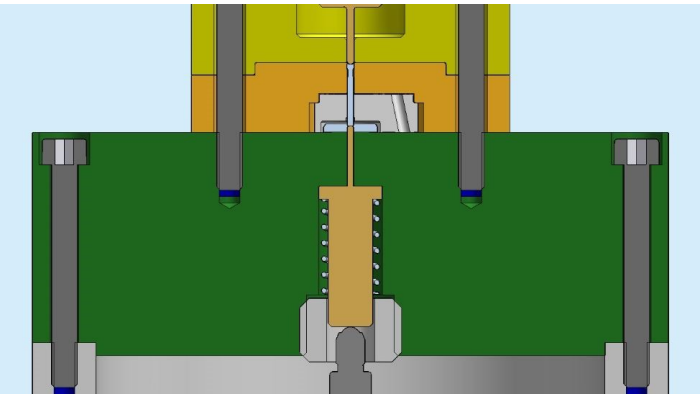

*Figure 6.8 - Valve fixture of the press-fit station*

A further linear encoder length gauge with 0.05 µm of resolution was used as position feedback of the AMSD signal control loop.

For each part, a preassembly was done in order to establish the fastening between pin and armature by interference-fit. After the pre-press phase the current position of the armature was measured and the FAG calculated as the average of 4 positions of the pin, 90 degrees rotate each, in order to set the remaining displacement needed, accomplished with the final press-fit phase. Driving the piezoelectric actuator dynamically, using AMSD control loop and measuring the displacement with the linear encoder length gauge the targeted setpoint is achieved. Fig. 6.9 depicts the force-displacement graph during the press-fit process; after reaching the static friction load, there is an abrupt acceleration of the pin, due to the transition between static and dynamic friction coefficient. After that, a steady dynamic friction coefficient is reached and the displacement steps are more constant and more predictable. The same behaviour was observed and discussed in Section 4.3.2.2, when samples manufactured for the control loop validation of were used.

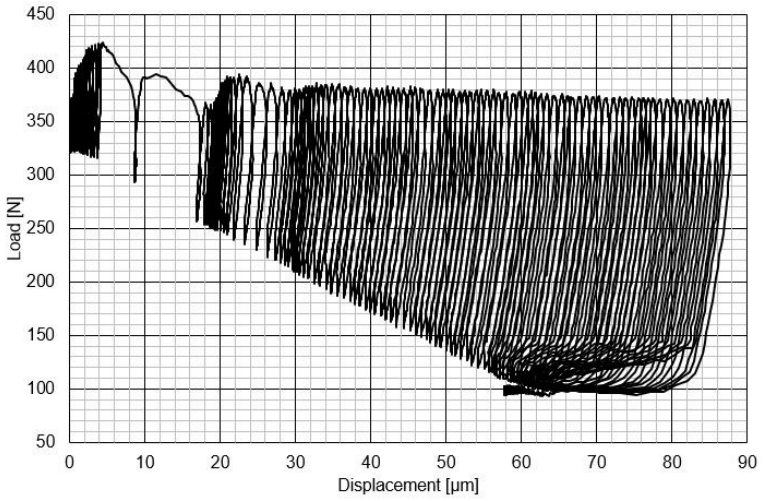


*Figure 6.9 - Force - Displacement curve of a press-fit process of a valve*

After this phase, the valve was mounted on the measurement station for the final check of the FAG. Fig. 6.10 shows the final measurements of the 10 pressed parts with respect to the tolerance.

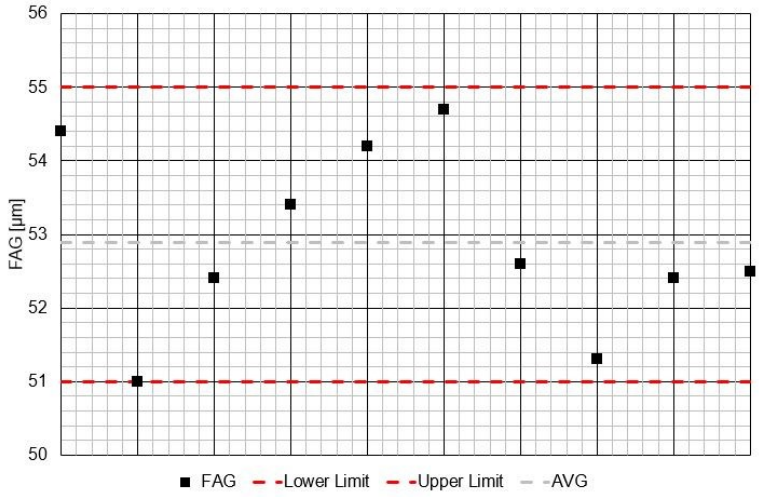


*Figure 6.10 - Results of the assembly of 10 valves*

All the valves have been pressed within the specifications tolerance; furthermore, the average is really close to the nominal value of 53 µm. The results demonstrate the feasibility of the proposed process, regarding the position of pin and armature for a solenoid control valve of CR injector.

# 7. Conclusions

The new tightened emissions regulations are increasing the request for optimal performing engines, able to fulfil the low emission levels demanded in the near future.

Fuel injectors are a core part of the engine and are currently affected by several inaccuracies, that are nowadays corrected by using different learning functions implemented in the ECU. In order to obtain more efficient components, a more accurate production process for the manufacturing of these devices is highly requested and beneficial.

Assembly processes are fundamental in the fabrication of both gasoline and diesel injectors; a high geometric accuracy is essential for optimal and reproducible operations, especially in terms of final relative position of the mating parts.

The thesis presents a piezo actuated press, used to characterize the main phenomena that take place during an interference-fit assembly. The results were used to develop two different control strategies for the full scale prototype press, a hybrid press-fitting station which combines in series a hydraulic cylinder and a piezoelectric actuator. The station features a large operation range and a high micrometric positioning accuracy.

A series of experiments has been carried out, in order to compare the strategies for controlling the press process: a Constant Slope Driving (CSD) and Amplitude Modulated Sinusoidal Driving (AMSD). The tests were conducted on custom-designed plugs and sleeves. Measurements were performed at the same interference pressure.

An analysis of the load and of the relative displacement during the tests allows to have an insight into the friction phenomena occurring during the press-fit. The overall accuracy of the press fit process has been found strictly dependent on the capacity to detect the start of the irreversible relative motion between the mating parts. In particular, the importance of detecting the pre-sliding phenomena that characterizes the static-dynamic friction has been analysed.

The performance of the hybrid press-fit station has been investigated by changing two parameters of the piezo actuator driving voltage, more precisely the slope and the frequency.

The performance indicator is the positioning error which characterizes the difference between the setpoint and the final position of the plug into the sleeve. The comparison of the results shows a smaller positioning error with the AMSD control strategy, compared to the CSD

process, thanks to its ability to detect and compensate the pre-sliding effect. The control loop based on the AMSD reaches a positioning error of ± 2 µm for setpoint values ranging from 3 to 50 µm. This remarkable accuracy offers potentialities for high precision assembly of metal parts of fuel injector.

In order to evaluate the performances of the AMSD control strategy during the press-fit fo industrial parts, two application cases were investigated in detail:

- Dry calibration process for GDI injector
- Assembly of needle control valve of CR diesel injector

In the first application the aim was to calibrate GDI injectors in the ballistic region, characterized by high sensitivity of the injected quantity to the filter position. Furthermore, in order to have a cleaner and less harmful process, a gaseous test fluid was used instead of a liquid one. The target was to achieve a dispersion less than 15%, in operation with liquid, for an injector batch calibrated with this new process, based on a gaseous agent. This result has been achieved, combining the full scale prototype press with the Loccioni AirMexus, with an error of 13% in the calibration point for a batch of 9 GDI injectors.

The second application case was given by the assembly of the armature of a solenoid control valve for a common rail diesel injector; the pin has to be inserted into the armature hole with a final position between the surface of the valve body and the armature of 53 ± 2 µm. A measurement station has been developed and tested. The repeatability and reproducibility of the measurement station was assessed. Then 10 parts were pressed following the proposed new method, utilizing the full scale prototype press. All the parts have been assembled within the given tolerance.

In conclusion, a new prototype press, able to reach a positioning accuracy of ± 2 µm, has been successfully developed and its performances have been shown and verified in real application processes. The resulted prototype is capable to confirm its potentialities with real components, opening at its introduction in real industrial processes requiring high geometric accuracy.

# Appendix

The derivate of the term $\frac{dp}{dT}$ can be expressed as follow:

(41) $$\frac{d}{dt}\left(\frac{p}{T}\right) = \frac{T\frac{dp}{dt} - p\frac{dT}{dt}}{\mathrm{T}^2}$$

In order to express this term as derivative of the pressure the hypothesis of adiabatic condition during an injection event has been adopted; therefore, the following propriety can be used:

(42) $$pT^{\frac{k}{1-k}} = constant$$

where $k$ is the heat capacity ratio.

By differentiating equation (42), the following expression is obtained:

(43) $$T^{\frac{k}{1-k}}\, dp + p\,\frac{k}{1-k}\, T^{\frac{k}{1-k}}\, T^{-1} dT = 0$$

By simplifying and rearranging:

(44) $$\frac{dT}{T} = \frac{k-1}{k}\frac{dp}{p}$$

Then, multiplying equation (44) by $\frac{T}{dt}$:

(45) $$\frac{T}{dt}\frac{dT}{T} = \frac{k-1}{k}\frac{dp}{p}\frac{T}{dt}$$

Therefore:

(46) $$\frac{dT}{dt} = \frac{T}{p}\frac{k-1}{k}\frac{dp}{dt}$$

By replacing (46) in equation (41):

(47) $$\frac{d}{dt}\left(\frac{p}{T}\right) = \frac{T\frac{dp}{dt} - p\frac{Tk-1dp}{p\ k\ dt}}{\mathrm{T}^2} = \frac{1}{T}\left(\frac{dp}{dt} - \frac{k-1}{k}\frac{dp}{dt}\right) = \frac{1}{T}\frac{dp}{dt}\left(1 - \frac{k-1}{k}\right) = \frac{dp}{dt}\frac{1}{kT}$$

# References


1. Impact of selected policy measures on Europe´s air quality. EEA – European Environmental Agency: EEA Report no. 08/2010; Copenhagen, Denmark, 2010
2. European Union emission inventory report 1990 – 2008 under the UNECE convention on Long-Range Transboundary Ait Pollution (LRTAP). EEA – European Environmental Agency; EEA Technical Report no. 07/2010; Copenhagen, Denmark, 2010
3. Commission Regulation (EC) No. 715/2007. Official Journal of European Union L 42, 1 – 15
4. Commission Regulation (EC) No. 692/2008. Official Journal of European Union L 171, 1 – 16
5. Marotta A, Pavlovic J, Ciuffo B, Serra S, Fontaras G (2015) Gaseous Emissions from Light-Duty Vehicles: Moving from NEDC to the New WLTP Test Procedure, Environmental Science & Technology, Volume 49(14), 8315 – 8322
6. Mock P, German J, Bandivadekar A, Riemersma I, Ligterink N, Lambrecht U, (2013) From Laboratory to road. A comparison of official real-world fuel consumption and CO2 Value for Cars in Europe and the United States, International Council on Clean Transportation
7. Pelkmans L, Debal P (2006) Comparison of on-road emissions with emissions measured on chassis dynamometer test cycles, Transportation Research Part D – Transportation and Environment, Volume 11(4), 233-241
8. Andersson J, May J, Favre C, Bosteels D (2014) On-Road and Chassis Dynamometer Evaluations of Emissions from Two Euro 6 Diesel Vehicles, Int. J. Fuels Lubr, 7(3), 919 – 934
9. Andre M. (2004) The ARTEMIS European Driving Cycles for Measuring Car Pollutant Emissions, Science of the Total Environment, Volume 334, 73 – 84
10. Fontaras G, Franco V, Dilara P, Martini G, Manfredi U (2014) Development and review of euro 5 passenger car emission factors based on experimental results over various driving cycles, Science of the Total Environment, Volume 468, 1034 – 1042

11. Weiss M, Bonnel P, Hummel R, Provenza A, Manfredi U (2011) On-road Emissions of Light-Duty Vehicles in Europe, Environ. Sci. Technol, Volume 45(19), 8575 – 8581

12. Weiss M, Bonnel P, Hummel R, Steininger N (2013) A Complementary Emissions Test for Light Duty Vehicles: Assessing the Feasibility of Candidate Procedures, Publications Office of the European Union, JRC75998

13. Commission Regulation (EC) No.427/2016, Official Journal of European Union, L 82, 8 – 20

14. Johnson T (2016) Vehicular Emission in Review, SAE Int. J. Engines 9(2), 1258 – 1275

15. Johnson, T (2015) Review of Vehicular Emissions Trends, SAE Int. J. Engines, Volume 8(3), 1152-1167

16. Gerhardt J (2015) Advanced Clean Diesel with Closed-Loop Controls, Hyundai-Kia International Powertrain Conference

17. Wong W V, Tung C S (2016) Overview of automotive engine friction and reduction trends - Effects of surface, material, and lubricant-additive technologies, Friction, Volume 4 (1): 1 – 28

18. Pischinger S (2011) Verbrennungsmotoren Band 2 (24 ed.). Aachen, Germany: Lehrstuhl Für Verbrennungskraftmachinen, 335

19. Kašpar J, Fornasiero P, Graziani M (1999) Use of CeO2-based oxides in the three-way catalysis. Catalysis Today. 50 (2): 285–298

20. Jong HK (2010) NO2-Assisted Soot Regeneration Behavior in a Diesel Particulate Filter with Heavy-Duty Diesel Exhaust Gases. Numerical Heat Transfer Part A, Vol. 58 (9), pp.725–739

21. Babcock & Wilcox Company (2007) Steam, Its Generation and Use. Babcock & Wilson Company, 1913

22. Praveena V, Martin M L J (2017) A review on various after treatment techniques to reduce NOx emissions in a CI engine, In Journal of the Energy Institute, 1 – 17

23. Takahashi N, Shinjoh H, Iijima T, Suzuki T, Yamazaki K, Yokota K (1996) The new concept 3-way catalyst for automotive lean-burn engine: NOx storage and reduction catalyst, Catal. Today 27 (1-2): 63 – 69.

24. Doornbos G, Adams E, Carlsson P, Dahl D (2015) Comparison of lab versus engine tests in the development of a highly efficient Ammonia Formation Catalyst for a Passive SCR System, SAE Technical Paper 2015-24-2504, 2015, http://dx.doi.org/10.4271/2015-24-2504

25. Mark J, Candace M (1999) Diesel passenger vehicles and environment, Union of Concerned Scientist

26. Wagner U, Eckert P, Spicher U (2008) Possibilities of Simultaneous In-cylinder reduction of soot and NOx emissions for Diesel engines with direct injection, International Journal of Rotating Machinery

27. Velji A, Remmels W, Schmidt R M (1995) Water to reduce NOx-emissions in diesel engines a basic study, Proceedings of the 21th CIMAC Congress on Combustion Engine Technology, Interlaken, Switzerland, paper no. 46

28. Prasad H S, Gonsalvis J, Vijay V S (2015) Effect of Introduction of Water into Combustion Chamber of Diesel Engines – A Review, Energy and Power, Volume 5(1A): 28-33

29. Dennis A, Garner C, Taylor D (1999) The Effect of EGR on Diesel Engine Wear, SAE 1999-01-0839

30. Leach F, Davy M, Weall A, Cooper B, Comparing the Effect of a Swirl Flap and Asymmetric Inlet Valve Opening on a Light Duty Diesel Engine, SAE Technical Paper 2017-01-2429, 2017

31. Mohan B, Yang WM, Chou SK (2013) Fuel injection strategies for performance improvement and emissions reduction in compression ignition engines—A review. Renewable and Sustainable Energy Reviews, Volume 28, pp. 664–676, doi:10.1016/j.rser.2013.08.051.

32. Stumpp G, Ricco M (1996) Common rail – an attractive fuel injection system for passenger car DI diesel engines, SAE Paper No. 960870

33. Giuffrida A, Carlucci P, Ficarella A, (2004) Preliminary Studies on the Effects of Injection Rate Modulation on the Combustion Noise of a Common Rail Diesel Engine, SAE paper 2004-01-1848, 2004

34. Fuyuto T, Taki M, Ueda R, (2014) Noise and Emissions Reduction by Second Injection in Diesel PCCI Combustion with Split Injection, SAE Int J Engines 2014, Volume 7, 1900–1910

35. Han Z, Uludogan A, Hampson G, Reitz R (1996) Mechanism of Soot and NOx Emission Reduction Using Multiple-injection in a Diesel Engine, SAE Technical Paper 960633

36. G. Ferrari (2016) Internal Combustion Engines. Società Editrice Esculapio

37. Yan F, Wang J (2011) Common Rail Injection System Iterative Learning Control Based Parameter Calibration for Accurate Fuel Injection Quantity Control, International Journal of Automotive Technology, Volume 12(2), 149 – 157

38. Huhtala K, Vilenius M (2001) Study of a common rail fuel injection system, SAE Paper No. 2001-01-3184

39. Dimitriou P, Peng Z, Wang W (2015) Effects of Advanced Injection Strategies on the in-cylinder air–fuel Homogeneity of Diesel Engines, Proc IMechE, Part D, J Automobile Engineering; Volume 229, 330–341

40. Herfatmanesh M R, Peng Z, Ihracska A, Lin Y, Lu L, Zhang C (2016) Characteristics of Pressure Wave in Common Rail Fuel Injection System of High-Speed Direct Injection Diesel Engines, Advances in Mechanical Engineering 2016, Volume 8(5), 1 – 8

41. Baumann J, Kiencke U, Schlegl T (2006) Practical Feasibility of Measuring Pressure Waves in Common Rail Injection Systems by Magneto-Elastic Sensors, SAE paper 2006-01-0891

42. Risi AD, Naccarato F, Laforgia D (2005) Experimental analysis of common rail pressure wave effect on engine emissions, SAE paper 2005-01-0373

43. Catania AE, Ferrari A, Spessa E (2009) Numerical-experimental study and solutions to reduce the dwell-time threshold for fusion-free consecutive injections in a multijet solenoid-type CR system. J Eng Gas Turb Power, Volume 131: 022804

44. Beatrice C, Belardini P, Bertoli C (2001) Combustion process management in common rail DI diesel engines by multiple injection. SAE paper 2001-24-0007

45. Baumann J, Göger D, Kiencke U (2005) A magneto-elastic sensor for measuring pressure oscillations in common rail systems, IFAC Proceedings Volumes, Volume 38(1): 67 – 72

46. Cancellieri A, Claude P L, Method of operating a fuel injector of an internal combustion engine, United States Patent Nr. 20170107928

47. Tordin S, Massaro A, Method of controlling a fuel injection, United States Patent Nr. 9644565

48. Pelizzoni I, Cancellieri A, Method for estimating an instantaneous pressure value in a fuel line of a fuel injection system, United States Patent Nr. 9133787

49. Catania AE, Ferrari A, Manno M, Spessa E (2008) Experimental investigation of dynamics effects on multiple-injection common rail system performance, Journal of Engineering for Gas Turbines and Power-Transactions of the ASME, Volume 130(3), 032806

50. de Risi A, Naccarato, F, Laforgia, D, (2005) Experimental Analysis of Common Rail Pressure Wave Effect on Engine Emissions, SAE Technical Paper 2005-01-0373

51. Kamil M, Rahman M M, Bakar A Rosli, (2016) Development of a complete single jet common rail injection system gas dynamic model for hydrogen fuelled engine with port injection feeding system, International Journal of Mechanical, Aerospace, Industrial, Mechatronic and Manufacturing Engineering, Volume 10(6)

52. Niels L. Pedersen (2016) Principles and design of mechanical face seals. Structural and Multidisciplinary Optimization 54: 349-359

53. Heinz P. Bloch (1998) Improving machinery reliability, Volume 1 (3rd ed.), Gulf Professional Publishing

54. C. C. Selvage (1979) Assembly for interference fits by impact and constant force methods, Master Thesis, Massachusetts Institute of Technology

55. Budynas R G, Nisbett J K (2015) Shigley's Mechanical Engineering Design, Mc-Graw Hill Education

56. Conway H D, Farnham K A (1967) Contact stresses between cylindrical shaft and sleeves, International Journal of Engineering Science, Volume 5, 541 – 554

57. Lindeman, Robert A (1974) Finite element computer program for the solution of nonlinear axisymmetric contact problems with interference fits, NWL Technical Report NWL-TR-3148

58. Parsons B, Wilson E A (1970) A method for determining the surface contact stresses resulting from interference fits, Journal of Engineering for Industry, Volume 90, 208 – 218

59. Andersson S, Soderberg A, Bjorklund S (2007) Tribology International, Volume 40, 580 – 587

60. Patro K S, Sinha R (2004) Influence of friction models on response evaluation of buildings with sliding isolation devices, 13th World Conference on Earthquake Engineering, Paper No. 1373

61. Savietto P, Moraes de Souza M, Savoy J (2012) Stick-Slip Analysis on Press-Fit Joints through Finite Element Method and Laboratory Tests, SAE Paper 2012-36-0189

62. di Liberto F, Balzano E, Serpico M, Peruggi F (2007) Dinamica Stick-Slip: Oscillazioni con Attrito, La Fisica nella Scuola, XL, Volume 3

63. Yamagata Y, Higuchi T (1995) A micropositioning device for precision automatic assembly using impact force of piezoelectric elements. Proceedings IEEE Int. Conf. Robotics and Automation, 1: 666–671

64. Liu Y T, Yamagata Y, Higuchi T (2005) Micropositioning device using impact force of piezoelectric flying wires. IEEE/ASME Transactions on Mechatronics 10: 692-696

65. Liu Y T, Higuchi T (2001) Precision Positioning Device Utilizing Impact Force of Combined Piezo-Pneumatic Actuator. IEEE/ASME Transactions on Mechatronics 6: 467-473

66. Urbakh M, Klafter J, Gourdon D, Israelachvili J (2004). The nonlinear nature of friction, Nature, Volume 430: 525-8

67. Gasparetti M, Paone N, Tomasini E P (1996) Laser Doppler techniques for the combined measurement of inlet flow and valve motion in IC engines, Measurement Science and Technology, Volume 7(4), Pages 576 – 591

68. Lenci S (2009) Lezioni di Meccanica Strutturale, Pitagora

69. Liuti A, Rodriguez Verdugo F, Paone N, Ungaro C (2016) Monitoring techniques for high accuracy interference fit assembly processes. AIP Conf. Proc. 1740: 060005

70. B. Bhushan (2010) Springer Handbook of Nano-technology. Springer-Verlag, Berlin, pp. 896-898

71. Liuti A, Rodriguez Vedugo F, Paone N, Ungaro C (2017) High-accuracy interference-fit assembly utilizing a hybrid actuator, The International Journal of Advance Manufacturing Technologies, doi.org/10.1007/s00170-017-1256-3

72. Lindler J E, Anderson E H, Regelbrugge M E (2013) Design and testing of piezoelectric-hydraulic actuators. Proceedings of SPIE - The International Society for Optical Engineering 5054: 96-107

73. Liu Y T, Wang C C (2009) One-DOF Precision Position Control using the Combined Piezo-VCM Actuator. World Academy of Science, Engineering and Technology 56: 570-575

74. Linjama, M, Huova, M, Pietola, M, Juhala, J, Huhtala, K (2015) Hydraulic Hybrid Actuator: Theoretical Aspects and Solution Alternatives. Proceedings of the Fourteenth Scandinavian International Conference on Fluid Power. Tampere University of Technology, Tampere

75. Castellini P, Revel G M, Tomasini E (1998) Laser Doppler Vibrometry: A Review of Advances and Applications, The Shock and Vibration Digest, Volume 30, 443-456

76. Straffellini G (2000) Attrito e usura dei materiali. Materiali e Ingegneria

77. Nogueira I, Dias A M, Gras R, Progri R (2002) An experimental model for mixed friction during running-in, Wear, Volume 253, 541–549

78. Al-Bender F (2010) Fundamentals of Friction Modeling, Proceedings ASPE Spring Topical Meeting on Control of Precision Systems, Volume 48, 117-122

79. Swevers J, Al-Bender F, Ganseman C, Prajogo T (2000) An integrated friction model structure with improved presliding behaviour for accurate friction compensation, IEEE Transactions on Automatic Control, Volume 45, 675-686

80. Lampaert V, Al-Bender F, Swevers J (2004) Experimental characterization of dry friction at low velocities on a developed tribometer setup for macroscopic measurements, Tribology Letters, Volume 16, 95-106

81. Al-Bender F, Symens W, Swevers J, Van Brussel H (2004) Theoretical analysis of the dynamic behavior of hysteresis elements in mechanical systems, International Journal of Non-linear Mechanics, Volume 39, 1721-1735

82. Levée G, Gasoline Direct Injection, SIA/CNAM 2012, Paris

83. Ungaro C, Buono T, Method for measuring the instantaneous flow of an injector for gaseous fuels, Patent US20100126261 A1

84. Francisco Rodriguez Verdugo (2014) AirMexus: a shot-to-shot device for testing CNG injectors, Automotive Testing Technology Forum, Novi, USA